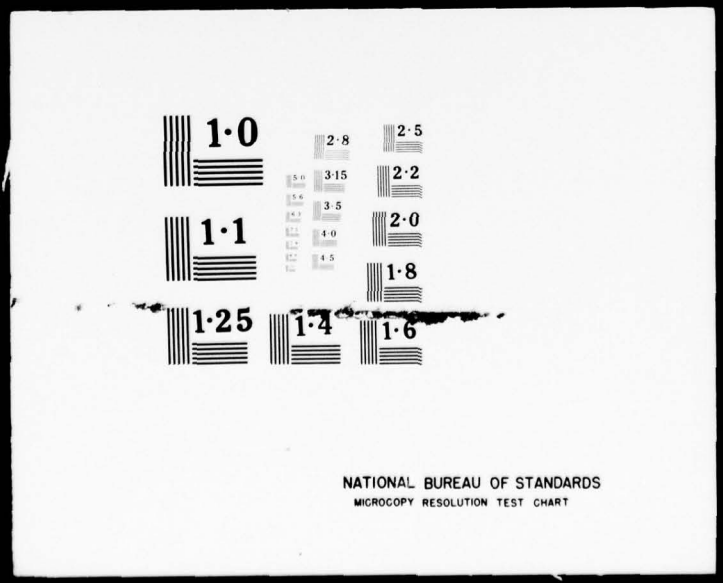
AD-A040 829 ROSENSTIEL SCHOOL OF MARINE AND ATMOSPHERIC SCIENCE --ETC F/G 8/3
WIND-FORCED EQUATORIAL WAVES IN THE ATLANTIC OCEAN.(U)
MAY 77 Z R HALLOCK N00014-75-C-0173
UNCLASSIFIED TR-77-2 NL

1 OF 2
ADA 040829

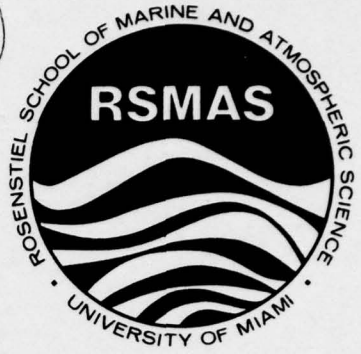


1 OF 3
ADA
040829



ADA040829

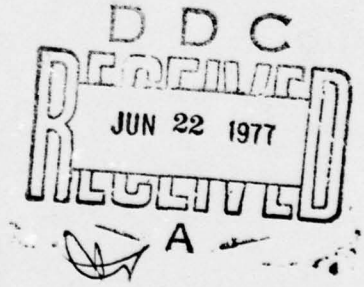




TECHNICAL REPORT

WIND FORCED EQUATORIAL WAVES IN THE ATLANTIC OCEAN

By
Zachariah R. Hallock



DISTRIBUTION STATEMENT A
Approved for public release;
Distribution Unlimited

DDC FILE COPY

TR 77-2

SECURITY CLASSIFICATION OF THIS PAGE (When Data Entered)

REPORT DOCUMENTATION PAGE

READ INSTRUCTIONS BEFORE COMPLETING FORM

1. REPORT NUMBER: No. N00014-75-C-0173	2. GOVT ACCESSION NO.
3. RECIPIENT'S CATALOG NUMBER	
4. TITLE (and Subtitle): WIND-FORCED EQUATORIAL WAVES IN THE ATLANTIC OCEAN	5. TYPE OF REPORT & PERIOD COVERED: Technical Report (Ph.D. Dissertation)
	6. PERFORMING ORG. REPORT NUMBER: TR-77-2
7. AUTHOR(s): Zachariah R. Hallock	8. CONTRACT OR GRANT NUMBER(s): N00014-75-C-0173
9. PERFORMING ORGANIZATION NAME AND ADDRESS: Dr. Zachariah R. Hallock - Dept. of Phys. Oceanography, Rosenstiel School of Marine & Atmospheric Sciences, 4600 Rickenbacker Cswy. Miami, Florida 33149	10. PROGRAM ELEMENT, PROJECT, TASK AREA & WORK UNIT NUMBERS: NA
11. CONTROLLING OFFICE NAME AND ADDRESS: CDR. Robert G. Kirk, Code 410, Department of the Navy, Naval Ocean Research & Development Activity, Bay St. Louis, Miss. 39520	12. REPORT DATE: May, 1977
	13. NUMBER OF PAGES: 152 (164p.)
14. MONITORING AGENCY NAME & ADDRESS (if different from Controlling Office)	15. SECURITY CLASS. (of this report): NA
	15a. DECLASSIFICATION/DOWNGRADING SCHEDULE: NA

16. DISTRIBUTION STATEMENT (of this Report)

Approved for public release; distribution unlimited.

17. DISTRIBUTION STATEMENT (of the abstract entered in Block 20, if different from Report)

18. SUPPLEMENTARY NOTES

A condensed version to be published in a scientific journal.

19. KEY WORDS (Continue on reverse side if necessary and identify by block number)

Equatorial waves, Equatorial Atlantic, GATE Equatorial Oceanographic Experiment, Wind-forced long equatorial waves, Equatorial meanders, South equatorial current, equatorial undercurrent

20. ABSTRACT (Continue on reverse side if necessary and identify by block number)

During the GARP Atlantic Tropical Experiment (GATE), north-south fluctuations in the equatorial current system were observed. Observations of current profiles during Phase II suggest that the fluctuations had a period of about 16 days and were propagating westward with a phase speed of 130 to 190 cm/sec. Evidence of fluctuations in the tradewinds at similar frequencies was also found.

Analysis of profiling current meter (PCM) data reveals that latitudinal

DD FORM 1 JAN 73 1473 EDITION OF 1 NOV 65 IS OBSOLETE
S/N 0102-014-6601

SECURITY CLASSIFICATION OF THIS PAGE (When Data Entered)

405 515

BLOCK 20 CONTINUED: shear in the zonal equatorial currents is important, and that meridional and vertical motions are highly time-dependent and have small means.

Theoretical analysis of a linear, two-layer system shows that the characteristics of the observed fluctuations are consistent with the theory of linear, equatorially trapped waves, particularly the Yanai wave.

Numerical integration of equations of this system shows that oscillations such as those observed may be a resonant response to an impulsive, cross-equatorial forcing in the upper layer. The presence of a mean zonal flow with shear modifies but does not drastically alter, the results.

UNIVERSITY OF MIAMI
ROSENSTIEL SCHOOL OF MARINE AND ATMOSPHERIC SCIENCE

TECHNICAL REPORT

May, 1977

WIND-FORCED EQUATORIAL WAVES IN THE ATLANTIC OCEAN

by

Zachariah R. Hallock

D D C
RECEIVED
JUN 22 1977
DISSEMINATED

Submitted to

The Office of Naval Research
Contract No. N00014-75-C-0173

Approved for public release; distribution unlimited

4600 Rickenbacker Causeway
Miami, Florida 33149

William W. Hay
Dean

HALLOCK, ZACHARIAH R. (Ph.D., Physical Oceanography)

WIND-FORCED EQUATORIAL WAVES IN THE ATLANTIC OCEAN

(May, 1977)

Abstract of a doctoral dissertation at the University of Miami.

Dissertation supervised by Professor Walter O. Düing.

During the GARP Atlantic Tropical Experiment (GATE), north-south fluctuations in the equatorial current system were observed. Observations of current profiles during Phase II suggest that the fluctuations had a period of about 16 days and were propagating westward with a phase speed of 130 to 190 cm/sec. Evidence of fluctuations in the tradewinds at similar frequencies was also found.

Analysis of profiling current meter (PCM) data reveals that latitudinal shear in the zonal equatorial currents is important, and that meridional and vertical motions are highly time-dependent and have small means.

Theoretical analysis of a linear, two-layer system shows that the characteristics of the observed fluctuations are consistent with the theory of linear, equatorially trapped waves, particularly the Yanai wave.

Numerical integration of equations of this system shows that oscillations such as those observed may be a resonant response to an impulsive, cross-equatorial forcing in the upper layer. The presence of a mean zonal flow with shear modifies, but does not drastically alter, the results.

PRECEDING PAGE BLANK-NOT FILMED

ACKNOWLEDGEMENTS

I thank the members of my committee for their time and assistance. In particular, I am indebted to Dr. Dennis Moore for his much-needed help in theoretical matters and Dr. Walter Düing for his continuous support over the years.

I am grateful to Drs. Otis Brown and Robert Evans for programming suggestions and for doing the lion's share of the data reduction.

Mr. Kevin Kohler did an excellent job of digitizing my hand analyses, which were then conscientiously key punched by Mrs. Paula Diaz. I thank Ms. Rita Levitt for her superb work in typing the final draft.

I am indebted to all those GATE participants whose observations contributed to this work.

Finally, I thank my wife, Judi, for her patience and support during my years as a student.

This research was supported by the Office of Naval Research under contract NONR 00014-75-C-0173.

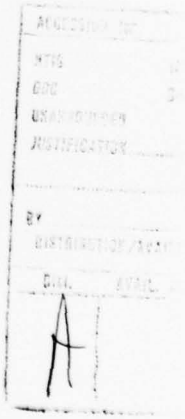


TABLE OF CONTENTS

Chapter			Page
1.	INTRODUCTION		1
2.	ANALYSIS OF THE GATE EQUATORIAL PROFILING EXPERIMENT (GEPE)		10
	2.1	Overview	10
	2.2	PCM Data Analysis	11
		.1 Data Acquisition and Analysis	11
		.2 Description of Analyzed Data	13
	2.3	Dynamics and Kinematics	17
		.1 Accelerations and Momentum Balances	17
		.2 Vertical Motions and Meridional Circulation	21
	2.4	Wind Observations	23
	2.5	Supplementary Observations	25
	2.6	Summary and Interpretation	27
3.	THEORETICAL CONSIDERATIONS AND NUMERICAL EXPERIMENTS		29
	3.1	Introduction	29
	3.2	Derivation of Model Equations	31
	3.3	Solution of the Linear Problem	41
		.1 *Derivation of the Vertical Normal Modes*	41
		.2 Calculation of Normal Mode Parameters	46
		.3 Projection of the Forcing Function on the Vertical Modes	49
		.4 Solution to the Horizontal Equations	51
		.5 The Forced Problem	53
		.6 Solution to the Steady Problem	53
	3.4	Numerical Experiments	54
		.1 Numerical Method	54
		.2 Cases Studied	59
		.3 Derived Quantities	60
		.4 Presentation of Results	61
4.	DISCUSSION OF RESULTS		63
	4.1	Comparison of Model Results with Linear Theory	63
	4.2	Effects of Mean Current	69
	4.3	Comparison of Observations with Theoretical and Numerical Results	71
	4.4	Future Research Suggested by the Present Investigation	76
5.	CONCLUSIONS		79

LIST OF TABLES

		Page
Table 1:	Wave Parameters Estimated from Observations	16
Table 2:	Rossby No. as a Function of Gravity Wave Speed and Current Velocity	38
Table 3:	Range of Parameters for Error Estimates	48
Table 4:	Range of Normal Mode Parameters	49
Table 5:	Yanai Wave Characteristics for Model Modes	67
Table 6:	Phase Speeds Extracted from Longitude-Time Maps; Pulsed Forcing	69

LIST OF FIGURES

		Page
Fig. 1	Track of R/V ISELIN during GATE, Phase II	85
Fig. 2	R/V ISELIN - Current at 10 Meters	86
Fig. 3	R/V ISELIN - Current at 80 Meters	87
Fig. 4	R/V ISELIN - Surface Wind	88
Fig. 5	R/V ISELIN - Depth of 21^{o} Isotherm	89
Figs. 6 to 10	Vertical Sections of Zonal Current and Meridional Circulation	90
Fig. 11	R/V HUMBOLDT - Current at 10 Meters	96
Fig. 12	R/V HUMBOLDT - Current at 50 Meters	97
Fig. 13	R/V ISELIN - Current in Upper Layer	98
Fig. 14	R/V ISELIN - Current in Lower Layer	99
Fig. 15	R/V HUMBOLDT - Current in Upper Layer	100
Fig. 16	R/V HUMBOLDT - Current in Lower Layer	101
Fig. 17	R/V ISELIN - Vertical Sections of Average Velocity	102
Fig. 18	Percent of Local Zonal Acceleration Accounted for by Coriolis Acceleration and Meridional Advection of Zonal Momentum	103
Fig. 19	Layer Transports at the Equator - Observed	104
Fig. 20a	Correlation of v-components of Surface Wind and Current. R/V ISELIN, Phase II	105
Fig. 20b	Periodogram of Surface Wind at the Equator and 10^{o}W. R/V PASSAT, Phase II	105
Fig. 21	Current Velocity at Undercurrent Core at 23.5^{o}W, as Observed from R/V KURCHATOV	106
Fig. 22	Diagram of System used to Study Wind-Forced Oscillations	107
Fig. 23	Dispersion Diagrams for Model Baroclinic Modes	108

		Page
Fig. 24	Yanai Wave Dispersion Diagrams a. Period vs. Phase Speed for Westward Yanai Wave b. Period vs. Phase Speed for Eastward Yanai Wave	109
Fig. 25	Temporal Dependence of Forcing Function	110
Fig. 26	Mean Fields	111
Figs. 27 to 67	Model Results	
Fig. 27	Case 3: Forcing = Step 2, No Mean Flow $\eta_1(y,t)$	112
Fig. 28	" $\eta_2(y,t)$	113
Fig. 29	" $u_1(y,t)$	114
Fig. 30	" $u_2(y,t)$	115
Fig. 31	" $v_1(y,t)$	116
Fig. 32	" $v_2(y,t)$	117
Fig. 33	" $v_1(x,t)$ (real)	118
Fig. 34	" $v_2(x,t)$ (real)	119
Fig. 35	Case 4: Forcing = Pulse, No Mean Flow $\eta_1(y,t)$	120
Fig. 36	" $\eta_2(y,t)$	121
Fig. 37	" $u_1(y,t)$	122
Fig. 38	" $u_2(y,t)$	123
Fig. 39	" $v_1(y,t)$	124
Fig. 40	" $v_2(y,t)$	125
Fig. 41	" v-external (y,t)	126
Fig. 42	" v-internal (y,t)	127
Fig. 43	" $v_1(x,t)$ (real)	128
Fig. 44	" $v_2(x,t)$ (real)	129
Fig. 45	Case 5: Forcing = Step 2, Mean Flow Present $\eta_1(y,t)$	130

			Page
Fig. 46	Case 5: Forcing = Step 2, Mean Flow Present	$\eta_2(y,t)$	131
Fig. 47	"	$u_1(y,t)$	132
Fig. 48	"	$u_2(y,t)$	133
Fig. 49	"	$v_1(y,t)$	134
Fig. 50	"	$v_2(y,t)$	135
Fig. 51	"	$u_{1\ \text{total}}(y,t)$	136
Fig. 52	"	$u_{2\ \text{total}}(y,t)$	137
Fig. 53	"	$v_1(x,t)$ (real)	138
Fig. 54	"	$v_2(x,t)$ (real)	139
Fig. 55	Case 6: Forcing = Pulse, Mean Flow Present	$\eta_1(y,t)$	140
Fig. 56	"	$\eta_2(y,t)$	141
Fig. 57	"	$u_1(y,t)$	142
Fig. 58	"	$u_2(y,t)$	143
Fig. 59	"	$v_1(y,t)$	144
Fig. 60	"	$v_2(y,t)$	145
Fig. 61	"	$u_{1\ \text{total}}(y,t)$	146
Fig. 62	"	$u_{2\ \text{total}}(y,t)$	147
Fig. 63	"	$v_1(x,t)$ (real)	148
Fig. 64	"	$v_2(x,t)$ (real)	149
Fig. 65	V-upper (real) Case 4: Pulsed Wind, No Mean Flow (Entire Latitude Domain)		150
Fig. 66a	Layer Transports - Case 4: v-component, Imaginary Part		151

Page

Fig. 66b Layer Transports - Case 6: v-component, Imaginary Part 151

Fig. 67 Percent of Variance Contained in Normal Modes 152

1. INTRODUCTION

The equatorial regions of the oceans and atmosphere have long been a topic of intense interest to the theoretician as well as to the observationalist. Unique aspects of the behavior of the circulation in these regions are primarily the result of the zero-crossing of the vertical component of the Coriolis acceleration.

At latitudes away from the equator, circulation problems can be treated with quasi-geostrophic theory. This theory is a manifestation of the constraints on long-period motions resulting from the earth's rotation. The gross aspects of the circulation can be understood without inclusion of non-linear and complicated, frictional dependence.

Near the equator, this is not the case. It is not immediately apparent which balances are important. Quasi-geostrophic theory takes on a different interpretation since the inertial period is very much dependent on the latitude and becomes infinite at the equator. While the theory can be defined using an equatorial adjustment time scale (Moore and Philander, 1976), there is, nevertheless, a latitude at which the Coriolis acceleration becomes so small as to result in balances which include non-linear and dissipative processes in the steady state.

On the other hand, time-dependent motion could exist in which non-linear and dissipative processes are not significant. This would be true mainly in the absence of currents with intense shear, which is not the case in the real ocean.

The equatorial ocean is characterized by intense zonal currents to a depth of about 400 m. These currents display strong variations

in space and, based on more recent observations, time. Typically, from the surface to a depth of about 50 m, from about 5°N to 5°S in the Atlantic, there is westward flow with speeds up to 120 cm/sec. From about 50 m to 200 m or more, the flow is eastward with a somewhat smaller magnitude. Below this depth, there is sometimes a weaker westward flow. The intense eastward flow is referred to as the Equatorial Undercurrent or Lomonosov Current. In the Pacific, a similar structure exists (Philander, 1973b; Knauss, 1966; Stalcup and Metcalf, 1966; Rinkel, 1964; and Knauss, 1961).

Variations from periods of several months to a year have been noted in earlier studies, although evidence of higher-frequency fluctuations has been presented by Rinkel (1964), Wunsch and Gill (1976), and Groves and Miyata (1967).

During the GARP Atlantic Tropical Experiment (GATE), overwhelming evidence was found for the existence of energetic fluctuations of equatorial fields with periods ranging from tidal to several months (Düing, 1975). The result has been an increased interest in time-dependent, equatorial motion. There was also evidence of energetic fluctuations in the tradewinds at similar periods (Krishnamurti, 1975 a and b). It is not clear from the observations alone whether the current fluctuations constitute a true meander or whether they are part of a wavelike process which exists over a wider latitude range.

According to Moore and Philander (1975) and Gill (1975), theories on equatorial motions can be divided into two somewhat exclusive categories: linear and non-linear, steady-state, wind-driven models (mostly numerical), and linear, inviscid, time-dependent, free and forced models (mostly analytical). Notable exceptions include studies by Cane (1975)

and by O'Brien and Hurlburt (1973), where time dependence, advection, and friction have been included. Even these latter investigations, however, are primarily concerned with the long-term spinup of an entire ocean initially at rest, rather than short-term variability.

Non-linear, steady-state models, which are typified in a paper by McKee (1973), are in essential agreement as to the reasons for the existence of the Equatorial Undercurrent and the general equatorial circulation. They predict correct scales in latitude and zonal velocity and agree on the gross features of the meridional or secondary circulation. They rely, to a large extent, on vertical and/or horizontal eddy viscosity coefficients, however, and thus, finer structure in their results is somewhat arbitrary. The vertically averaged, non-linear terms, in conjunction with the meridional circulation, tend to transport eastward momentum equatorward (Gill, 1975). A common interpretation of all steady-state models is that an easterly wind over an equatorial ocean bounded to the west will, within several weeks after onset, develop an eastward pressure gradient force as a result of set-up against the boundary. The setup is the result of westward transport, which occurs primarily in the surface layer near the equator. An eastward flow results at a depth where this pressure gradient force exceeds the westward drag of the wind. A secondary circulation develops due to the poleward Ekman divergence in the mixed layer, resulting in an equatorward flow in the thermocline. This meridional flow modifies the zonal velocity profile through advective effects.

A difficulty with the homogeneous models is that a vigorous upwelling develops at the equator as part of the meridional circulation. This is not consistent with observations according to Moore and Philander

(1975). In the presence of stratification, however, a depth-dependent zonal flow can approach geostrophy, and thus, the meridional circulation will be less than in the homogeneous case. Stratified, non-linear, steady-state models (Robinson, 1966; Philander, 1973) show the same essential features as the homogeneous models near the surface, except for the reduced upwelling. Due to the additional thermohaline effects, however, the stratified models help to explain the deep westward flow observed by Stalcup and Metcalf (1966).

While the steady-state theories cannot explain the dynamics of the observed fluctuations, they set the stage for possible explanations which are offered in this study. Theory provides a mechanism by which the equatorial current system can come into existence as a nearly geostrophic zonal flow. The meridional flow constitutes a secondary circulation which is a result of the Ekman divergence in the surface layer. In the steady-state, momentum and energy input by the wind is balanced by frictional dissipation through vertical and horizontal shear.

Mikhailova and Shapiro (1972) have treated a problem similar to that of Charney and Spiegel (1971), except that a two-layer density field is included. The model also includes a linear friction law (depending on horizontal velocity) in lieu of horizontal viscosity. They approach the time-dependent aspect by applying a time-varying zonal wind, which results in an increase of the mean transport due to the non-linearities. The v-component of the response is antisymmetric about the equator, however, and the shortest period in the forcing is two months, thus limiting the applicability of the model to fluctuations observed during GATE.

Philander (1976) has found that surface current systems such as the Atlantic South Equatorial Current and the North Equatorial Countercurrent may be unstable to certain waves, and that the Undercurrent may respond passively through vertical coupling. The parameters in the theory include the characteristics of the mean westward flow on a latitude scale of about 10^{o}, which is beyond the range of the PCM GATE data. This type of theory, which is a linearized wave problem (i.e., with the mean flow included as a space-variable coefficient), states that infinitessimal disturbances to a mean state, provided they have the right characteristics, will grow in time, deriving energy from the mean flow through non-linear interaction. Once the perturbation has grown sufficiently, the dynamics must move from a linearized to a truly non-linear regime. On the other hand, with a finite perturbation such as a time-dependent wind forcing with characteristics that do not necessarily satisfy the instability conditions, a response involving non-linear interactions would also result which might be related to the meanders observed.

Cane (1975), in a non-linear, time-dependent, numerical model*, includes a case where a southerly wind-component is added to the forcing after the model is integrated to an equilibrium with an easterly wind.

---

*Cane's model is composed of an active layer of one density overlying another of higher density. The lower layer is quiescent, or motionless. The active layer is divided into a surface frictional layer of fixed thickness and a thicker subsurface layer which contains the Undercurrent. Vertical advection of momentum between the layers is included, as well as vertical and horizontal viscosity.

A result is the upwind shift of the Undercurrent over a period of about two months and the development of a quasi-stationary meander pattern in latitude and longitude, originating at the western boundary and propagating (in the group sense) eastward. During the first month, over the whole domain, especially in the eastern quarter where longitudinal structureis initially negligible, a transient, north-south oscillation of the Undercurrent occurs with a period of about 16 days. It eventually damps out, but this may be due to the dissipation in the model. It appears to be a locally excited transient. A deficiency of this calculation, as far as GATE observations are concerned, is that the surface zonal flow which exists at the onset of the southerly wind is eastward instead of westward over most of the domain along the equator. This is likely related to the peculiar nature of the surface layer in the model. These results, nevertheless, bear the closest resemblance to the observations insofar as the meanders are concerned.

The problem of linear equatorial waves has been dealt with in detail by Matsuno (1966), Moore (1968), Lighthill (1969), and Cane and Sarachik (1976). The most extensive study for free equatorial waves in the ocean is given by Moore (1968).

The scales of motion predicted by these theories are consistent with the features of GATE observations, but the assumption of linearity is not completely justified. Moore (1968) defines an equatorial Rossby number, $R_o \equiv U/\beta L^2$, where U is the velocity scale, L is a length scale, and β is the latitudinal derivative of the Coriolis parameter. It can be said that this is the Rossby number at latitude L for length scale L.

If L is sufficiently large or U sufficiently small, R_o may be neglected, resulting in the linear equations of motion. It turns out a posteriori that L is not arbitrary, but constitutes a trapping scale for equatorial waves. According to Moore (1968),

$$L = \sqrt{\frac{C_g}{\beta}}$$

where C_g is a gravity wave speed associated with the vertical mode under consideration and is about 200 cm/sec for low-order baroclinic modes. L, which is also termed the equatorial radius of deformation, R_d, is about 100 to 300 km in these cases. Consequently, for $U \gtrsim 50$ cm/sec, R_o is no longer negligible. In particular, if a mean zonal flow, such as that observed near the equator, is included, the Rossby number exceeds unity, regardless of the velocity scale of the fluctuations.

Linear wave theory, therefore, would be applicable for small amplitudes if there were no equatorial currents. In the real ocean, however, these currents exist, and some manifestation of their effect must be included in the study of time-dependent motions near the equator.

While the steady-state and large-scale, time-integrated numerical models include features such as the Undercurrent, it is the wave theories which are most directly applicable to motions such as those observed during GATE. The question still remains as to the origin of the disturbances.

The instability mechanism proposed by Philander (1976) offers one explanation. However, Philander (personal communication) has stated that several-week oscillations with wavelengths larger than 1500 km

are not likely to be unstable in the Atlantic, and the observed fluctuations appear to be of the order of 2500 km in length (Düing et al, 1975).

Waves generated in a different location, e.g., near a boundary, which propagate into the area of observation, provide another possibility. Problems of this nature have been treated by Moore (1968) in the absence of a mean zonal current.

A third explanation, which is not entirely exclusive of the second, is wind forcing. This problem has been treated formally by Lighthill (1969) and Cane and Sarachik (1976) for the equatorial ocean. They suggest that many equatorial modes can be excited, depending on the form of the forcing process. These studies are quite general in scope and do not treat the specific cases of interest in any detail. Moreover, they do not include consideration of mean currents.

Observational evidence for wind-forced equatorial waves is offered by Wunsch and Gill (1976) from sea-level fluctuations in the equatorial Pacific. They found that correlation between atmospheric pressure and sea-level indicated the excitation of equatorially trapped inertia-gravity waves in the first baroclinic mode.

The above description of Cane's 1975 model also suggests that several-week oscillations may be transients excited by meridional, time-dependent wind forcing. The advantage of this model is that an undercurrent exists; i.e., non-linear effects have been included.

The purpose of the present study is to try to determine the nature of the current fluctuations observed during GATE on the basis of their kinematic and dynamic properties, and to provide a plausible hypothesis

for their generation. In particular, it is shown that such fluctuations are likely to be a resonant response to a broad-band, impulsive excitation rather than a direct passive response to a continuing forcing component or the result of a dynamic instability process in which wave characteristics depend on details of mean flow profiles. It is further demonstrated that a meridional windstress component, such as that observed during GATE, is adequate to produce such a response.

2. ANALYSIS OF THE GATE EQUATORIAL PROFILING EXPERIMENT (GEPE)

2.1 Overview

During the GARP Atlantic Tropical Experiment (GATE) in 1974, a great number of observations were obtained in the Equatorial Atlantic by many different institutions. It will be some time before all data are properly assimilated and combined to give an overall picture of the processes in the atmosphere and ocean during the period of the experiment. Descriptions of the oceanographic measurements appear in GATE Report #14 (1976).

The present investigation is based on the analysis of GEPE data, surface wind data from ships in the vicinity of GEPE, the results of the reports indicated above, and several publications by GATE investigators.

The GEPE data were acquired by workers from the University of Miami from four ships during Phase II of GATE, from 7 July to 19 August. On R/V COLUMBUS ISELIN, Düing (1975b) acquired 65 profiling current meter (PCM) stations, 44 STD stations, and 166 XBT traces while traversing a trapezoidal track between 1.75°N and 1.25°S, 18°W and 29°W. Brown (1975) acquired 30 PCM's from the GDR vessel ALEXANDER VON HUMBOLDT between 1.5°N and 1.5°S, 23.5°W and 25°W. Hallock (1975) obtained 43 PCM's from the U.S.S.R. vessel AKADEMIK KURCHATOV at 23.5°W. At 10°W, 13 PCM's were obtained by Low (1975) from the French ship CAPRICORNE.

My analysis efforts centered on the PCM data from R/V ISELIN since they are the most comprehensive data from GEPE. Similar, but less extensive, analysis was performed on PCM data from R/V HUMBOLDT. Data from R/V KURCHATOV and R/V CAPRICORNE, being more restrictive in scope, have been used for comparison.

Surface wind observations have been investigated to estimate the spatial and temporal variability of atmospheric forcing on the ocean in the GEPE area.

The analysis was performed in five main steps: 1) PCM data were calibrated, edited and corrected for systematic errors due to observational procedures; 2) interpolation and smoothing in latitude and time were effected through a hand analysis followed manual digitization; 3) diagnostic calculations on the analyzed data were performed to estimate magnitudes of accelerations and momentum balances; 4) correlations between the surface wind and current were computed; and 5) the data were averaged into two active layers consistent with principal vertical distributions.

The objectives of the analysis described in the remainder of this chapter are to describe the major features of the PCM data set, obtain quantitative estimates of the dynamic processes implied, and to state a hypothesis for explaining the observed fluctuations of the equatorial currents.

2.2 PCM Data Analysis

2.2.1 Data Acquisition and Analysis

The PCM data from R/V ISELIN are now examined. Figure 1 is a plot of PCM station positions distributed in latitude and time (y-t plane). This figure represents the sampling pattern for the profiles where profiles from 29^{o}W are lumped together with those from 28^{o}W, assuming that east-west scales are much greater than 1^{o} longitude.

At each position, a PCM and an STD profile were made to a depth of about 600 m. In a similar manner, XBT profiles were obtained over the same sampling domain. Preliminary processing of the PCM data was performed aboard ship on a PDP-8E mini-computer, allowing for early analysis of gross features (Düing et al., 1975). Subsequent processing and analysis was done on a UNIVAC 1106 in Miami. Details of the data reduction can be found in Brown et al.(1977).

Due to irregular spacing and paucity of observations in y and t, I decided to do a hand analysis (not unlike classical meteorology techniques) of the velocity components for each 10-meter level to a depth of 200 m. Below 200 m, currents become weak and variable, and the results of this type of analysis become questionable. A similar analysis was done for the surface wind and thermocline depth, as observed from R/V ISELIN. The resulting contour maps are typified in Figs. 2 to 5. The maps were first sketched with the positions of the contours being estimated by manual linear interpolation between data points in the y-t plane. Details on scales less than the average y-t spacing of the data were smoothed out and derivatives (horizontal) were made reasonably uniform in areas of large magnitudes. The maps were subsequently digitized to a one-day, 15-mile grid for further analysis. A series of meridional (latitude-depth) sections was prepared from the digitized data. These sections (Figs. 6 to 10) are contour plots of zonal velocity and vector plots of meridional and vertical velocity (more will be said later about the calculation of vertical velocity). Figures 17 a and b are y-z sections of time-averaged zonal and meridional velocity components (u, v). These figures show that the structure of the flow field

is quite complex and that it changes significantly with time, but that in the mean, v is quite small. It can also be seen from Fig. 17b that a calculation of mean vertical velocity from v_y would not be significantly different from zero in any part of the domain (y, z) of the observations.

Two properties of the GATE PCM data set indicate the use of caution when interpreting results of time averages. These are the shortness of the record compared to the period of the principal fluctuations and the amplitude of these fluctuations compared to the mean. In addition, there is evidence of significant fluctuations with periods longer than the record length: in our observations, the mean position of the Undercurrent is north of the equator, in contrast to results at 23.5°W (Bubnov, 1975), as well as theoretical predictions which place the Undercurrent upwind of the equator in the mean (e.g., McKee, 1973; Charney and Spiegel, 1971; Philander, 1973). In short, while we can get good estimates of the scales of the time-dependent behavior of the equatorial currents, mean values cannot be expected to be representative of long-term mean conditions.

2.2.2 Description of Analyzed Data.

The most outstanding feature in Fig. 3 is a lateral, latitudinally antisymmetric fluctuation in time of the zonal velocity component at a depth of 80 m. Examination of the meridional component reveals a north-south advection consistent with this fluctuation (this point will be systematically demonstrated in Section 2.2). The westward flow at the surface, while not as well defined, exhibits variability on the

same scales (Fig. 2). The possibility that the observed 2 to 3-week oscillation is an artifact of the sampling scheme has been ruled out since it is present in several independent sets of observations.

The meridional sections (Figs. 6 to 10) exhibit a distinct, bimodal structure: the north-south oscillation of the westward surface flow maximum tends to be about 90^{o} out of phase with that of the core of the Undercurrent. This feature is suggestive of the mixed-mode oscillation of a two-layer system.

The y-t maps of the zonal component at 80 m (Fig. 3) show maxima symmetric in latitude about the position of the core of the Undercurrent. These may be associated with symmetric wave modes or may be the eastward acceleration which would result from a poleward advection of the equatorial water.

Figures 11 and 12 present the corresponding y-t maps at 10 m and at 50 m for the zonal and meridional components of velocity, as observed from R/V HUMBOLDT at 23.5^{o}W. By comparing meridional(v) components at 10 m from 23.5^{o}W and 28^{o}W, we can infer a westward phase propagation of about 150 cm/sec, assuming that the phases in the two plots are one and the same. The calculation is done by dividing the difference in longitude by the temporal offset, which is about 4.5 days. The resulting speed is in approximate agreement with a similar calculation by Düing et al. (1975), who compared y-t maps of maximum zonal (u) components from the two ships. They obtained a time difference of three days, giving a phase speed of 190 cm/sec. The u-component at the surface is not well enough defined to identify phases with any certainty, and the v-components at the core depth are difficult to compare due to a non-zero mean (which may be in error - see Fig. 21) at the HUMBOLDT

longitude. Düing et al. (1975) also estimated a period of 16 days by identifying quasi-sinusoidal appearance of the map of u-max with one cycle of a fluctuation or "meander."

Clearly, it is difficult to define a period or a phase speed with great certainty. We should, therefore, infer a range of such parameters from the data. According to Düing (1975), the best estimate of the time lag between phases at 28°W and 23.5°W, based on salinity observations from R/V HUMBOLDT, R/V ISELIN, and R/V TRIDENT, as well as PCM data, is about three days. The estimates made with the v-components at the surface, as described above, yield a value of 4.5 days. The east-west distance between ISELIN and HUMBOLDT is 500 km. We thus obtain a phase speed ranging from 130 to 180 cm/sec. In all cases where a quasi-periodic structure in y-t can be defined, the estimate of the period varies between 15 and 17 days. We can now derive a range of values for an east-west wavelength.

$$C \approx (130 \text{ to } 190) \text{ cm/sec}$$

$$T \approx (15 \text{ to } 17) \text{ days}$$

$$\lambda \approx (2070 \text{ to } 2790) \text{ km}$$

It must be emphasized that the independent observed parameters are C and T, whereas λ is derived from them, assuming a dependence of the form

$$e^{i(\sigma t + kx)} \quad \text{where } k = 2\pi/\lambda$$

Alternative interpretations are possible but less likely. Following Düing et al.(1975), we construct a table (c.f. Table 1) of C, λ, vs. n

for eastward and westward-propagating waves. The number of complete cycles of the waves that exist between the two longitudes is represented by n. Previous calculations have been for the n = 0 case.

Table 1. Wave Parameters Estimated from Observations

n	Cn (cm/sec)	n (km)	
1	41 - 55	607 - 714	for eastward waves
2	19 - 23	274 - 294	
0	130 - 190	2070 - 2790	for westward waves
1	27 - 32	397 - 415	
2	15 - 17.5	222 - 227	

This table summarizes the possible wave parameter ranges which can be derived by visual inspection from the y-t maps. These ranges will be used in Chapter 4, where comparison with theoretical dispersion curves is made.

In addition to the y-t maps of current velocity components, a similar map of the depth of the 21^{o}C isotherm (thermocline) is presented in Fig. 5. A quasi-periodic structure appears in this quantity as well. The variations toward the end of the record, if interpreted as vertical motion, imply oscillatory vertical velocities of theorder of 10^{-2}cm/sec. This value is in agreement with estimates of vertical velocity computed from the divergence of horizontal velocity. Figure 5 shows the most pronounced change in height, from 55 m to 95 m, between 10 August and

14 August, indicative of an 8-day period if interpreted as a half-cycle. This result is in agreement with those derived from temperature observations by Miller (1977) and Bubnov et al. (1975).

While there exist many interesting features in the observations as presented, e.g., small-scale vertical structure fluctuations which might be indicative of the presence of internal waves, the focus of this investigation is on the north-south oscillations of the eastward Undercurrent and the westward surface flow. For purposes of simplification, the digitized y-t map data were averaged into two layers between 0 and 200 m. The boundary between the layers was chosen as the depth of zero zonal velocity component. One reason for this choice is that it is reasonable to expect the dynamics of a westward flow to be significantly different from that of an eastward flow at the equator. Another reason is that the layered configuration chosen allows a more direct comparison of the observations with a two-layer dynamical model, such as those previously discussed, and an additional one to be introduced in Chapter 3.

The y-t maps of these layer-averaged data are presented in Figs. 13 to 16. It is seen that the essential features of the lateral oscillations are retained, while minor features are smoothed out and amplitudes are decreased.

2.3 Dynamics and Kinematics

2.3.1 Accelerations and Momentum Balances

The observations discussed in the previous sections depict vigorously time-dependent fluctuations in the equatorial current system. To better understand the dynamical processes involved, estimates of

terms in the equations of motion have been made. In their usual form, these equations are in units of acceleration (cm/sec^2).

Terms which have been examined include:

$$u_t,\ vu_y \quad \beta yv,\ v_t,\ \beta yu,\ \nu_v u_{zz},\ \text{etc.}$$

The accelerations, like the velocities from which they are derived, are quasi-periodic, so that the instantaneous values are considerably greater than mean values.

Typical magnitudes for the local and advective time derivatives of u and v are $10^{-4} cm/sec^2$. These are in agreement with the values found by Knauss (1966) for the advective derivatives. In the region just above the core of the Undercurrent, dissipative terms of the same magnitude are encountered, assuming vertical eddy viscosity of 50 cm/sec^2. The choice of a value of vertical viscosity is difficult: Jones (1973) reports a strong dependence of the viscosity on depth. In the light of our observations, viscosity is likely to be time-dependent as well. Poleward of 0.75^o latitude, the Coriolis acceleration becomes important.

It is not practicable to estimate zonally dependent accelerations such as uu_x with the available data, but they are likely to be important. Katz (1976) reports a mean value of p_x of about 10^{-5} cm/sec^2 in acceleration units. Large variances of p_x indicate that instantaneous values are considerably higher. [Weisberg (personal communication) reports meridional pressure gradients, based on STD data, which vary on similar time scales.]

A windstress of the order of 0.5 dyn/cm^2 would produce the observed value of v_t of 10^{-4} cm/sec^2 (assuming a τ /H stress model). It is

quite probable that the magnitude of the time-dependent windstress exceeded this value at R/V ISELIN during Phase II of GATE (Fig. 4).

Vertical advection terms appear to be important in regions of high vertical shear of horizontal velocity. In particular, at a depth of 50 m, where u_z reaches a maximum, wu_z reaches a magnitude of 10^{-4} cm/sec^2.

Many terms in the momentum equations appear to be of comparable magnitude near the equator, and it is not clear whether there are any principal balances. Consequently, an attempt has been made to systematically test certain balances. Clearly, since we cannot evaluate all terms in the equations, all possible balances cannot be considered. If, however, several terms seem to cancel each other consistently, the importance of the terms in a dynamical process will have been established. As it turns out, one tirm conclusion can be drawn from the calculations to be described.

We test a balance among terms: $A_i(\vec{r}, t)$, $i = 1, N$

where: $\vec{r}$ = position vector

t = time

A_i = term in equation

by computing a coefficient:

$$\rho(\vec{r}) = 1 - \left[\overline{\left(\sum_i A_i\right)^2} \right]^{\frac{1}{2}} \Big/ \sum_i \left(\overline{A_i^2}\right)^{\frac{1}{2}}$$

where

$$\overline{(\ )} \equiv \frac{1}{T} \int_0^T (\ )\, dt$$

and ρ is confined to the interval (0, 1). A value of 1 implies a perfect balance, while a value of 0 results for maximum imbalance.

We are calculating the complement of the normalized root mean square (RMS) residual of a sum of quantities which are expected to cancel to a degree. Balance coefficients were computed for sets of terms such as:

a) $u_t + vu_y - \beta yv$

b) $u_t + vu_y - \beta yv - \nu_v u_{zz}$

c) $v_t + \beta yu$

etc.

Clearly, any calculations involving ν_v must be treated with caution, as its value is questionable.

The primary result shows that, at the depth of the core of the Undercurrent, particularly at latitudes of maximum meridional shear, there is a dominant contribution to the local acceleration by the meridional advection of zonal momentum. This balance coefficient (computed for a), above) is depicted in Fig. 18. Equatorward of 0.75° latitude, the Coriolis term is of secondary importance. It is emphasized that this calculation is more than just an estimate of the magnitude of the nonlinear term, vu_y. It represents the systematic contribution to the local acceleration by that term. Other balances, including those for the meridional equations, indicate likewise that non-linear terms are important in most of the latitude-depth region spanned by the data. Unfortunately, while inclusion of more terms tends to improve these balances, they by and large do not rise above 60%, thus limiting the interpretation of the results.

The conclusion to be drawn from these calculations is that mean flow must be considered when attempting to model the observed processes.

At the very least, meridional advection of zonal momentum and of the associated geostrophic meridional pressure gradient must be included.

2.3 Vertical Motions and Meridional Circulation

An important aspect of equatorial current observations is the meridional circulation, i.e., north-south and vertical flow. Most discussions of these flows, however, are associated with steady-state models (e.g., McKee, 1973). In such models, a secondary circulation is required to balance the Ekman divergence resulting from the zonal wind forcing. The balance is effected through dissipative terms which depend on the shear in the meridional flow. Vertical velocities in McKee's model are of the order of 10^{-2} cm/sec. The model is for a homogeneous ocean, however, and in models which include stratification, the magnitudes of the vertical motions and meridional flow are considerably lower.

Figures 6 to 10 represent instantaneous values of the meridional circulation derived from the digitized y-t maps. The w-component was computed as follows:

$$w(y,z,t) = - \int_o^z \nabla_H \cdot \vec{v}_H \, dz$$

where: $w(z = 0) = 0$

$$\nabla_H \equiv \vec{i} \frac{\partial}{\partial x} + \vec{j} \frac{\partial}{\partial y}$$

$$\vec{v}_H \equiv \vec{i}u + \vec{j}v$$

For ∇_H two cases have been considered. First, assuming $u_x \ll v_y$,

$$\nabla_H \cdot \vec{v}_H \approx v_y$$

If u_x is considered important, however, we must make some assumption about the longitudinal structure based on the observations. Our best guess is for a westward-propagating disturbance with a phase speed of 160 cm/sec.

If we let

$$u = u[\,k(x + ct)\,] = u(\,\xi\,),$$

then

$$u_t = kcu'$$

$$u_x = ku'$$

$$u' \equiv u_\xi$$

$$u_x = \frac{1}{c}\,u_t$$

Inclusion of the x-structure results in values of w which are smaller by about 50% than those computed from v_y alone. However, the overall y-z structure remains qualitatively the same. Typical magnitudes of w were found to be 10^{-2} cm/sec and greater. Errors are such that w can only be estimated to within a factor of about two. The main purpose of these calculations is to show the y-z structure, or the meridional flow, and to illustrate the intense time dependence.

There is a systematic structure to the derived meridional circulation in the y-z plane, and it is quasi-periodic in time. Due to large time-dependent amplitudes and a short record length, the time-averaged value of this circulation is not significantly different from zero. Thus, comparisons with meridional circulations implied in steady-state models are not meaningful. On the other hand, the oscillatory nature of w and v (and well as u) are consistent with a wavelike phenomenon. The meridional circulation is essentially consistent with the variation in the position and with the shape of the zonal current field. The

results imply that the time-varying meridional circulation is part of the same wavelike phenomenon that is manifest in the lateral oscillation of the Undercurrent. Based on observational results alone, it is not clear whether the oscillations are solely meanders in the Undercurrent or are manifestations of some wave phenomenon which extends beyond the north-south limits of the Undercurrent

Figure 19 is a plot of time series of meridional transports in the two previously defined layers, and their sum:

$$M_1 = H_1 v_1$$
$$M_2 = H_2 v_2$$
$$M_T = M_1 + M_2$$

The total (M_T) shows the 16-day periodicity even more clearly than in the Undercurrent or surface flow. M_T corresponds roughly to the external mode of a linear, two-layer system.

2.4 Wind Observations

In Figs. 2 to 4, similarities in scales of variability can be seen between wind and current. Correlation coefficients for the v-components, calculated for several time lags, are presented in Fig. 20a. A lag of one day yields a high degree of correlation between about 1^{o}S and 0.75^{o}N latitude. Correlations between the zonal components are much lower, except near 1^{o}N, for a time lag of 5 to 6 days. Although these results cannot be considered to be statistically significant, they suggest that a high correlation between meridional components of wind and current is plausible.

Time series of wind observations from two Soviet ships at the equator have been examined. The ships were R/V AK. KURCHATOV and R/V PASSAT. Observations were obtained at 23.5°W and 10°W, respectively. Figure 20 b is a typical periodogram computed from the PASSAT data. A significant amount of energy exists in the v-component at periods ranging from 5 days to several weeks. Gaps in the records between phases necessitated separate analysis of each phase, thus reducing the quality of the results.

Krishnamurti (1975b) inferred the wind field at 850 mb from satellite photographs of clouds during the entire GATE period. Subsequent analysis of the winds revealed simultaneous surges in the Tradewinds, with a dominant period of 14 to 15 days and longitudinal wavelength of the order of 2500 km. At the equator, these surges were primarily from the southeast, with a maximum near 25°W. Amplitudes of the surges were about 3 m/sec, with maximum intensities up to 8 m/sec. These values are in agreement with those observed from R/V ISELIN (recall Fig. 4). Krishnamurti (1975a) cites other authors reporting 2 to 3-week oscillations in tropical wind systems (Wallace and Chang, 1969; Yanai and Murkami, 1970; Kousky and Wallace, 1971; Krishnamurti et al, 1972; Gruber, 1974).

In summary, wind observations during GATE imply the existence of time variability of the meridional wind component at periods of 2 to 3 weeks, with longitudinal scales corresponding to wavelengths of 2000 to 3000 km. A very simple argument will now be presented to show that a modest windstress applied on this time scale can produce an acceleration resulting in a velocity amplitude comparable to that observed during the PCM experiment.

Assume: τ = 0.25 dyn/cm. Let the windstress act as a body force over a layer of depth, H = 40 m. A period of 16 days has a quarter-cycle of 4 days (the time during which the response should reach maximum amplitude). Thus,

$$v = \int_{t=0}^{4 \text{ days}} \frac{\tau^{(y)}}{\rho H} \, dt = 22 \text{ cm/sec.} \qquad (\rho \approx 1)$$

This value is indeed of the same order as the observed amplitude. The stress model described is the one used in Chapter 3 in the dynamical model to be considered.

2.5 Supplementary Observations

At 23.5°W and 10°W, north-south arrays of Soviet BPV-2 (or Alekseev) moorings were deployed by R/V KURCHATOV, R/V PASSAT, R/V VIZE, and R/V ZUBOV. These moorings were maintained during all three phases of GATE. Each mooring carried about 10 BPV-2 current meters at depths ranging from 15 to 700 meters. They sampled current speed and direction every half-hour. In a preliminary GATE report and in TROPEKS '74, Bubnov (1975 a & b) analyzed the observations from 23.5°W. The resulting latitude-time maps of velocity components show the same oscillatory behavior in the equatorial current system as observed from R/V ISELIN and R/V A. V. HUMBOLDT (Fig. 21). In a later study, Bubnov (1976) presents the results of a spectral analysis done on selected time series from both 23.5°W and 10°W. The principal result was the existence of a pronounced energy peak for a period of 16 to 18 days at and near the equator at depths up to 100 m. There was also evidence of higher frequencies, including semi-diurnal tides. Off the equator, at 10°N and

23.5°W, a dominant peak was found at the local inertial period of 68 hours. Bubnov concludes that the several-week period corresponds to an equatorial inertial oscillation. It is noted that the inertial period at one baroclinic radius of deformation (100 to 300 km) from the equator is of the order of 2 to 3 weeks.

Meincke (1975) obtained results from three current meter moorings at 29°W at latitudes of 0°1'S, 0°49.5'S, and 0°25'N. The mooring at 0°25'N yielded one record at a depth of 18 m. At 0°1'S, records at six levels were obtained: 18, 75, 96, 127, 308, and 499 meters. At 0°49.5'S, records at five levels were obtained: 75, 96, 127, 308, and 499 meters. The instruments operated throughout Phase II. Spectral analysis yielded dominant energy peaks at semi-diurnal periods. Less pronounced peaks at 24.8 hours were also present. Records were not of sufficient duration to yield spectral estimates for periods longer than about 8 days, but examination of plots of the v-component reveals a pronounced, quasi-periodic, 16-day signal with an amplitude of about 40 cm/sec to a depth in excess of 100 m. Tidal signal amplitudes were typically 10 to 15 cm/sec.

Krishnamurti (1976) reported on the objective analysis of sea surface temperatures (SST's) based on satellite data and ship observations. Spectral estimates based on the data from the entire GATE period show fluctuations with periods of 3, 7, 16, 20, and 38 days, as well as higher frequencies, including tidal. East-west scales of several thousand kilometers are evident in the analyzed maps of SST.

Brown (1977) reports similar spatial scales in satellite-derived SST data from the equatorial area during GATE.

Current profiles taken by Hallock (1975) aboard R/V KURCHATOV at the equator and at 23.5°W show evidence of tidal frequencies (the sampling interval was 6 hours) and several-week lateral and vertical fluctuations in the position of the Undercurrent. The duration of this series of profiles was about two weeks.

All these observations imply that the 16-day oscillation is a real and prominent feature of the equatorial current system, and, while signals of higher frequency are present, the PCM data do not seem to be severely alaised by these signals.

2.6 Summary and Interpretation

The GATE PCM observations offer strong evidence of north-south oscillatory motions with a 2 to 3-week period in the equatorial Atlantic. Associated with these fluctuations are vertical motions, as inferred from calculations of vertical velocity which are also periodic in time. The meridional circulation is consistent with changes in the latitude-depth structure of the zonal current. The existence of a 16-day oscillation is corroborated by independent measurements at longitudes ranging from 10°W to 29°W during all three phases of GATE. The principal features of these fluctuations are retained when the data are averaged into two layers, the interface between the layers corresponding to the isotach of zero zonal velocity.

Dynamical calculations revealed that advective and frictional terms in the equations of motion are probably important near the equator, and, in particular, meridional advection of zonal momentum is pronounced in the level of the Undercurrent.

The role of frictional processes is found to be important, particularly in regions of large vertical shear of horizontal flow. It is difficult, however, to quantitatively determine its effect in the present case due to the uncertainty of a value for vertical eddy viscosity.

It is shown that the assumption of a reasonable windstress acting over the upper of the two defined layers is capable of producing the observed northward speeds. Furthermore, both the frequency content of the wind field and its correlation with the surface flow suggest wind forcing on the scales of the observed 16-day fluctuation.

Excitation by a time-varying wind, with possible strong interactions with mean zonal currents, constitutes a plausible mechanism for generation of the several-week oscillation. This conclusion provides the motivation for the theoretical discussions and numerical experiments to follow.

3. Theoretical Considerations and Numerical Experiments

3.1 Introduction

As discussed in Chapter 2, several investigations of the response of the equatorial ocean to winds have been carried out using a two-layer approximation for the vertical structure. The primary reason for choosing such a system is that it is the simplest one which can accomodate the gross features of the structure of the equatorial currents. A single layer would necessitate extending the Undercurrent to the surface everywhere and would not allow for the simulation of some of the features in the observations. For example, the southward shift of the core of the Undercurrent four days after the onset of the northward flow at the surface would not be possible in a single layer system. The two-layer system also allows several options for setting the density structure and for the application of forcing. As will be shown later, the layered system in many ways resembles a continuously stratified system, such as the one treated by Moore (1968).

The system to be considered may be referred to a "$2\frac{1}{2}$" layer model. It consists of two active layers of finite mean thickness overlying an infinitely deep or quiescent layer (Fig. 22). Each layer is treated as a shallow fluid of constant density. Densities increase with mean layer depth. A property of the bottom layer thus defined is that horizontal pressure gradients and horizontal motions are everywhere vanishingly small. The elevation of the lower interface, η_3, is, therefore, completely determined by the elevations of the other two. The horizontal extent of the system is from 15^{o}N to 15^{o}S. For the class of motions considered, and due to the fact that the $2\frac{1}{2}$-layer configuration has no

barotropic mode, boundaries at these latitudes have virtually no effect on the short-term response near the equator. The east-west structure is approximated by simple harmonic dependence.

A mean, geostrophically balanced zonal current is included in the model. It consists of a westward flow in the surface layer and an eastward flow in the Undercurrent layer. Meridional dependence of the currents is Gaussian (i.e., e^{-y^2}) with an e-folding distance of 300 km in the surface layer and 100 km below. The current fields thus defined are fixed in time and independent of longitude. They enter the equations as latitude-variable coefficients simulating some of the non-linear terms. Due to these properties it is possible to Fourier transform the equations in longitude and consider the problem for a single longitudinal wave number at a time.

Forcing is applied by assuming an acceleration in the form of a body force, τ/H, where τ is the windstress and H is the layer over which it acts. The windstress in this study is a simple function of time and is independent of latitude, except near the boundaries. Longitudinal dependence is implicit in the wave number of the harmonic component considered. Attention has been restricted to a meridionally forced problem since it is the simplest form of forcing that will produce a latitudinally symmetric v-component, such as that observed, in the response. To obtain such a response with only a zonal forcing component would require a nonzero windstress curl. Clearly, the observed wind field is much more complex than the assumed forcing function, but the aim here is to seek a possible mechanism for wave generation, not to explore all possible cases.

In the following sections, the equations for this system are

presented and put into a form to be integrated numerically. Also, the linear case has been examined analytically for comparison with the observations and to check numerical results. Finally, the numerical simulation itself is discussed and cases with mean flow are compared with other results.

3.2 Derivation of Model Equations

I begin with the linearized, inviscid, shallow-fluid equations on an equatorial beta-plane (i.e., the Coriolis parameter is directly proportional to the latitude) for a two-layer, divergence-coupled system overlying a third, infinitely deep, motionless layer. This system is essentially the same as that used by Philander (1976). Included is a fixed, geostrophically balanced mean zonal current in each of the active layers. I have assumed *that the non-linear terms are small, except* where interaction with the idealized, longitudinally independent zonal currents are concerned. Thus, for the fluctuations (dependent variables), the Rossby number is small. A Rossby number is defined, however, which relates to the magnitude of the mean flow. Wind forcing is introduced as a body force which acts uniformly over the upper layer.

For convenience, the following constants are defined:

$$\rho' \equiv \rho_2 - \rho_1 \ , \quad \rho'' \equiv \rho_3 - \rho_2 \ , \quad \alpha \equiv \frac{\rho' + \rho''}{\rho''}$$

On the equatorial beta-plane, the Coriolis parameter takes the form:

$$f = 2\Omega \sin \Phi \approx 2\Omega \Phi = \frac{2\Omega y}{R} \equiv \beta y$$

where Ω = rotation rate of earth

Φ = latitude (angle)

R = radius of earth

y = latitude (distance)

also: x = longitude (distance)

(u_i, v_i) = horizontal velocity in layer i

g = acceleration of gravity

(F, G) = upper layer forcing function

Following Fig. 22 for other variable definitions, the equations of motion for this system are:

$$u_{1_t} + \bar{u}_1 u_{1_x} + v_1 \bar{u}_{1_y} - \beta y v_1 = -g\eta_{1_x} + F$$

$$v_{1_t} + \bar{u}_1 v_{1_x} + \beta y u_1 = -g\eta_{1_y} + G$$

$$\beta y \bar{u}_1 = -g\bar{\eta}_{1_y}$$

$$\eta_{1_t} - \eta_{2_t} + \bar{u}_1(\eta_{1_x} - \eta_{2_x}) + v_1(\bar{\eta}_{1_y} - \bar{\eta}_{2_y}) + (H_1 + \bar{\eta}_1 - \bar{\eta}_2)(u_{1_x} + v_{1_y}) = 0$$

$$u_{2_t} + \bar{u}_2 u_{2_x} + v_2 \bar{u}_{2_y} - \beta y v_2 = \frac{-g}{\rho_2}(\rho_1 \eta_{1_x} + \rho' \eta_{2_x}) \qquad \text{Eqs. (1)}$$

$$v_{2_t} + \bar{u}_2 v_{2_x} + \beta y u_2 = \frac{-g}{\rho_2}(\rho_1 \eta_{1_y} + \rho' \eta_{2_y})$$

$$\beta y \bar{u}_2 = \frac{-g}{\rho_2}(\rho_1 \bar{\eta}_{1_y} + \rho' \bar{\eta}_{2_y})$$

$$\frac{\rho'}{\rho''}\,\eta_{1_t} + \alpha\eta_{2_t} + \bar{u}_2\,\left(\frac{\rho'}{\rho''}\,\eta_{1_x} + \alpha\eta_{2_x}\right) + v_2\,\left(\frac{\rho'}{\rho''}\,\bar{\eta}_{1_y} + \alpha\bar{\eta}_{2_y}\right) +$$

$$\left(H_2 + \frac{\rho'}{\rho''}\,\bar{\eta}_1 + \alpha\bar{\eta}_2\right)\left(u_{2_x} + v_{2_y}\right) = 0$$

The boundary conditions are that the meridional component of velocity vanish at the zonal boundaries at 15^o latitude, and all variables are taken to be periodic in the selected east-west wave number. The system is initially at rest (except for the mean flows) and is integrated in time with an applied forcing function. The boundary conditions are expressed as follows:

At $y = \pm 15^o$ latitude

$$u_{1_t} = -g\,\eta_{1_x}$$

$$\beta y u_1 = -g\eta_{1_y}$$

$$v_1 = 0$$

$$u_{2_t} = -g\,\left(\frac{\rho_1}{\rho_2}\,\eta_{1_x} + \frac{\rho'}{\rho_2}\,\eta_{1_y}\right)$$

$$\beta y u_2 = -g\,\left(\frac{\rho_1}{\rho_2}\,\eta_{1_y} + \frac{\rho'}{\rho_2}\,\eta_{2_y}\right)$$

$$v_2 = 0$$

$$u_1\,(x + \lambda) = u_1\,(x), \text{ etc.}$$

For $u_1 \propto e^{ikx}$; $k = \frac{2\pi}{\lambda}$

(The mean flow is prescribed in such a way as to be virtually zero at and near the zonal boundaries. Hence, they need not be included here.)

Non-dimensional variables and associated scale constants are defined as follows:

$$(u_1,\ u_2,\ v_1,\ v_2) \equiv U\ (u_1',\ u_2',\ v_1',\ v_2')$$

$$(x,\ y,\ \lambda) \equiv L\ (x',\ y',\ \lambda'),\ H_1/H_2 \equiv H$$

$$t \equiv Tt',\ \eta_1 \equiv A_1\eta_1',\ \eta_2 \equiv A_2\ \eta_2'$$

$$(\bar{u}_1,\ \bar{u}_2) \equiv \bar{U}\ (\bar{u}_1',\ \bar{u}_2'),\ \bar{\eta}_1 \equiv \bar{A}_1\ \eta_1'\ ,\ \bar{\eta}_2 \equiv \bar{A}_2\ \bar{\eta}_2'$$

Scale factors are chosen which are appropriate for the class of motions being investigated. This choice is largely a matter of convenience since no terms will be neglected as a result.

Anticipating accelerations of similar magnitude, but not necessarily of the same phase in the two layers, pressure gradients in the two layers are assumed to be of comparable magnitude as well. Hence, the same scale factor is chosen, appropriately weighted for the density differences, for the two interfaces, η_1 and η_2.

$$(A_2,\ \bar{A}_2) \equiv (A,\ \bar{A}) \equiv \frac{\rho_2(A_1,\ \bar{A}_1)}{\rho'} \qquad \text{or}$$

$$(A_1,\ \bar{A}_1) = \frac{\rho'}{\rho_2}\ (A,\ \bar{A})$$

An equatorial Rossby number is defined which is associated with the magnitude of the mean current:

$$R_o \equiv \bar{U}/\beta L^2$$

In the momentum equations, relations among U, A, and L are chosen to be consistent with quasi-geostrophic scaling:

$$(U, \bar{U}) = \frac{g\rho'}{\rho_2} \quad \frac{(A, \bar{A})}{\beta L^2}$$

A baroclinic, equatorial radius of deformation is defined:

$$R_d \equiv \sqrt{\frac{Cg}{\beta}} \qquad Cg \equiv \sqrt{g\rho' H_1/\rho_2}$$

Thus, $$(A, \bar{A}) = (U, \bar{U})\ H_1/\beta R_d^2$$

Finally, defining:

$$\gamma \equiv \rho'/\rho_2 \quad , \quad \delta \equiv \rho_1\rho'/\rho_2\rho''$$

and assuming

$$\rho_1/\rho_2 \approx 1,$$

and choosing an "inertial" time scale:

$$T = 1/\beta L$$

the scaled momentum equations are divided by βL $(U, \bar{U})$ and the continuity equations by A/T, which yields:

$$u_{1_t} + R_o (\bar{u}_1 u_{1_x} + v_1 \bar{u}_{1_y}) - yv_1 = -\eta_{1_x} + \frac{F}{U\beta L}$$

$$v_{1_t} + R_o \bar{u}_1 v_{1_x} + yu_1 = -\eta_{1_y} + \frac{G}{U\beta L}$$

$$y\bar{u}_1 = -\eta_{1_y}$$

$$\gamma\eta_{1_t} - \eta_{2_t} + R_o \left[\bar{u}_1 (\gamma\eta_{1_x} - \eta_{2_x}) + v_1 (\gamma\bar{\eta}_{1_y} - \bar{\eta}_{2_y})\right] + \qquad \text{Eqs. (2)}$$

$$\left[\frac{Rd^2}{L^2} + R_o (\gamma\bar{\eta}_1 - \bar{\eta}_2)\right] (u_{1_x} + v_{1_y}) = 0$$

$$u_{2_t} + R_o (\bar{u}_2 u_{2_x} + v_2 \bar{u}_{2_y}) - yv_2 = -\eta_{1_x} - \eta_{2_x}$$

$$v_{2_t} + R_o \bar{u}_2 v_{2_x} + yu_2 = -\eta_{1_y} - \eta_{2_y}$$

$$y\bar{u}_2 = -\bar{\eta}_{1_y} - \bar{\eta}_{2_y}$$

$$\left[\delta\eta_{1_t} + \alpha\eta_{2_t} + R_o\left[\bar{u}_2\left(\delta\eta_{1_x} + \alpha\eta_{2_x}\right) + v_2\left(\delta\bar{\eta}_{1_y} + \alpha\bar{\eta}_{2_y}\right)\right]\right] +$$

$$\left[H\frac{Rd^2}{L^2} + R_o\left(\delta\bar{\eta}_1 + \alpha\bar{\eta}_2\right)\right]\left(u_{2_x} + v_{2_y}\right) = 0$$

It will be shown later that taking $L = R_d$ is a convenient choice since R_d turns out to be the equatorial trapping scale for the motions involved. L has been left in Equations (2) to illustrate how the divergence of horizontal velocity enters the dynamics. For example, for $L^2 >> R_d^2$, the motion is essentially non-divergent. The remaining free parameters, U, $\bar{U}$ correspond to typical amplitudes of the fluctuation velocity field and the mean flow, respectively. U is set equal to C_g for convenience since it appears only in the forcing terms.

$$R_o = \frac{\bar{U}}{C_g} = \frac{\bar{U}}{\beta R_d^2} \; ; \; \frac{F, G}{U\beta L} = \frac{F, G}{(\beta C_g^3)^{\frac{1}{2}}} = \frac{F, G}{\beta^2 R_d^3}$$

All other constants are determined by the static structure of the system (i.e., the density field) and the rotation rate of the earth.

From the GATE data as well as previous observations (Stalcup and Metcalf, 1966; and Rinkel, 1965), layers can be defined such that the following parameters can be evaluated.

$$H_1 = 40m, \quad H_2 = 80m, \quad \rightarrow \quad H = 2$$

$$\rho' = \rho'' = 0.002 \rightarrow \alpha = 2, \quad \delta = 1$$

$$\rho_1 \approx \rho_2 \approx \rho_3 \approx 1 \qquad \text{(aside from differences)}$$

This yields:

$$Cg = 88.5 \text{ cm/sec} = U$$

$$L = R_d = 197 \text{ km}$$

$$T = 2.57 \text{ days}$$

The time scale can be defined as the period divided by 2π. Thus,

$$Per = 2\pi T \approx 16 \text{ days}$$

The baroclinic adjustment time scale, T, is compatible with the dominant time scale present in the observations. If the system were treated as one active layer 120 m thick with an overall density difference of 0.004, one finds:

$C_g = 217$ cm/sec, $L = R_d = 308$ km, $T = 1.64$ days, $Per = 10.3$ days

Thus, a rather large change in problem parameters results in a relatively small change in the time scale. Since the choice of H_1 and hence, C_g, is somewhat arbitrary, these results may seem fortuitous. It is shown in Section 3.3; however, this is not the case.

R_o is quite dependent on problem parameters for $\bar{U}$ in the range of observed values. Table 2 illustrates this point.

Table 2: Rossby No. as Function of Gravity Wave Speed and Current Velocity

$\bar{U}$ (cm/sec)	C_g (cm/sec)	R_o
10	88.5	0.113
10	217.0	0.046
25	88.5	0.281
25	217.0	0.115

Harmonic dependence in longitude (x) is now introduced.

$$u_1(x, y, t) \equiv \mathrm{Re}\left\{\tilde{u}_1 (y, t)\, e^{ikx}\right\} = \tilde{u}_{1_r} \cos kx - \tilde{u}_{1_i} \sin kx$$

where

$$k = 2\pi/\lambda, \quad \lambda = \text{east-west wavelength}$$

Applying scaling:

$$\lambda = L\lambda', \quad k = k'/L$$

Since the equations are mathematically linear, even when mean flow is included, once the harmonic dependence in x has been introduced, they can be Fourier transformed in that coordinate so that only one wave number component need be considered at once; i.e.:

$$u_t + \bar{u}u_x = F \qquad u = \sum_{j=1}^{\infty} \tilde{u} e^{ik_j x}$$

$$\sum_{j=1}^{\infty} \tilde{u}_t e^{ik_j x} + ik_1 \bar{u}\tilde{u} e^{ik_j x} = \sum_{j=1}^{\infty} \tilde{F} e^{ik_j x}$$

where k_j are such as to make the set $e^{ik_j x}$, $j = 1, \infty$ orthogonal over λ_1, where $k_m = mk_1$. Multiply by $e^{ik_m x}$, integrate over λ_1, and divide by $e^{ik_m x}$:

$$\rightarrow \quad \tilde{u}_t + ik_m \bar{u}\tilde{u} = \tilde{F}$$

The resulting transformed equations are (omitting primes and ~):

$$u_{1_t} + R_o(ik\bar{u}_1 u_1 + v_1 \bar{u}_{1_y}) - yv_1 = -ik\eta_1 + F/\beta^2 R_d^3$$

$$v_{1_t} + R_o ik\bar{u}_1 v_1 + yu_1 = -\eta_{1_y} + G/\beta^2 R_d^3$$

$$\gamma\eta_{1_t} - \eta_{2_t} + R_o\left[ik\bar{u}_1(\gamma\eta_1 - \eta_2) + v_1(\gamma\bar{\eta}_{1_y} - \bar{\eta}_{2_y})\right] +$$

$$\left[1 + R_o(\gamma\bar{\eta}_1 - \bar{\eta}_2)\right](iku_1 + v_{1_y}) = 0$$

Eqs. (3)

$$u_{2_t} + R_o(ik\bar{u}_2 u_2 + v_2 \bar{u}_{2_y}) - yv_2 = -ik(\eta_1 + \eta_2)$$

$$v_{2_t} + R_o\, ik\bar{u}_2 v_2 + yu_2 = -\eta_{1_y} - \eta_{2_y}$$

$$\delta\eta_{1_t} + \alpha\eta_{2_t} + R_o\left[ik\bar{u}_1(\delta\eta_1 + \alpha\eta_2) + v_2(\delta\bar{\eta}_{1_y} + \alpha\bar{\eta}_{2_y})\right] +$$

$$\left[H + R_o(\delta\bar{\eta}_1 + \alpha\bar{\eta}_2)\right](iku_2 + v_{2_y}) = 0$$

(The mean flow equations are unchanged. In fact, they simply represent the relationships of $\bar{U}$ to $\bar{\eta}$ and do not enter explicitly into the solution of the problem; i.e., the mean flow is prescribed.)

These six equations, with the previously stated boundary conditions, constitute the system to be integrated numerically in time. Prior to this, the integration, an analysis of the linear equations for free waves (i.e., for R_o=0 and no forcing) will be carried out to ellucidate numerical results.

3.3 Solution of the Linear Problem

The problem of linear, equatorial waves has been dealt with at length by Lighthill (1969), Matsuno (1966), Moore (1968), and others. The purpose of Section C is to put the previously derived system of equations into a form which is compatible with existing theory for the case where $R_o \ll 1$. The results of the linear analysis are compared with the observations and also with the numerical results for a zero mean flow as a check on the validity of the model.

3.3.1 Derivation of the vertical normal modes

The objective of the following procedure is to take the six coupled Equations (2), with $R_o=0$ for the two-layer system, and define two sets of normal (uncoupled) equations which can be solved separately.* Each of these sets is equivalent in form to the other and to the equations of a barotropic (one-layer) system. The subsequent analysis is identical to that used by Matsuno (1966) yielding a dispersion relation for each mode.

I begin with the redimensionalized equations where the mean flow terms have been omitted:

$$u_{1_t} - \beta y v_1 = -g\eta_{1_x} + F$$

$$v_{1_t} + \beta y u_1 = -g\eta_{1_y} + G$$

$$\eta_{1_t} - \eta_{2_t} + H_1 (u_{1_x} + v_{1_y}) = 0$$

$$u_{2_t} - \beta y v_2 = -g\left(\frac{\rho_1}{\rho_2} \eta_{1_x} + \frac{\rho'}{\rho_2} \eta_{2_x}\right)$$

* The procedure used is that outlined by Lighthill (1969)

$$v_{2_t} + \beta y u_2 = -g \left(\frac{\rho_1}{\rho_2} \eta_{1_y} + \frac{\rho'}{\rho_2} \eta_{2_y}\right)$$

$$\frac{\rho_1}{\rho''} \eta_{1_t} + \alpha \eta_{2_t} + H_2 \left(u_{2_x} + v_{2_y}\right) = 0$$

Boundary conditions are taken at $y = \pm \infty$ and require all fields to vanish. Following Lighthill (1969), thickness variables are defined:

$$h_1 = \eta_1 - \eta_2, \quad h_2 = \eta_2 - \eta_3, \quad h_3 = \eta_3$$

(Constants such as H have been omitted from h since the thicknesses enter only as derivatives.)

As previously:

$$h_3 = \frac{-\rho_1 h_1 - \rho_2 h_2}{\rho_3}$$

resulting with:

$$u_{1_{tt}} - \beta y v_{1_t} = \frac{-g}{\rho_1} \left[\rho_1 \left(1 - \frac{\rho_1}{\rho_3}\right) h_{1_{xt}} + \rho_1 \left(1 - \frac{\rho_2}{\rho_3}\right) h_{2_{xt}}\right] + F_t$$

$$u_{2_{tt}} - \beta y v_{2_t} = \frac{-g}{\rho_2} \left[\rho_1 \left(1 - \frac{\rho_2}{\rho_3}\right) h_{1_{xt}} + \rho_2 \left(1 - \frac{\rho_2}{\rho_3}\right) h_{2_{xt}} + G_t\right.$$

$$h_{1_{xt}} = -H_1 \left(u_{1_{xx}} + v_{1_{xy}}\right)$$

$$h_{2_{xt}} = -H_2 \left(u_{2_{xx}} + v_{2_{yx}}\right)$$

where the momentum equations have been differentiated with respect to time and the continuity equations with respect to x (the procedure for the v-momentum equations is completely analogous).

Defining a matrix:

$$A = a_{ji} = \frac{1}{\rho_3} \begin{bmatrix} \rho_3 - \rho_1 & \rho_3 - \rho_2 \\ (\rho_3 - \rho_2)\ \frac{\rho_1}{\rho_2} & \rho_3 - \rho_2 \end{bmatrix}$$

the above equations are rewritten

$$u_{j_{tt}} - \beta y v_{jt} = -g \sum_{i=1}^{2} a_{ji}\, h_{i_{xt}} + F_{jt} = g \sum_{i=1}^{2} a_{ji} H_i \left(u_{i_{xx}} + v_{i_{xy}}\right) + F_{jt}$$

for each layer, j.

Normal mode variables, $\bar{u}^k$, $\bar{v}^k$, as well as an "effective" or "equivalent" depth, $\bar{H}^k$, are defined such that the following is true:

$$\bar{u}^k_{tt} - \beta y \bar{v}^k = -g\bar{H}^k(\bar{u}^k_{xx} + \bar{v}^k_{xy}) + \bar{F}^k_t \qquad \text{Eq. (4)}$$

The layer variables are defined in terms of the normal mode variables by:

$$(u_j, v_j) = \sum_{k=1}^{2} C^k_j (\bar{u}^k, \bar{v}^k) , \qquad (F, G) = \sum_{k=1}^{2} C^k_1 (\bar{F}^k, \bar{G}^k)$$

Since the normal modes are defined to be independent, the layer equations can be written separately for each mode; i.e., in Eq. (4), substituting for u_j, for mode k:

$$(u^k_j, v^k_j) = C^k_j (\bar{u}^k, \bar{v}^k) ; \quad (F^k, G^k) = C^k_j (\bar{F}^k, \bar{G}^k)$$

This results with:

$$C^k_j(\bar{u}^k_{tt} - \beta y \bar{v}^k_t) = -g \sum_{i=1}^{2} a_{ji} H_i C^k_i (\bar{u}^k_{xx} + \bar{v}^k_{xy}) + \bar{F}^k_t C^k_j =$$

$$-g\bar{H}^k(\bar{u}^k_{xx} + \bar{v}^k_{xy}) C^k_j + \bar{F}^k_t C^k_j$$

A new matrix, B, is defined:

$$B = b_{ji} \equiv a_{ji} H_i \quad .$$

To satisfy the above equation, the following is required:

$$\sum_{i=1}^{2} b_{ji} C_i^k = \bar{H}^k C_j^k$$

This is an eigenvalue problem where the equivalent depths, $\bar{H}^k$, are the eigenvalues and the proportionality constants, C_j^k, form the eigenvectors of the matrix, B. Consequently, for each vertical mode, k, we have $\bar{H}$, C_j, j = 1, 2 and a set of equations:

$$\bar{u}_{tt} - \beta y \bar{v}_t = -g\bar{H} (\bar{u}_{xx} + \bar{v}_{xy}) + \bar{F}_t$$

$$\bar{v}_{tt} + \beta y \bar{u}_t = -g\bar{H} (\bar{u}_{xy} + \bar{v}_{yy}) + \bar{G}_t$$

These are the equations of a single-layer or barotropic, shallow fluid, such as that treated by Matsuno (1966), whose solution is outlined later in this section. The above procedure is applicable to a system with any number of layers, as described by Lighthill (1969). The case of continuous stratification, treated by Lighthill (1969) and Moore (1968), has the same end result, namely, the above-normal mode equations and an equivalent depth which is proportional to the Brunt-Vaisala frequency. The matrix problem is replaced by a Sturm-Liouville problem involving the solution of the separated, vertical structure equation for the system.

3.3.2 Calculation of normal mode parameters

In the previous subsection we derived the equation:

$$\vec{BC} = \bar{H}\vec{C}$$

where C is the vector, C_j, j = 1,2 for each normal mode, k, where the superscript has been omitted. The eigenvalues are found by solving the following equation:

$$\text{Det } [B - \bar{H}I] = 0$$

where I is the identity matrix. This expression results in the secular equation:

$$\bar{H}^2 - p\bar{H} + q = 0$$

where

$$p = b_{22} + b_{11}$$

$$q = b_{11}b_{22} = b_{21}b_{12}$$

We then get:

$$\bar{H} = (p \pm \sqrt{p^2 - 4q}\ ) / 2$$

Choosing the following system parameters:

$$\rho_3 - \rho_2 = \rho_2 - \rho_1 = 0.002$$

$$H_1 = 40 \text{ m}, \quad H_2 = 80 \text{ m}$$

and assume: $\rho_1 \approx \rho_2 \approx \rho_3 \approx 1$ (aside from differences)

$$B = \begin{bmatrix} 16 & 16 \\ 8 & 16 \end{bmatrix}$$

$\bar{H}$ = (27.3, 4.69) cm; (mode 1, mode 2)

$$\vec{C} = \left\{ \begin{bmatrix} 1 \\ .707 \end{bmatrix}, \begin{bmatrix} 1 \\ -.707 \end{bmatrix} \right\}$$

Hereafter, the mode corresponding to $\bar{H}$ = 27.3 cm is referred to as the external mode and the other as the internal mode. The external mode consists of a weighted sum and the internal mode to a weighted difference of the layer velocity components in the light of the corresponding eigenvectors, C. Both modes are baroclinic in nature due to the underlying motionless layer.

$$\bar{u}^1 = (u_1 + \sqrt{2}\, u_2)/\, 2 \qquad \text{external mode}$$

$$\bar{u}^2 = (u_1 - \sqrt{2}\, u_2)/\, 2 \qquad \text{internal mode}$$

The external mode is nearly equivalent to the single mode of a

system consisting of one active layer overlying an infinitely deep, motionless layer. The equivalent depth in this case would be given approximately by (Lighthill, 1969):

$$\bar{H} \simeq \frac{\rho'}{\rho_o} H \quad ,$$

where H is the active layer depth, ρ' is the density difference, and ρ_o is the average density of the system.

Associated with each equivalent depth is a gravity wave speed, $C_g = \sqrt{g\bar{H}}$. This is not to be confused with the phase speed of waves in the solution ($C_g = \sigma/k$), but is related to this and other quantities, as will be shown.

In a later subsection, the solution to the horizontal, normal mode equations is discussed. Periods and phase speeds are proportional to $1/\sqrt{C_g}$, C_g, respectively. It is useful, therefore, to examine the sensitivity of C_g to small changes in problem parameters. This has been done for each of the two modes. Values of all pertinent quantities were computed for a wide range of layer depths and density differences.

From these calculations, a subset was selected (see Table 3 below) as being representative of a reasonable range of values.

Table 3: Range of Parameters for Error Estimates

$H_1 = (20,40,60)$ m

$H_2 = (40,80,120)$m

$\frac{\rho'}{\rho_o} = (2,3,4) \quad X10^{-3}$

$\frac{\rho''}{\rho_o} = (1,2,3) \quad X10^{-3}$

From these, a range of values for $\bar{H}$, Cg, and $2\pi/\sqrt{\beta Cg}$ was derived for each mode. The results are summarized in Table 4 below.

Table 4: Range of Normal Mode Parameters

	External	Internal
H	= 14.3 - 43.1	3.18 - 9.53 cm
C_g	= 119 - 205	56 - 97 cm/sec
$T_o = \frac{2\pi}{\sqrt{\beta C_g}}$	= 13.4 - 10.6	20.3 - 15.5 days

It turns out that $T_o = 2\pi/\sqrt{\beta Cg}$ is the period of the gravest horizontal mode (excluding the Kelvin wave) for east-west wave number, k = 0. This calculation shows that Cg and, to a greater extent, T_o are relatively insensitive to realistic variations in system parameters. To be more concise, T varies as $H^{-\frac{1}{4}}$, where H depends directly on layer depths and density differences.

According to Moore and Philander (1975), the equivalent depths derived from typical density profiles in the tropical Atlantic are 60, 20, 8, 4, 2 cm, respectively, for the first five baroclinic modes. This places the two-layer system being considered about midway among these.

3.3.3 Projection of the forcing function on the vertical modes

In the previous subsection, the normal mode equations, including normal mode representations of the forcing terms, were derived. The normal mode forcing terms are now written in terms of the layer forcing terms. Following Lighthill (1969):

$$(\bar{F}^k, \bar{G}^k) = \frac{\sum_{j=1}^{2} \rho_j H_j C_j^k (F_j, G_j)}{\sum_{j=1}^{2} \rho_j H_\rho (C_j^k)^2}$$

In particular, with $F_2 = G_2 = F_1 = 0$, and $G_1 = G_1(t)$, a latitudinally uniform, time-dependent, cross-equatorial windstress of the form:

$$G_1 = \frac{\tau^{(y)}}{\rho_1 H_1} \rightarrow \bar{G}^k = \frac{C_1^k \tau^{(y)}}{\rho_1 H_1 (C_1^k)^2 + \rho_2 H_2 (C_2^k)^2}, \quad \bar{F}^k = 0$$

For the previously selected parameter values, we obtain:

$$\bar{G}^1 = \frac{\tau^{(y)}}{80m} \qquad \bar{G}^2 = \frac{\tau^{(y)}}{80m}$$

Thus, the forcing is the same on each of the two modes and has a magnitude which is equivalent to that when forcing a single-layer system 80 meters thick. For illustration, another case is considered. A windstress applied uniformly over both layers, with the same densities and thicknesses as previously:

$$G_1 = G_2 = \frac{\tau^{(y)}}{H_1 + H_2}$$

results with:

$$\bar{G}^1 = \frac{\tau^{(y)}}{99.4m}, \qquad \bar{G}^2 = \frac{-\tau^{(y)}}{580\ m}$$

In this case, most of the forcing goes into the external mode, as is intuitively apparent.

3.3.4 Solution to the horizontal equations

Once the vertical dependence has been separated and harmonic dependence in longitude and time has been introduced, the problem is reduced to that of solving an ordinary differential equation in latitude. The resulting equation for v (u and η have been eliminated) in the homogenous (unforced) case is (after Matsuno, 1966):

$$C_g^2 v_{yy} + (\sigma^2 - k^2 C_g^2 + \beta C_g^2 \frac{k}{\sigma} - \beta^2 y^2) v = 0$$

where dependence of the form $e^{i(\sigma t+kx)}$ has been assumed and $C_g = \sqrt{g\bar{H}}$ for the mode under consideration.

Applying the boundary condition for $y = \pm \infty$ where $v \to 0$, the equation admits to solutions of the form:

$$v(y) = C_n e^{-\frac{\beta}{2C_g} y^2} H_n \left(\sqrt{\frac{\beta}{C_g}} y \right)$$

where H_n is the nth Hermite polynomial. This solution requires that:

$$\sigma^2 + k^2 C_g^2 + \beta C_g^2 \frac{k}{\sigma} = \beta C_g (2m + 1)$$

For $k = 0$, $n = 0$,

$$\sigma_0 = \sqrt{\beta C_g} \quad \text{or} \quad T_0 = 2\pi / \sqrt{\beta C_g}$$

corresponding to the time scale previously discussed. Dispersion diagrams for various horizontal modes, n, are presented in Fig. 23. The axes are labelled in dimensional units for each of the vertical modes in the chosen example. While this may be more cumbersome than using a non-dimensional dispersion diagram, it is more readily referenced with real quantities.

The line labelled $n = -1$ on the diagram represents the equatorial Kelvin wave. This is an additional solution to the normal mode equations for the case where $v = 0$ everywhere. Consequently, the above equation for v alone cannot provide this result. The Kelvin wave was introduced by Moore (1968).

It can be seen in Fig. 23 that Rossby wave modes have periods in excess of 40 days and, therefore, are not likely candidates for explaining observations in the period range from two to three weeks. Since it will later become apparent that the Yanai ($n = 0$) mode is of greatest interest, more detailed dispersion curves for these waves are plotted in Fig. 24.

The Yanai wave is sometimes termed the mixed Rossby-gravity wave because, for large values of k, the westward propagating branch resembles a Rossby wave, whereas the eastward branch resembles a gravity wave. For $k = 0$, it lies in between. It is possible that the Yanai wave is in some way related to inertial oscillations since its period for $k = 0$ is the inertial period at $y = \pm R_d$.

3.3.5 The Forced Problem

The solution to the general, linear, initial-value problem will not be presented here. It is a very complex and interesting problem in its own right and has been treated at length by Cane and Sarachick (1976) and Lighthill (1969). It is sufficient to say - and this point is demonstrated in the numerical experiment section - that most of the energy of the response can be accounted for by the first several free, horizontal modes of the system, plus a steady-state component, when present. The free modes have been discussed. The steady solution is quite simple to analyze since it is the Sverdrup transport resulting from the east-west structure of the meridional forcing.

3.3.6 Solution to the Steady Problem

Moore (personal communication) outlined the following analysis. Setting time derivatives to zero in the linear equations:

$$-\beta y v_1 = -g\eta_{1_x} \qquad -\beta y v_2 = -p_{2_x}$$

$$-\beta y u_1 = -g\eta_{1_y} + F \qquad \beta y u_2 = -p_{2_y}$$

$$u_{1_x} + v_{1_y} = 0 \qquad u_{2_x} + v_{2_y} = 0$$

leading to $\beta v_1 = F_x$ (vorticity eq.) and $\beta v_2 = 0 = v_2$

$$\text{if } F = \mathrm{Re}\left\{\frac{\tau}{\rho H_1} e^{ikx}\right\} \qquad \text{then} \qquad v_1 = \mathrm{Re}\left\{\frac{ik\tau e^{ikx}}{\rho H_1 \beta}\right\}$$

If $k \neq 0$, then $u_2 = u_1 = v_2 = 0$.

If $k = 0$, then $v_1 = v_2 = 0$; $|u_1| \geq 0$; $|u_2| \geq 0$.

For $\lambda = 2400$ km

$\tau = 1$ dyn/cm^2

$H_1 = 40$ m

$|v_1| = 2.86$ cm/sec.

3.4 Numerical Experiments

3.4.1 Numerical Method

Taking $R_o = 1$ in Eqs.(3), Section 3.2 (which is equivalent to setting the mean flow scale, $\bar{U}$, to C_g), the following equations result:

$$u_{1_t} = -ik\bar{u}_1 u_1 - v_1 \bar{u}_{1_y} + yv_1 - ik\eta + F/\beta^2 R_d^3$$

$$v_{1_t} = -ik\bar{u}_1 v_1 - yu_1 - \eta_{1_y} + G/\beta^2 R_d^3$$

$$\gamma\eta_{1_t} - \eta_{2_t} = -ik\bar{u}_1 (\gamma\eta_1 - \eta_2) - v_1(\gamma\bar{\eta}_{1_y} - \bar{\eta}_{2_y}) - (1 + \gamma\bar{\eta}_1 - \bar{\eta}_2)(iku_1 + v_{1_y})$$

$$u_{2_t} = -ik\bar{u}_2 u_2 - v_2 \bar{u}_{2_y} + yv_2 - ik(\eta_1 + \eta_2)$$

$$v_{2_t} = -ik\bar{u}v_2 - yu_2 - \eta_{1_y} - \eta_{2_y}$$

$$\delta\eta_{1_t} + \alpha\eta_{2_t} = ik\bar{u}_2 (\delta\eta_1 + \alpha\eta_2) - v_2 (\delta\bar{\eta}_{1_y} + \alpha\bar{\eta}_{2_y}) -$$

$$(H + \delta\bar{\eta}_1 + \alpha\bar{\eta}_2) (iku_2 + v_{2_y})$$

Notice that the third and sixth equations are:

$$\gamma\eta_{1_t} - \eta_{2_t} \equiv A$$

$$\delta\eta_{1_t} + \alpha\eta_{2_t} \equiv B$$

which results in:

$$\eta_{1_t} = (B + \alpha A) / (\delta + \alpha\gamma)$$

$$\eta_{2_t} = (\gamma B - \delta A) / (\delta + \alpha\gamma)$$

Conditions at zonal boundaries were treated as follows:

$$u_{1_t} = -ik\eta_1 \qquad u_{2_t} = -ik(\eta_1 + \eta_2$$

$$\pm y_B u_1 = -\eta_{1_y} \qquad \pm y_B u_2 = -\eta_{1_y} - \eta_{2_y}$$

$$v_1 = v_2 = 0 \qquad \text{at} \qquad y = \pm y_B$$

This results in a system of six equations of the form:

$$\Phi_t^{\ell} = \Gamma^{\ell} \ (\Phi^m) \ , \quad \ell = 1, 6$$

where Γ involves Φ and its derivatives in y.

It was found that a fourth-order differencing scheme for derivatives in y was both efficient and accurate (Cane 1975). Time integration was done by the "leapfrog-trapezoidal" method (Haltiner,1971). These techniques are now described.

Space differencing:

$$\frac{\partial \Phi}{\partial y} \approx [8(\Phi_{i+1} - \Phi_{i-1}) - (\Phi_{i+2} - \Phi_{i-2})] \ / \ 12\Delta y$$

In cases where i is within 1 grid-point of the boundary, a slightly different form is necessary:

$$\frac{\partial \Phi_2}{\partial y} \approx (6\Phi_3 - 3\Phi_2 - \Phi_4 - 2\Phi_1) \ / \ 6\Delta y$$

$$\frac{\partial \Phi_1}{\partial y} \approx (-9\Phi_3 + 18\Phi_2 + 2\Phi_4 - 11\Phi_1) \ / \ 6\Delta y$$

Boundary conditions were managed as follows:

(Mean flows were assumed to be zero at y = yb. Tendencies for u_1, u_2 were computed. Following time integration, η_1, η_2 were determined on the boundary in terms of adjacent values of η_1, η_2 and the new values of u_1 and u_2 on the boundary.

The "leapfrog-trapezoidal" method is a two-step or predictor-corrector method. It was chosen for efficiency and because it does not adversely affect phases and amplitudes of wave-type solutions. For long integrations or those involving frictional processes, however, other

schemes may be preferable. The method is summarized as follows:

let $$\Phi_t^k = \Gamma(\Phi^k)$$

where k represents the time-step and Γ the tendency function.
We define a predicted value:

$$\Phi^* = \Phi^{k-1} + 2\Delta t\Gamma(\Phi^k)$$

where Δt is the time-step size.
The corrected or final value is:

$$\Phi^{k+1} = \Phi^k + \frac{\Delta t}{2} \left[\Gamma(\Phi^*) + \Gamma(\Phi^k)\right]$$

This scheme also has the desirable characteristic of damping the computational mode.

After some experimentation a grid spacing in latitude of 28 km was chosen. Linear stability of the calculation required that the time-step be less than about 3 hours, so a value of 2 hours was chosen and found to be satisfactory. With these step sizes an integration of 2 months (model time) required only about 15 minutes of CPU time and very little core on a UNIVAC 1106.

The six dependent variables computed were decimated to four steps per model day before storage on disk and tape for subsequent plotting and analysis.

The forcing function employed was essentially uniform in latitude. It was tapered off inside the zonal boundaries to prevent the immediate generation of gravity waves which might contaminate the equatorial solution. Time dependence was similar to the latitude

dependence, being a hyperbolic tangent function. The form of the forcing was:

$$G = \tau'[\tanh a(t-t_1) - \tanh a(t-t_2)] * [\tanh b(y-y_1) - \tanh b(y+y_1)]/ 4$$

Where y_1 is the extent in latitude, north and south, and t_1 and t_2 are the onset and decay times, respectively. τ' is the scaled forcing amplitude. This form allows for the application of a pulse-type forcing of any duration. For example, for t_2 60 days, t_1 near zero and a sufficiently large, G approaches a step function in time. The form of the forcing will be shown (Fig. 25) in the individual examples.

The mean flow was taken to be a Gaussian, zonal flow in each layer specified by the parameters $\bar{u}_0$ and Λ.

$$\bar{u}_i = \bar{u}_{0_i} \exp(-y^2/2\Lambda_i^2) \qquad i = 1, 2$$

$\bar{\eta}$ (the pressure field) was chosen to be in geostrophic balance with $\bar{u}$ (recall the third and seventh equations in (2)). Layer thicknesses were specified at the equator so that, in the presence of mean flow, $\bar{\eta}$ increases from zero at the equator (see Fig.26). Λ_i were chosen to be consistent with the observed latitudinal extents of the equatorial currents, thus mean flows were, subsequently, assyptotically zero well within the zonal boundaries.

Since longitudinal dependence of the form e^{ikx} has been assumed, all the dependent variables are complex. This was achieved by using complex FORTRAN variables. Real and imaginary parts of the model output were combined appropriately in later analysis to recover features of the longitudinal structure such as zonal propagation. The forcing function is assumed to have only a real part which is equivalent to a cos(kx)

dependence. The forcing is thus a stationary or standing wave, depending on the temporal dependence.

3.4.2 Cases Studied

The numerical experiments consist of six cases. The density structure in all cases is as described in Chapter 3, Section 1. The cases are as follows:

1. K = 0 Forcing = Step 1
2. K = $2\pi/2400$ km Forcing = Step 1
3. K = $2\pi/2400$ km Forcing = Step 2 Zero mean current
4. K = $2\pi/2400$ km Forcing = Pulse
5. K = $2\pi/2400$ km Forcing = Step 2 Mean current present
6. K = $2\pi/2400$ km Forcing = Pulse

Figure 25 shows the time-dependence for the three forcing functions used. The amplitude or maximum value of windstress is chosen to be 0.25 dyn/cm^2. Since this is a linearized model, i.e., the nonlinear terms are simulated by variable coefficients, the amplitude of the response is directly proportional to the amplitude of the forcing. The response depends in no other way on the forcing magnitude.

Characteristics of mean flow are given below for cases where it is indicated.

$\bar{u}_{0_1}$ = 40 cm/sec. Λ_1 = 300 km

$\bar{u}_{0_2}$ = 40 cm/sec. Λ_2 = 100 km

Horizontal profiles of these flows are shown in Fig.26. In all cases,

integration was carried out for sixty days of model time.

3.4.3 Derived Quantities

In addition to the six dependent variables, several other pertinent quantities were calculated. These include the internal and external modes of the v-component for case 4, total u-component for cases 5 and 6, and near-equatorial v-components as a function of longitude and time. The derivations are now described.

The external and internal modes were found from the appropriately weighted sum of v-components in the two layers. From Section 3.3, we have:

$$\bar{v}^1 \text{ (ext)} = (v_1 + \sqrt{2v_2}) \; / \; 2$$

$$\bar{v}^2 \text{ (int)} = (v_1 - \sqrt{2v_2}) / \; 2$$

The total u-components were found by adding the fluctuation u-components to the prescribed mean flows:

$$u_{1_T} = \bar{u}_1 + u_{1_r}, \; \bar{u}_1 - u_{1_i}$$

$$u_{2_T} = \bar{u}_2 + u_{2_r}, \; \bar{u}_2 - u_{2_i}$$

where u_r, u_i are real and imaginary parts of u respectively.

v-components as functions of longitude and time were derived using averages over a finite latitude band:

$$\langle v_i \rangle = - \frac{1}{2N+1} \sum_{j=-N}^{N} v_{ij} \simeq \frac{1}{2y_0} \int_{-y_0}^{y_0} v_i dy \qquad (i - 1, 2)$$

where $y_o = y_N = 280$ km $\simeq 2.5^o$.

The resulting time series of $\langle v_i \rangle$ were then multiplied by the harmonic longitude dependence, and the real part taken:

$$v_i(x,t) = \langle v_i \rangle_r \cos(kx) - \langle v_i \rangle_i \sin(kx) \quad (i=1,2)$$

where $k = 2\pi/2400$ km; $x = x_j$, $j = 1,121$

$x_{121} - x_1 = 4800$ km or two cycles.

and $dx = x_{j+1} - x_j = 40$ km

3.4.4 Presentation of Results

Results from cases 3 and 6 are shown in Figs. 27-64. Cases 1 and 2 are discussed but plots of output are not included; case 2 is not qualitatively different from case 3; and case 1 is a test run with $k=0$. Most of the indicated plots are latitude-time maps of real and imaginary parts of the six dependent variables, the total u-component and the vertical modes. The remainder (Figs. 33, 34, 43, 44, 53, 54, 63 and 64) are longitude-time representations of near equatorial v-components.

All variables are presented for completeness. Most discussion, however, concerns the meridional components. Latitude-time maps extend from 5°S to 5°N and cover the entire sixty-day integration time. Figure 65 is a second plot of the real part of v_1, case 4, but covering the entire latitude domain. With the exception of some artificial boundary-generated noise near the end of the integration, the response is limited latitudinally to about $\pm 5^{\circ}$. The larger radius of deformation for the system is 267 km or about 2.4° which is indeed consistent with the trapping scale of the model results. There are, in fact, extra-equatorial motions present in the response, e.g., inertial oscillations, but these are at least an order of magnitude

smaller in amplitude than the equatorial response. For these reasons, the $\pm 5^{\circ}$ scale was chosen since it provides a more detailed presentation.

In all the latitude-time plots one can see pronounced, several-week oscillations. In the longitude-time plots, a dominant, westward propagation is evident. A detailed discussion of these plots is given in Chapter 4.

4. DISCUSSION OF RESULTS

4.1 Comparison of Model Results with Linear Theory

To ascertain that the numerical scheme made sense, four runs were made with zero mean flow (Cases 1 - 4, Section 3.4.2). The results of these runs were projected onto the theoretical free modes of the system to determine if the model was consistent with linear theory.

For Case 1, k = 0; for Cases 2 to 4, k = $2\pi/2400$ km. The resulting v-components were first combined to form vertical, normal modes, and the latter then projected onto the horizontal modes, corresponding to the n = 0, 2, 4, 6, 8, 10, 12, and 14 Hermite functions. Projections on odd-order modes are zero, as is to be expected for the prescribed forcing. In Fig. 67, the percentage of variance accounted for by each of these modes is presented. These results show that the majority of the response is confined to the n = 0 mode, or Yanai wave, with percentages tapering off rapidly as n is increased. The Hermite function coefficients which result from this analysis are time series, and have been further analyzed to extract periods and phases in time. The results are in excellent agreement with the dispersion relations derived in Chapter 4.

The analysis procedure is now described.

Let $v_s = \frac{k \langle \tau \rangle}{\rho_1 \beta H_1}$ = Sverdrup transport,

where $\langle \tau \rangle = \frac{1}{T_{max}} \int_0^{T_{max}} \tau \, dt$ (i.e., the average forcing).

Then for $k \neq 0$,

$$v_1(y,t) \equiv v_{1_r}(y,t) + i(v_{1_i}(y,t) + v_s) \equiv v_{1_r}(y,t) + iv_{1_i}(y,t)$$

$$v_2(y,t) = v_{2_r}(y,t) + iv_{2_i}(y,t) ;$$

consequently,

$$v'_{1_r} = v_{1_r} \quad , \quad v'_{1_i} = v_{1_i} - v_s \quad , \quad v'_{2_r} = v_{2_r} \quad , \quad v'_{2_i} = v_{2_i} \quad ,$$

as was found earlier.

Forming the vertical, normal modes:

$$\bar{v}^1 = C_1^1 v'_2 + C_2^1 v_1 \qquad \text{external}$$

$$\bar{v}^2 = C^2{}_1 v'_1 + C_2^2 v'_2 \qquad \text{internal} \quad ,$$

where the C's represent the eigenvectors of the normal mode problem.

Each of these is then projected on the appropriate Hermite functions:

$$\bar{v}^\ell = \sum_{n=0}^{\infty} A_n^\ell \Psi_n^\ell \qquad \ell = 1,2$$

$$C_m^\ell(t) = \int_{-\infty}^{\infty} \Psi_m^\ell \bar{v}^\ell \, dy$$

$$\Psi^\ell = e^{\frac{-y^2}{2(R_d^\ell)^2}} H_n\left(\frac{y}{R_d^\ell}\right) \qquad y = (-\infty, \infty)$$

R_d is such that Ψ is assymptotically zero at $y_b = \pm 15^o$, so the limits of integration are placed here without much loss of accuracy. The $C_m^\ell(\tau)$ constitude time series of Hermite function coefficients.

The variances in Fig. 26 were computed as follows:

$$\rho_m^{\ell} = \frac{1}{T} \int_0^T \int_{-y_b}^{y_b} \frac{(C_m^{\ell}(t))^2}{(\bar{v}^{\ell}(y,t))^2} \, dy \, dt$$

For k = 0, these time series are sinusoidal. The periods agree with those predicted by the dispersion curves unequivocally since, *for each horizontal (and vertical) mode, there is only one frequency.* For $k \neq 0$, however, the series are not simple sinusoids, but rather, composite, periodic signals. The imaginary parts of these series (which were zero everywhere for k = 0) contain components of the same frequencies but of differing phase from those in the real parts. It was necessary, therefore, to extract the frequencies and phases of these components in order to determine the longitudinal propagation and dispersion characteristics.

The dispersion relation (Fig. 23) implies that, for $k \neq 0$, there should be three frequency components for $n \geq 2$, two for n = 0, and one, the Kelvin wave, for n = -1; i.e., for $n \geq 0$, there is an eastward and a westward gravity wave, as well as a Rossby wave. As stated above, we will not consider the Kelvin wave. The numerical solution, after integrating out the structure in latitude as described, may be represented by:

$$v(x,t) = \mathrm{Re} \left\{ (v_r(t) + i v_i(t)) \, e^{ikx} \right\} ,$$

where v_r and v_i are the real and imaginary parts of the model results *projected on a mode.* Assuming that v_r and v_i are linear combinations of harmonic functions in time with frequencies σ_1 and σ_2:

$$v_r = A_r^1 \cos(\sigma_1 t) + B_r^1 \sin(\sigma_1 t) + A_r^2 \cos(\sigma_2 t) + B_r^2 \sin(\sigma_2 t)$$

$$v_i = A_i^1 \cos(\sigma_1 t) + B_i^1 \sin(\sigma_1 t) + A_i^2 \cos(\sigma_2 t) + B_i^2 \sin(\sigma_2 t)$$

Thus, for each frequency, σ_j, we have, after some manipulation:

$$v(x,t)_j = \frac{1}{2}\Big[(A_r^j - B_i^j) \cos(\sigma_j t - kx) + (B_r^j + A_i^j) \sin(\sigma_j t - kx) + (A_r^j + B_i^j) \cos(\sigma_j t + kx) + (B_r^j - A_i^j) \sin(\sigma_j t + kx)\Big]$$

The first two terms correspond to eastward propagation and the last two to westward propagation. The coefficients A_r, B_r, etc. were evaluated from the model results by the method of least squares.

For $n = 0$, there are only two frequencies present. For $n \geq 0$, however, we also have a Rossby wave. Only the two inertio-gravity wave frequencies were explicitly extracted since the Rossby waves were of periods as large as and larger than the integration time. Subsequent visual comparison of original and reconstituted time series ascertained that virtually all short-period variance had been accounted for by σ_1 and σ_2, and that the remainder was a long-period variation consistent with the Rossby wave.

The numerical solution (no mean flow) thus consists of a combination of the free modes of the system with the correct frequencies and propagation directions. Moreover, the greater part of the variance of the response is contained in the lowest order horizontal modes (Fig. 67). A typical response amplitude is 20 cm/sec for v.

Examination of Fig. 67, in conjunction with the three forcing functions (Fig. 25), reveals that the response to the pulsed wind is

confined almost entirely to n = 0 for two modes. For both stepped-wind cases, there is a broader distribution of variance over horizontal modes. In particular, eight horizontal modes account for only 72% of the variance of the internal mode. This broadening can be attributed to the existence of many Rossby wave modes to satisfy initial conditions in the presence of the Sverdrup transport. Only in the stepped-wind cases is this transport non-negligible. For Case 1, where k = 0, 70% of the variance is found in the internal mode. This is consistent with the other stepped-wind cases in that the internal mode is excited more than the external mode by the steady component of the wind. Internal mode frequencies are lower than, and thus, closer to the energy peak in the steady wind. This effect is in addition to the steady-flow effect, which does not exist in Case 1. The reader is reminded at this point that the prescribed forcing is projected equally on the baroclinic modes.

Case 4 is, as a result of these considerations, the preferred case for study of the short-term response because virtually all the variance is confined to two lowest order horizontal modes, and the intermittent, pulse-like forcing is probably more representative of real conditions.

Table 5: Yanai Wave Characteristics for Model Modes

	Period (days)	Phase Speed (cm/sec)	Amplitude (dimensionless) Case 2	Case 3	Case 4	Case 1
External						
westward	16.7	166	0.277	0.189	0.294	
eastward	8.4	329	0.063	0.039	0.072	
Internal						
westward	23.1	120	0.177	0.244	0.297	
eastward	14.7	188	0.073	0.094	0.158	
External	11.9					0.103
Internal	18.5					0.163

Table 5 contains amplitudes of Yanai wave components for each of the four cases discussed. For Case 1 ($k = 0$), these amplitudes merely reflect the previous argument concerning internal and external modes since there is only one wave in each. In the other cases, however, there is, in addition, a systematic difference between the amplitudes of westward- and eastward-propagating waves: the amplitudes of the westward waves are always the larger. This can be explained by inspection of the dispersion diagrams (Fig. 23) and Table 5 and by noting that the phase speed, σ/k, is about twice as large for the eastward branch of the Yanai wave. Consequently, the westward wave, with slower phase speed, tends to absorb more energy before it propagates sufficiently far to be out of phase with the stationary forcing.

In summary, of all components appearing in the response, the dominant one is the Yanai wave, particularly the westward-propagating branch, with both external and internal modes of similar magnitude. The longitude-time plots for Cases 3 and 4 (Figs. 33, 34, 43, and 44) show a dominant, westward-propagating disturbance superimposed by beat patterns related to the frequency differences between internal and external modes and by interference from eastward-propagating waves. In Case 3 (Fig. 33), in the upper layer, the picture is further complicated by the presence of steady flow (Sverdrup flow) and Rossby waves.

Phase speeds were extracted for the dominant, westward- and eastward-propagating features directly from the plots (Table 6). These values agreed with those of the dominant, theoretical mode in each case.

Cases 5 and 6, which include mean current, are not analyzed by the foregoing techniques because vertical, normal modes cannot be defined

in the same way . It is necessary, therefore, to make direct comparisons of plots of output to estimate the effects of the advective terms.

Table 6: Phase Speeds (cm/sec) Extracted from Longitude-Time Maps; Pulsed Forcing

	Case 4 (no mean flow)			Case 6 (mean flow)		
	Upper	Lower	Average	Upper	Lower	Average
Westward	152	142	147	186	159	173
Eastward	200	186	193	174	186	180

4.2 Effects of Mean Current

Examination of longitude-time plots for Cases 5 and 6 (Figs. 53, 54, 63, and 64) indicates that westward-propagating disturbances dominate even more than in linear cases. Average westward phase speeds tend to be increased, while eastward phase speeds tend to be decreased. This difference may constitute a Doppler shift associated with the current in the upper layer. The reason that the Undercurrent has a much smaller effect in this shift is that it is narrower than the smaller of the two radii of deformation, and thus, has only a secondary Doppler-shifting effect, while the width of the current in the upper layer is greater than the larger R_d. Phase speeds derived from x-t plots for Cases 3 to 6 are recorded in Table 6. The Doppler-shift described above tends to cause the frequencies of the eastward and westward waves to be closer together. These results should be viewed as qualitative since the average phase speeds derived from the plots are only approximations. In short, the Doppler effect produces

a signal which is closer to containing a single frequency. Indeed, in the latitude-time maps of lower-layer v-components (Figs. 32, 39, 50, and 60), the signal seems to be more nearly simple harmonic in time than in the linear cases. However, while some apparent Doppler effects have been noticed, the concept is limited in this situation since the latitudinal scale of the waves is of the same order as that of the zonal currents.

The amplitudes in the mean flow cases tend to be greater than in the other cases. This implies an initial transfer of momentum and energy from the mean current to the fluctuations, but does not necessarily constitute an instability. An instability would require that the amplitudes grow with time. It might be said that the interaction with the mean current is an amplification of the forcing signal. It is likely that the proper choice of mean flow parameters would yield an instability for the forcing and wavelength used. This problem has been addressed by Philander (1976) for a very similar system, but will not be examined here.

The immediate effects of the mean current through non-linear interaction can best be seen in Figs. 29, 36, 47, and 57. The signs of $v\bar{u}_y$ are such that negative fluctuations in u (north of the equator) in the upper layer and positive fluctuations in the lower layer are enhanced, while fluctuations of the opposite signs are suppressed.

The presence of mean zonal currents with horizontal shear modify the responses in the cases considered, but the picture is still one of equatorially trapped waves with much the same structure as in cases

without mean flow. These results suggest that the system responds with periods and spatial scales which are determined primarily by the basic system parameters, namely, the density structure. While it is likely that values of east-west wavenumber and mean flow parameters can be found for which the response is entirely different, e.g., unstable, small deviations from the chosen values will have much the same results as those presented.

4.3 Comparison of Observations with Theoretical and Numerical Results

As discussed in Chapter 2, considerable caution is required in the inference of wave parameters from GATE observations. The implications are actually that certain scales of motion are observed more frequently than others. Even the results of one of the previously discussed model runs, with or without mean flow if sampled in the same fashion as GATE observations were made, would provide somewhat ambiguous results. With these limitations in mind, the following arguments are presented.

Since the best estimate of a wave parameter from the observations is the 16-day period, marks on the σ-axes (see Fig. 23) corresponding to this value show that, in the external mode, only the westward-propagating Yanai wave and the Kelvin wave curves are intersected. For baroclinic modes whose equivalent depths exceed that of the external mode of the model ($\bar{H}$ = 27.3 cm) up to a maximum that would be expected in the tropical ocean, say about 200 cm, this result holds. Thus, for the lower baroclinic modes, a 16-day wave would have a phase speed between about 120 and 200 cm/sec and a wavelength between

1700 and 2700 km. For higher baroclinic modes, such as the internal mode of the model, the eastward-propagating Yanai wave becomes a possibility. These results are summarized in Fig. 24, which contains plots of period vs. phase speed for several equivalent depths for the Yanai wave. Also plotted are curves of constant wavelength. The rectangle superimposed on the curves for the westward wave represents the ranges of these quantities inferred from the observations for the n = 0 case in Table 5. The plot suggests that the observed wave parameters are consistent with the first or second baroclinic mode in the continuously stratified case and for the external mode of the 2½-layer system under consideration. Phase speeds for other values of n in Table 5 are too low to be in agreement with linear theory. It is possible, however, that an eastward-propagating Yanai wave of smaller amplitude is present and may be responsible for the assymmetry observed in the y-t maps (e.g., Fig. 3). Indeed, when the results of the numerical integrations were analyzed, such was found to be the case. As shown in Section 2.2, there are indications that shorter period fluctuations exist in the observations. These appear to have periods between 5 and 10 days. Figure 23 shows that such periods are consistent with n = 2 inertio-gravity waves for a wavelength of from 2000 to 2500 km for the first several baroclinic modes and the external model mode. Consideration of the Kelvin wave, at least for the major fluctuation, is ruled out since it requires v to be zero. In fact, all odd-order Hermite functions are zero at the equator. Unfortunately, phase speeds cannot be estimated for these shorter period fluctuations from the observations. Sea-level measurements in the equatorial Pacific

analyzed by Wunsch and Gill (1976) show the existence of first baroclinic mode equatorial waves with periods of the order of four days. Wunsch and Gill also present an argument for the existence of meridionally forced Yanai waves.

In summary, it has been shown that the wave parameters estimated from the observed current records are consistent with the free solutions of the linear, equatorial wave problem for at least the westward-propagating Yanai wave for low-order baroclinic modes.

Comparison of model results with and without mean current indicates that the response is wavelike in either case, thus making the comparison with linear, free modes more meaningful. Comparison of observations with model results where the mean flow is included is also necessary, however. One case is selected for comparison as being most representative of real conditions.

Previous descriptions (Section 2.4) of observed winds during GATE imply that the pulsed wind (Cases 4 and 6) is probably the simplest realistic approximation to real conditions for examining short-term responses. In any case, it has been shown that a wavelike response results for step-like forcing as well as the pulse.

The model results, in conjunction with the theoretical analysis of the linear problem, suggest that the oscillations of the Undercurrent constitute a north-south advection by a predominantly wavelike process. This conclusion would be apparent in the observations if the north-south or trapping scale of the v-component were much greater than the width of the Undercurrent. However, based on observations alone, it is not obvious whether the oscillations are primarily wavelike, as

described, or are manifestations of an inertial jet phenomenon. The latter hypothesis is weakened if the zonal flow is assumed to be geostrophically balanced, and the pressure field, as well as the flow field, experiences the same initial disturbance; i.e., the lateral, Lagrangian motion of a free jet might be described by the following:

$$\frac{dv_c}{dt} + \beta y u_0 = 0 \quad ,$$

where u_0 is the eastward speed of the jet and v_c is the northward velocity of the position of the core.

For u_0 = 80 cm/sec,

$$T = \frac{2\pi}{\sqrt{\beta u_0}} = 17 \text{ days.}$$

If, however, u_{0g} is the geostrophic part of u_0, then

$$\beta y u_{0g} = -p_y \quad ,$$

which greatly increases T if $u_0 - u_{0g}$ is taken to be a perturbation. This argument is presented as a caution against an over-simplified, free-jet hypothesis.

A point concerning the actual forcing is worth mentioning. In the model, the system is initially at rest, so all subsequent motion can be attributed to the known applied forcing. In the observations, however, a small segment of an ongoing process is being examined, and our attempts to correlate the local winds with the currents may be

somewhat naive. If the observed fluctuations are indeed produced by the mechanisms implied by the model, it is more likely that they were excited by a pulse or periodic wind further to the west and previous to the current observations. This is implicit in the model results since the most energetic part of the lower layer response is initially in the imaginary part, or ¼-wavelength away from the peak in the forcing. Thus, at any given time of observation, the response at a given location is probably a combination of the effects of local forcing and previously excited waves which propagated into the area.

A comparison of v-components (Figs. 13, 14, 59, and 60) shows that amplitudes and times of zero-crossings are in remarkable agreement. It may be re-emphasized that the choice of parameters, both for the density structure and for the mean current, is not critical to this agreement. The choices were based on observations and adjustments were not made. The total u-components (Figs. 13, 14, 61, and 62) are also very similar. In particular, the maximum displacement of the Undercurrent core is seen to be nearly the same in both observations and model results. In the latter case, this depends to some extent on the magnitude of the forcing, but is affected by R_d as well. Due to the fact that the mean fields in the model are fixed, no changes in u or η result at the equator for the prescribed forcing. Thus, shifts of the Undercurrent are represented by changes in u off the equator.

Figures 66 a and b show equatorial, meridional transports calculated from the imaginary parts of the v-components in the model output, with and without mean current. These are compared with plots of the

same calculation done for the observations (Fig. 19). This comparison shows the similarity in the phase relations of the two layers, which, in turn, suggests similarity in the dynamic processes.

In general, amplitudes in the observations tend to be higher than those in the model. This is likely to be due to the choice of windstress; thus, the discrepancy need not be of undue concern. The difference is more pronounced when comparing vertical motions. An estimate of vertical motion implied by the model results can be found by examining Fig. 52. The pattern is periodic, just as with the observations, and the magnitude is simply the time-derivative of the interface elevations. (Advective effects cause, at most, a factor of two difference.) Where the observations imply vertical motions of the order of 5×10^{-2} cm/sec, the model implies values nearer to 10^{-3} cm/sec. This may be partially due to the oversimplification of the shear zone by the two-layer approximation. Another, more likely explanation is that there may be additional waves present in the observations, e.g., Kelvin waves, which have a maximum in w at the equator. For even modes, w is zero at the equator. For example, in cases where Kelvin and Yanai waves are additive, considerably higher magnitudes in w would result.

4.4 Future Research Suggested by the Present Investigation

During the course of this investigation, primarily in the latter stages when it became clear that the response remained wavelike in the presence of a mean current, certain new questions arose. Some of them, such as that concerning longitudinal propagation and the effects of zonal boundaries, cannot be addressed with the model in its present

form; i.e., explicit x-dependence would have to be introduced. On the other hand, there are a few questions which are natural extensions of this work which are now briefly discussed.

One question which arose during the GATE Miami Workshop (March, 1977) concerned dispersion characteristics in the presence of mean flow. Although for certain mean flow profiles a perturbation theory might be developed to analytically derive a dispersion relation, a more direct, empirical approach, which could be made with the model in this study, is to run the model for a series of values of the east-west wavenumber and, subsequently, to determine frequencies by spectral analysis of the results. This would be done for several mean flow configurations and, at first, an impulse-like forcing function to suppress longer-period Rossby waves.

A second problem of interest is that of the energetics of the system. Cane (1975) addressed this problem in his model calculations, providing an indication of how it should be approached. It would be useful to calculate the total (spatially integrated) accumulated kinetic and available potential energies as a function of time. Juxtaposed with these should be calculations of cumulative work done, as a function of time, by the various flux and exchange terms in the energy equation, e.g., input of energy by wind, contribution from mean flow, work done against pressure forces, etc. This would provide, among other things, a way to assess the effects of the mean zonal current on the dynamics of the system. An example of where this might be particularly useful is when parameters are adjusted so that an unstable wave will develop. In this case, the contribution of energy from the mean flow should be positive throughout the integration.

A series of experiments, similar to those already done, but using instead a zonal forcing, should result in odd-order modes, or modes involving anti-symmetric v-components, including Kelvin waves.

There are many permutations that could be tried, but since the model is highly idealized, emphasis should be on gross aspects of relevant cases and not on differences of results for many slightly different sets of parameters. It is felt that a problem including continuous vertical dependence should be studied to better understand the effects of atmospheric forcing in the light of vertical energy flux.

5. CONCLUSIONS

In Chapter 2, it was shown that there is evidence for the existence of energetic, several-week oscillations in the Atlantic equatorial current system. While it is difficult to determine accurately periods or wavelengths, it appears that two to three weeks is a reasonable estimate of the former. In the absence of any definitive observations, a longitudinal wavelength of several thousand kilometers is indicated through a rather indirect argument.

Subsequent analysis of current velocity data reveals that advective effects were important and all fields were highly time-dependent during GATE. This result suggests that the concept of a steady equatorial current system with a corresponding steady meridional flow with upwelling at the equator may have to be modified, and that it may be quite difficult to determine such quantities as mean, vertical velocity observationally.

The presence of 2- to 3-week wind fluctuations over the equatorial Atlantic during GATE suggests that the current fluctuations may be wind-excited. Investigation of a simple, two-layer, baroclinic system shows that oscillations similar to those observed can be excited by impulsive meridional forcing. The model response is a resonance phenomenon rather than a purely passive response to local forcing. That is, the characteristics of the response are determined chiefly by system parameters, as opposed to forcing characteristics. The response is thus composed of the free modes of the system. In the absence of mean currents, the free modes excited are completely consistent with the theory of

equatorially trapped waves, and furthermore, most of the energy of the response is found in the several gravest modes of the system. The presence of mean zonal flows tends to enhance and modify the response, but does not change its essentially wavelike character. The chief component of the response (termed a Yanai wave in the case without mean flows) appears to play a role similar to that of inertial oscillations in time-dependent, mid-latitude response problems.

While the presence of a free-mode oscillation in the equatorial ocean could be the result of a more indirect forcing (e.g., a wave to wave interaction at a meridional boundary), wind-forcing is as likely to be responsible as anything else. It should be apparent that, even with the very simple model described in Chapters 3 and 4, the combined effects of several impulses at different times and with different wavelengths would result in a very complex mixture of waves. It is, therefore, not surprising that the picture emerging from GATE is rather complex.

REFERENCES

Brown, O. B. and K. Boigt (1975) Meander Motions in the Equatorial Atlantic. GATE Report No. 14, Vol. I: 333-337, WMO, Geneva.

Brown, O. B. (1977) Large-Scale Equatorial Surface Thermal Anomalies as Observed by the GOES Satellite. Abstract of Presentation at the International Workshop on "The GATE Equatorial Experiment," 28 Feb. to 10 March 1977, Miami, Fla.

Brown, O. B., R. H. Evans, and W. Düing (1977) GATE Data Report (in preparation).

Bubnov, V.A., V. D. Egorikhin, and K. V. Moroshkin (1975a) New Data on Water Dynamics in the Equatorial Atlantic. GATE Report No. 14, Vol. I: 327-332. WMO, Geneva.

Bubnov, V. A., V. D. Egorikhin, and K. V. Moroshkin (1975b) On Variability of Water Temperature in the Equatorial Atlantic. GATE Report No. 14, Vol. I: 320-322. WMO, Geneva.

Bubnov, V.A., V. M. Vasilenko, and L. M. Krivelevich (1976) Low-Frequency Oscillations of Current Velocity (According to the Data of the GATE Expedition) Report of the Workshop on General Circulation of the Tropical Atlatnic and the C and B-Scale Oceanic Boundary Layer, Brest. WMO, Geneva

Cane, M. A. (1975) A Study of the Wind-Driven Ocean Circulation in an Equatorial Basin. Ph.D. Dissertation, Massachusetts Institute of Technology, 377 pp.

Cane, M. A. and G. G. Sarachik (1976) Forced Baroclinic Ocean Motion. Jour. Mar. Res., 34 (4): 627-665.

Charney, J. G. (1960) Non-Linear Theory of a Wind-Driven Homogenous Layer near the Equator. Deep-Sea Res., 6: 303-310.

Charney, J. G. and S. L. Spiegel (1971) The Structure of Wind-Driven Equatorial Currents in a Homogenous Ocean. Jour. Phys. Oceanogr., 1: 149-160.

Düing, W. O., Ph. Hisard, and J. K. Low (1975) Current Profiling Observations by the R/V Capricorne. GATE Report No. 14, Vol. I, 338-340. WMO, Geneva.

Düing, W. O. and R. H. Evans (1975) Long Westward Waves in the Upper Equatorial Atlantic. GATE Report No. 14, Vol. I: 310-319. WMO, Geneva.

DÜing, W. O., Ph. Hisard, E. Katz, J. Meincke, L. Miller, K. Moroshkin, S. G. H. Philander, A. Rybnikov, K. Voigt, and R. Weisberg (1975) Meanders and Long Waves in the Equatorial Atlantic. Nature, 257 (5524): 280-284.

Gill, A. E. (1971) The Equatorial Current in a Homogeneous Ocean. Deep-Sea Res., 18: 421-431.

Gill, A. E. (1975) Models of Equatorial Currents. Numerical Models of Ocean Circulation, NAS: 181-203.

Groves, G. W. and M. Miyata (1967) On Weather-Induced Long Waves in the Equatorial Pacific. Jour. Mar. Res., 25: 115-120.

Gruber, A. (1974) The Wavenumber Frequency Spectra of Satellite-Measured Brightness in the Tropics. Jour. Atmos. Sci., 31: 1675-1680.

Hallock, Z. R. and K. V. Moroshkin (1975) Fluctuations in the Vertical Structure of the Atlantic Equatorial Undercurrent. GATE Report No. 14, Vol. II: 324-327. WMO, Geneva.

Haltiner, G. J. (1971) Numerical Weather Prediction. John Wiley and Sons, Inc.

Hubert, L. W. (1975) Evaluation of the New Wind Data from SMS-1. Paper presented at the 9th Technical Conference on Hurricanes and Tropical Meteorology. Abstract Published in Bull. Amer. Meteor. Soc., 56: 316.

.....and L. F. Whitney, Jr. (1974) Compatibility of Low Cloud Vectors and Rawins for Synoptic Scale Analysis. NOAA Tech. Rept. NESS 70: 1-26 (Available from National Technical Information Service, Springfield, VA.)

Hurlburt, H. and D. Thompson (1976) A Numerical Model of the Somali Current. Jour. Phys. Oceanogr., 6 (5): 648-664.

Jones, J. H. (1973) Vertical Mixing in the Equatorial Undercurrent. Jour. Phys. Oceanogr., 3: 286-296.

Katz, E. (1977) Zonal Pressure Gradient during GATE. Jour. Mar. Res. (in press).

Keshavamurty, R. N. (1972) On the Vertical Tilt of Monsoon Disturbances. Jour. Atmos Sciences, 29: 993-995.

Knauss, J.A. (1961) Measurements and Observations on the Cromewell Current. Deep-Sea Res., 6: 265-286.

Knauss, J.A. (1966) Further Measurements and Observations on the Cromwell Current. Jour. Mar. Res., 24: 205-240.

Kousky, V. E. and J. M. Wallace (1971) On the Interaction between Kelvin Waves and the Mean Zonal Flow. Jour. Atmos. Sci., 28: 162-169.

Krishnamurti, T. N., S. M. Daggupaty, J. Fein, M. Kananutsu, and J. D. Lee (1973) Tibetan High and Upper Tropospheric Tropical Circulation during Norther Summer. Bull. Amer. Meteor Soc., 51: 1234-1239.

Krishnamurti, T. N. and C. E. Levy (1975a) Low-Level Fluctuations Over the GATE. Florida State University Report # 75-6.

Krishnamurti, T. N., C. E. Levy, and H. L. Pan (1975b) On Simultaneous Surges in the Trades. Jour. Atmos. Sciences , 32 (12): 2367-2370.

Krishnamurti, T. N., V. Wong, H. Pan, G. van Dan, D. Mockellan (1976). Florida State University Report #76-3.

Lighthill, M. J. (1969) Dynamic Response of the Indian Ocean to the Onset of the Southwest Monsoon. Ph. Tr. R. Soc. L. A-265: 45-92.

Matsuno, T. (1966) Quasi-Geostrophic Motions in the Equatorial Area. Jour. Met. Soc. Japan, 44: 25-43.

McKee, W. D. (1973) The Wind-Driven Circulation in a Homogeneous Ocean. Deep-Sea Res., 20: 889-899.

Meincke, J. (1975) Time-Variations of the Upper Equatorial Current System in the Atlantic Ocean (Preliminary Results). GATE Report #14, Vol II: 341-344 . WMO, Geneva.

Miller, L. (1977) Temperature Data from R/V TRIDENT. Abstract of Presentation at the International Workshop on "The GATE Equatorial Experiment," 28 February to 10 March 1977, Miami, Florida.

Moore, D. W. (1968) Planetary-Gravity Waves in an Equatorial Ocean. Ph.D. Dissertation, Harvard University, 201 pp.

Moore, D. W. and S. G. H. Philander (1975) Modeling of the Equatorial Oceanic Circulation. The Sea, 6(8): 319-362. John Wiley & Sons.

Mikhailova, E. N. and N. B. Shapiro (1972) Certain Problems in the Nonlinear Theory of Equatorial Currents. Izvestiya, 8(7): 720-739.

Murakami, T. and F. P. Ho (1972) Spectrum Analysis of the Cloudiness over the Pacific. Jour. Meteor. Soc. Japan, 50: 285-311.

O'Brien, J. J. and H. E. Hurlburt (1974) An Equatorial Jet in the Indian Ocean. Science, 189: 1075-1077.

Philander, S. G. H. (1973a) The Equatorial Thermocline. Deep-Sea Res., 20: 69-86.

Philander, S. G. H. (1973b) Equatorial Undercurrent: Measurement and Theories. Rev. Geophys. and Space Phys., 2(3): 513-570.

Philander, S. G. H. (1976) Instabilities of Equatorial Currents. Jour. Geophys. Res., 81 (21): 3725-3735.

Ramage, C. S. (1971) Monsoon Meteorology. Academic Press, 296: see p. 45.

Rinkel, M. O. (1965) Cruise Report, University of Miami: #P-6503, Equalant V.

Robinson, A. R. (1966) An Investigation into the Wind as the Cause of the Equatorial Undercurrent. Jour. Mar. Res., 24: 179-204.

Stalcup, M. C. and W. G. Metcalf (1966) Direct Measurements of the Atlantic Equatorial Undercurrent. Jour. Mar. Res., 24: 44-55.

Tripoli, G. J. and T. N. Krishnamurti (1975) Low-Level Flows Over the GATE Area during Summer, 1972. Mon. Wea. Rev., 103: 197-216.

TROPEKS '74 (1976) Gidrometeoizdat Leningrad, 234 pp.

Veronis, G. (1960) An Approximate Theoretical Analysis of the Equatorial Undercurrent. Deep-Sea Res., 6: 318-327.

Wallace, J. M. and C. P. Chang (1969) Spectral Analysis of Large-Scale Wave Disturbances in the Tropical Lower Troposphere. Jour. Atmos. Sci., 26: 1010-1025.

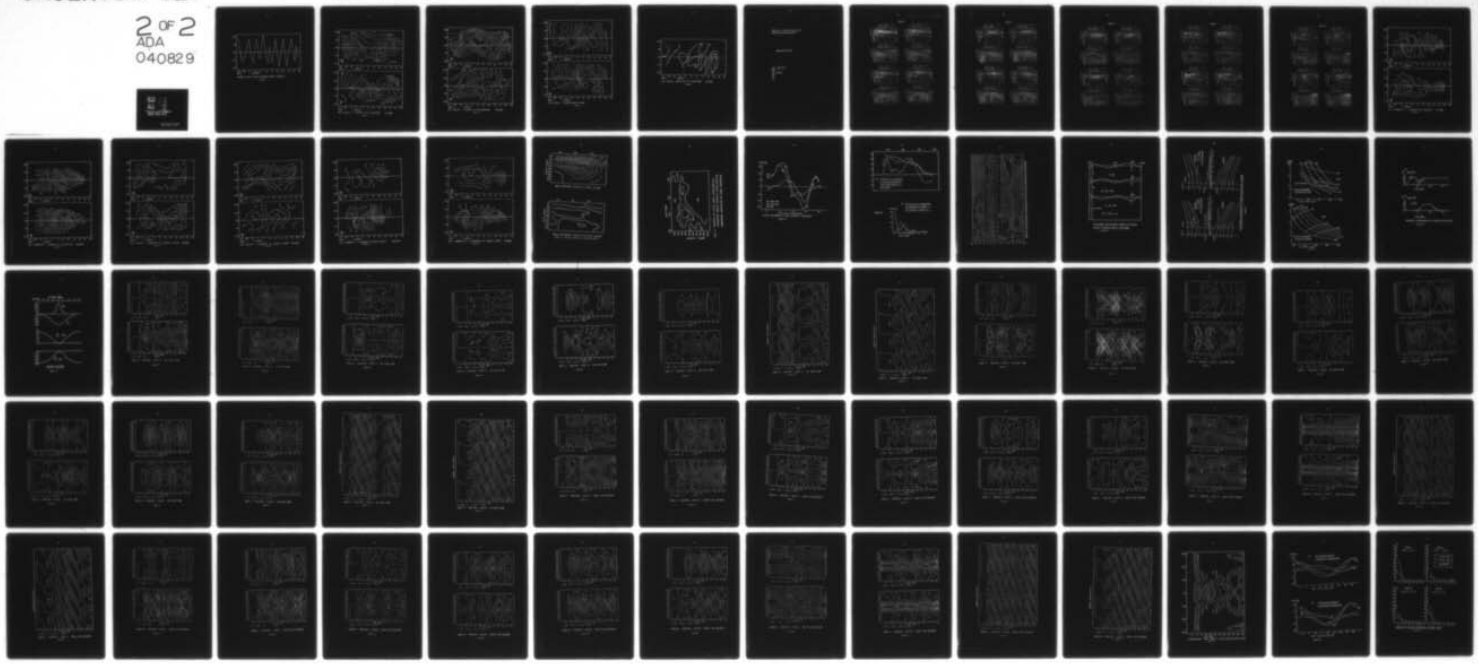
Wunsch, C. and A. E. Gill (1976) Observations of Equatorially Trapped Waves in Pacific Sea Level Variations. Deep-Sea Res., 125 (5): 371-390.

Yanai, M and M. Murakami (1970) A Further Study of Tropical Wave Disturbances by the Use of Spectrum Analysis. Jour. Meteor. Soc. Japan, 48: 185-197.

AD-A040 829 ROSENSTIEL SCHOOL OF MARINE AND ATMOSPHERIC SCIENCE --ETC F/G 8/3
WIND-FORCED EQUATORIAL WAVES IN THE ATLANTIC OCEAN.(U)
MAY 77 Z R HALLOCK N00014-75-C-0173

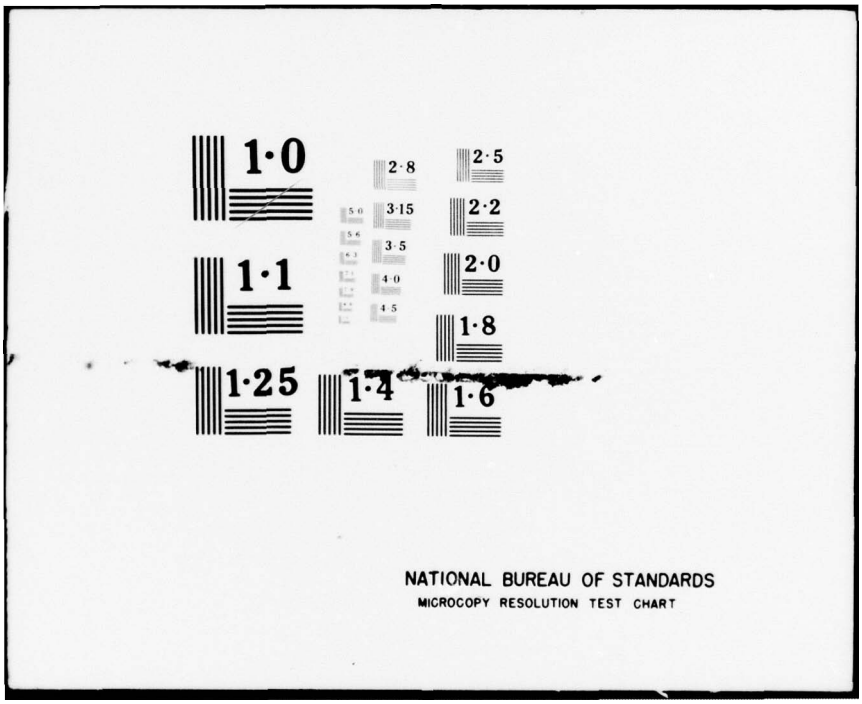
UNCLASSIFIED TR-77-2 NL

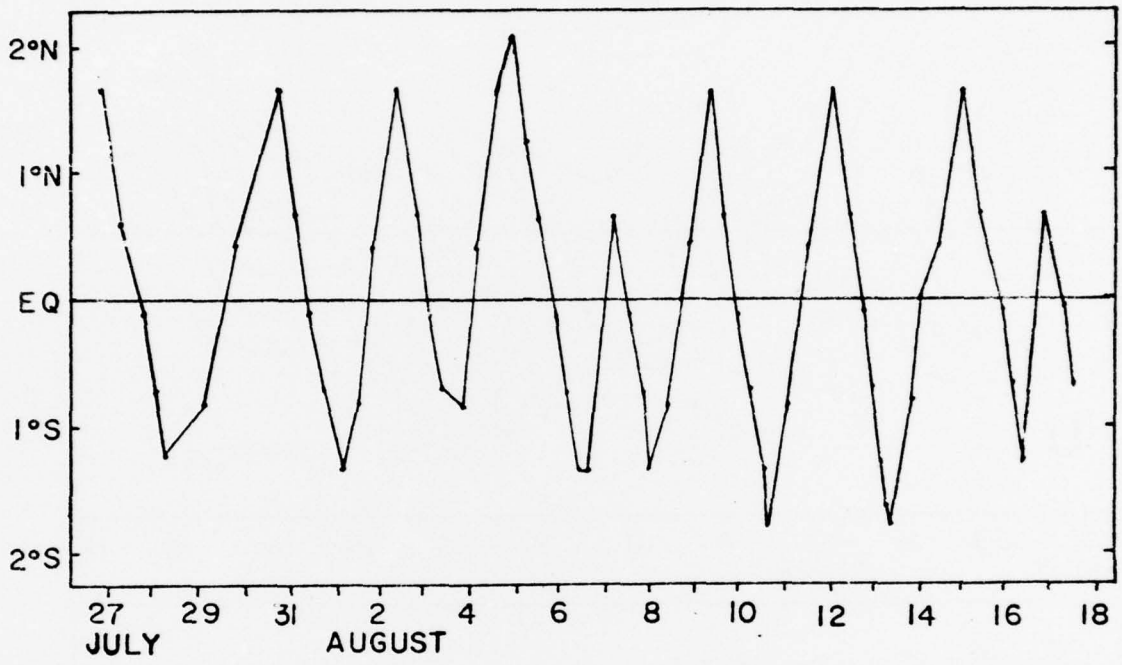
2 OF 2
ADA
040829



END

DATE
FILMED
7-77


1·0
1·1
1·25
1·4
1·6
1·8
2·0
2·2
2·5
2·8
3·15
3·5
4·0
4·5
5·0
5·6
6·3
NATIONAL BUREAU OF STANDARDS
MICROCOPY RESOLUTION TEST CHART



TRACK OF R/V ISELIN DURING GATE, PHASE II

Figure 1

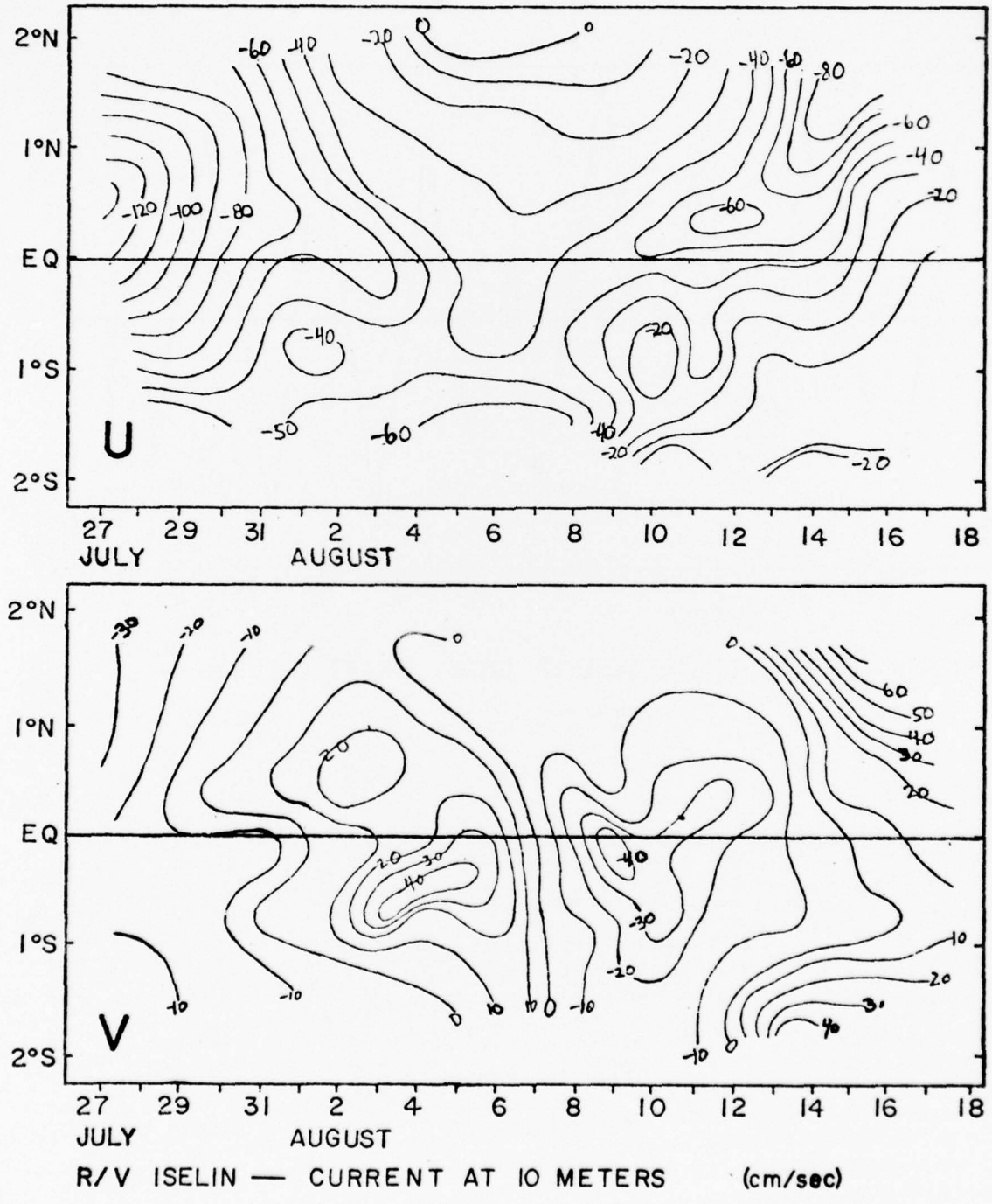

2°N
1°N
EQ
1°S
2°S
U
V
27
29
31
2
4
6
8
10
12
14
16
18
JULY
AUGUST
R/V ISELIN — CURRENT AT 10 METERS (cm/sec)

Figure 2

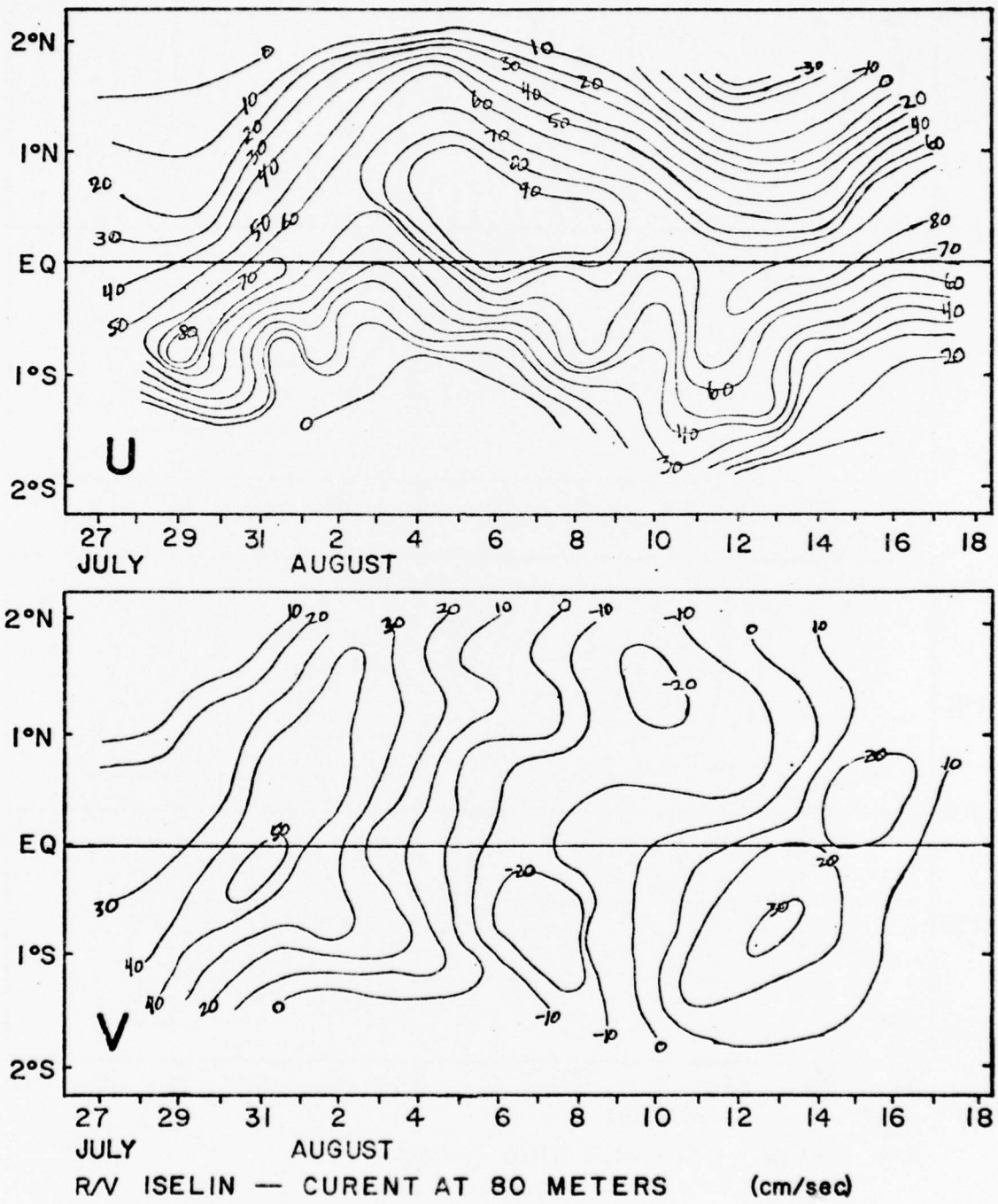

2°N
1°N
EQ
1°S
2°S
U
27 29 31 2 4 6 8 10 12 14 16 18
JULY AUGUST
2°N
1°N
EQ
1°S
2°S
V
27 29 31 2 4 6 8 10 12 14 16 18
JULY AUGUST
R/V ISELIN — CURENT AT 80 METERS (cm/sec)

Figure 3

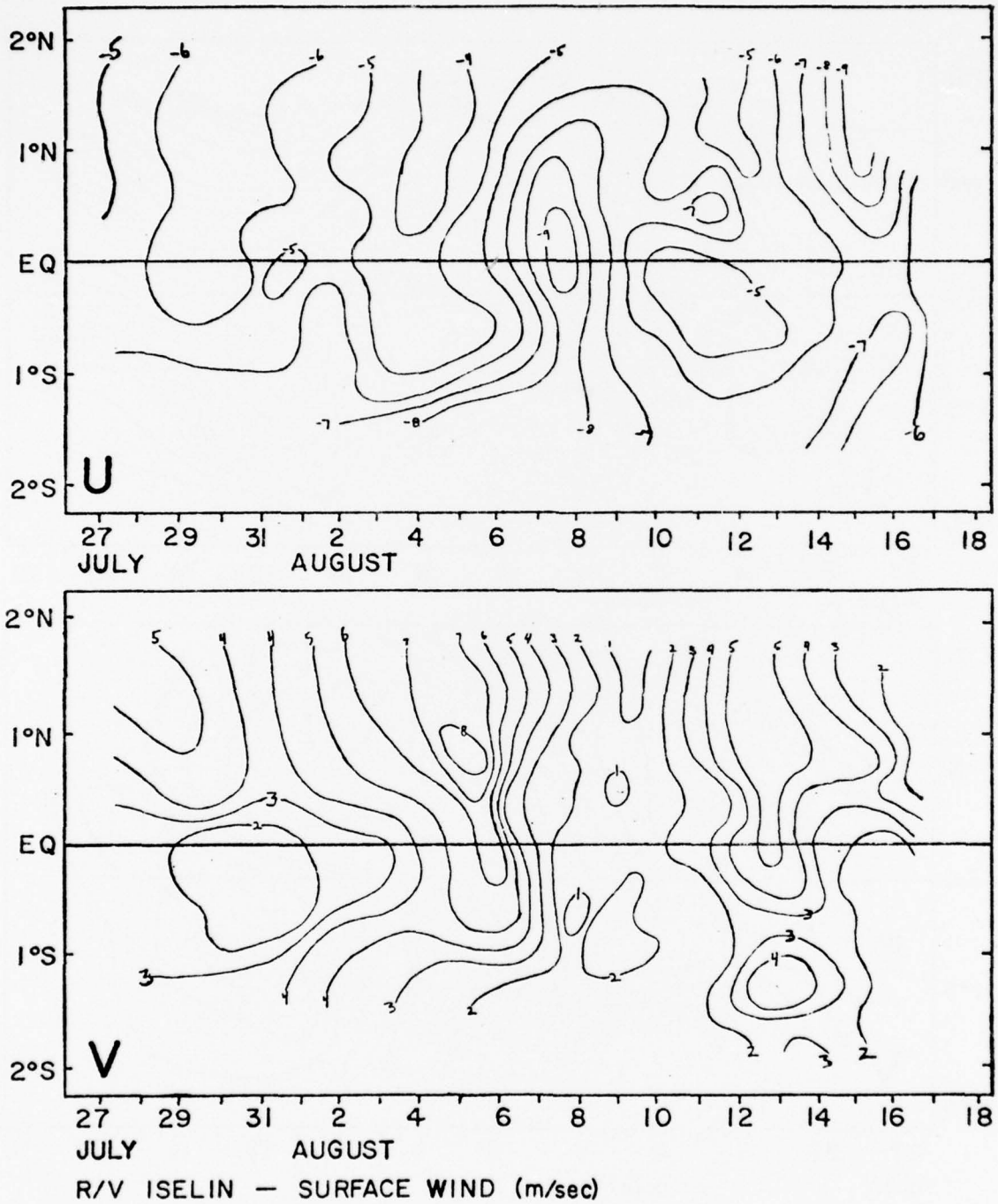

2°N
1°N
EQ
1°S
2°S
U
27 29 31 2 4 6 8 10 12 14 16 18
JULY AUGUST
2°N
1°N
EQ
1°S
2°S
V
27 29 31 2 4 6 8 10 12 14 16 18
JULY AUGUST
R/V ISELIN — SURFACE WIND (m/sec)

Figure 4

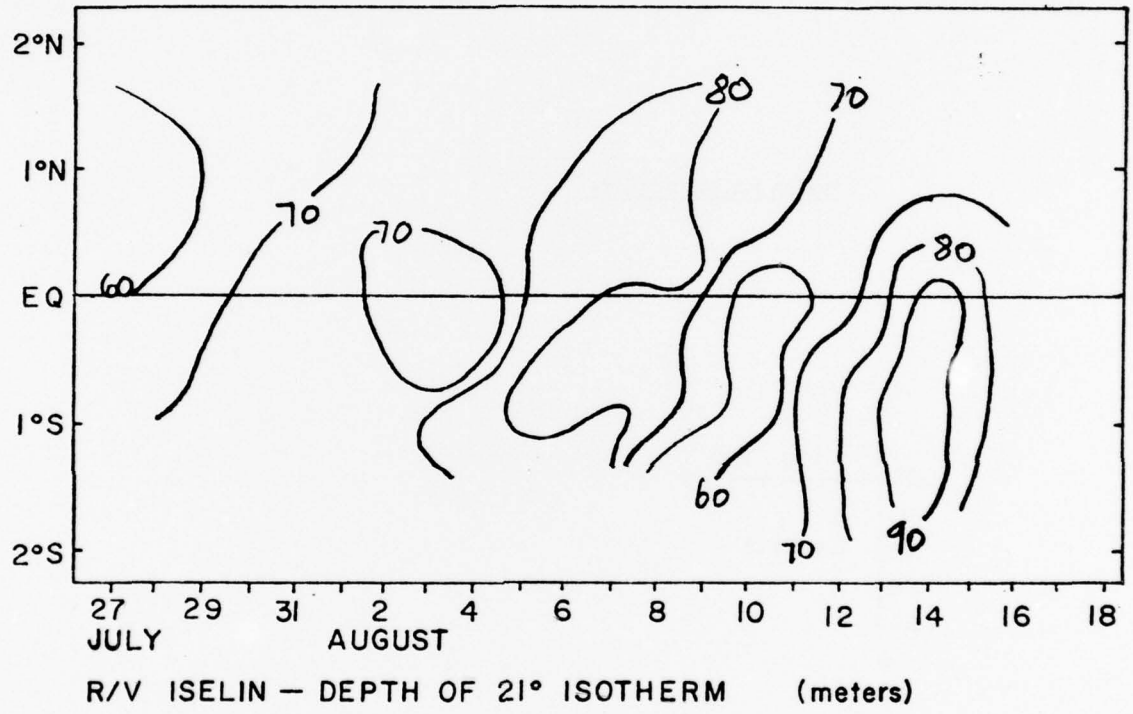
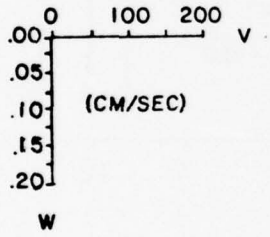

2°N
1°N
EQ
1°S
2°S
60
70
70
80
70
60
70
80
90
27
29
31
2
4
6
8
10
12
14
16
18
JULY
AUGUST
R/V ISELIN — DEPTH OF 21° ISOTHERM (meters)

Figure 5

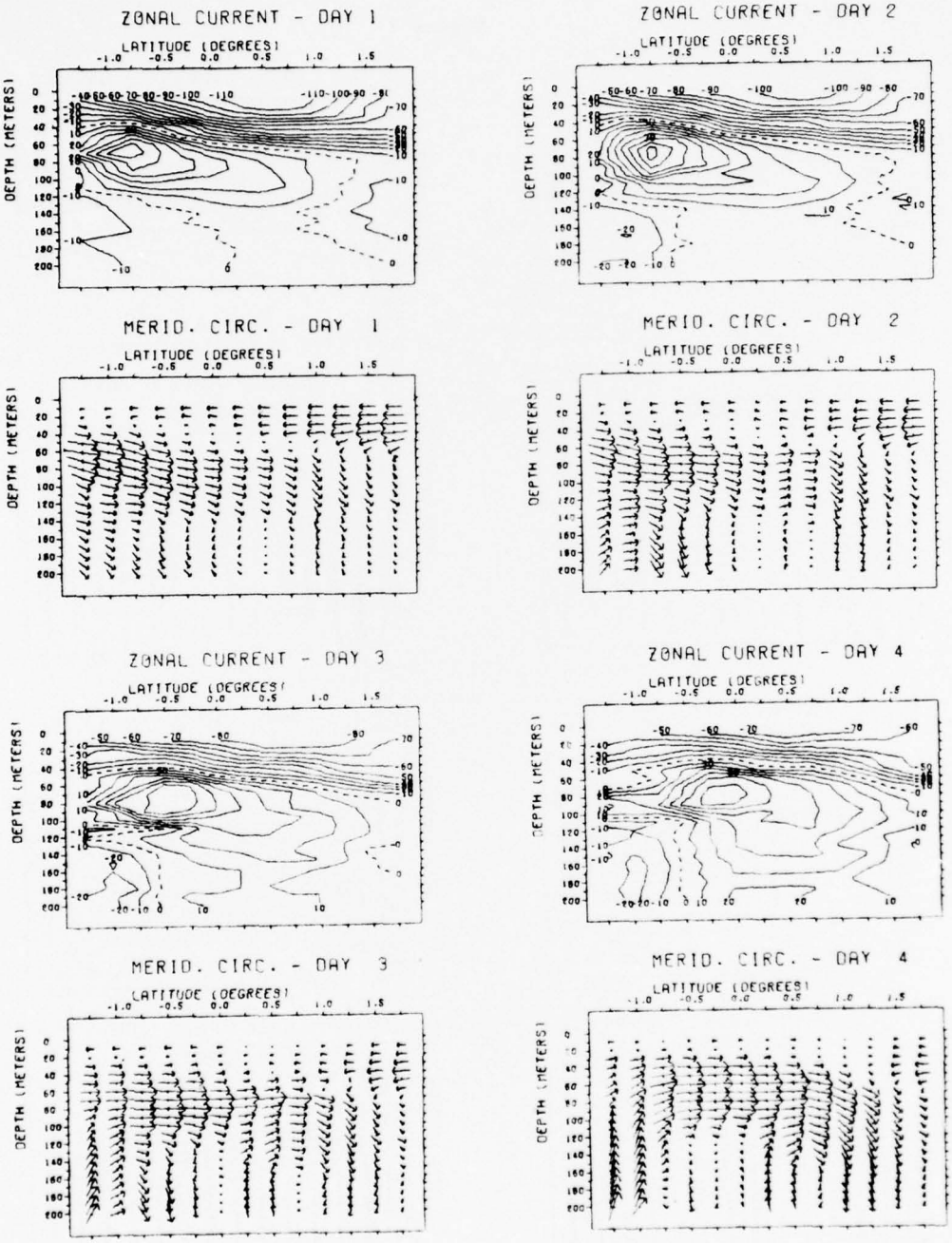
Figures 6-10: Vertical sections of zonal current and meridional circulation

Scales for vector plots



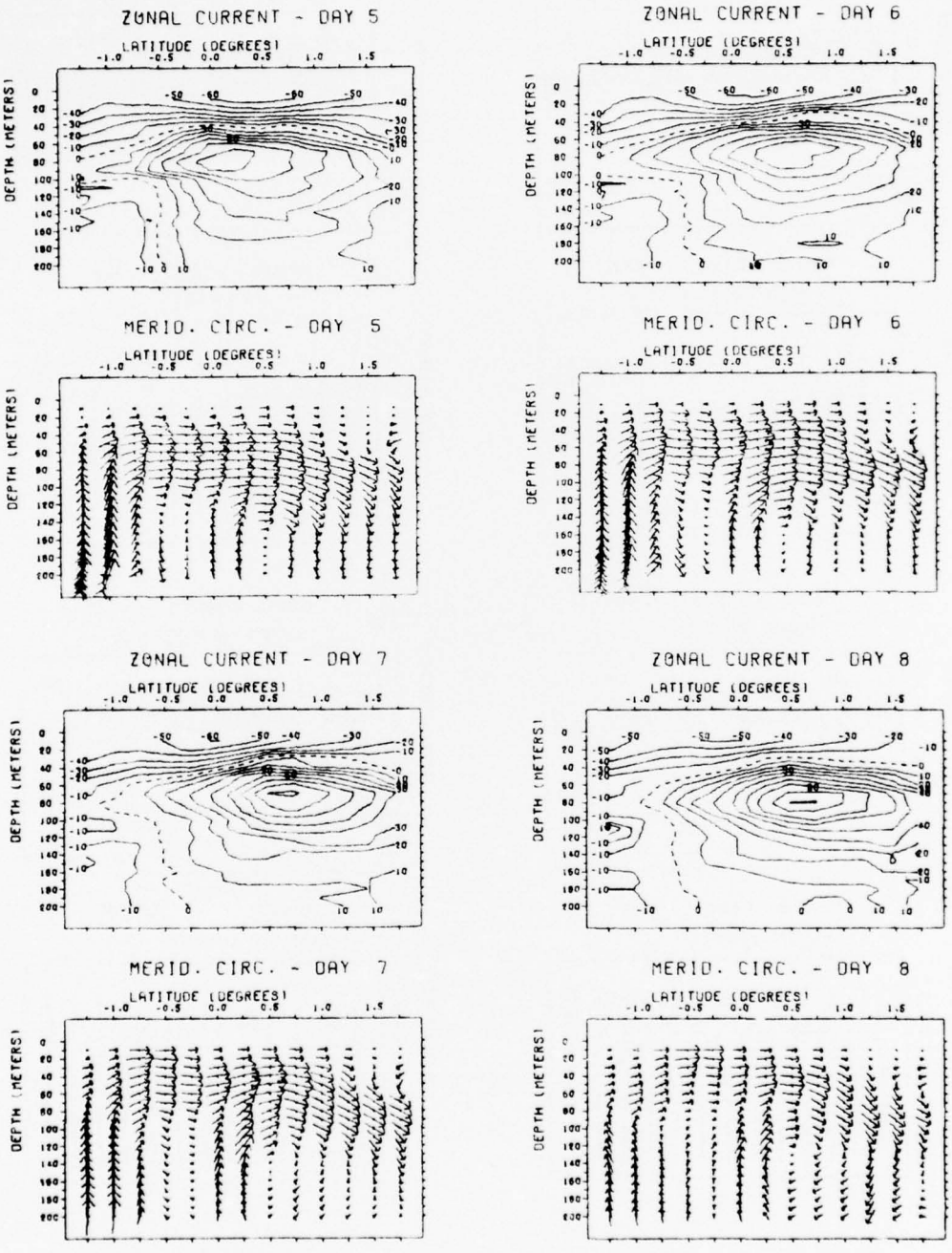
BEST AVAILABLE COPY

Figure 6



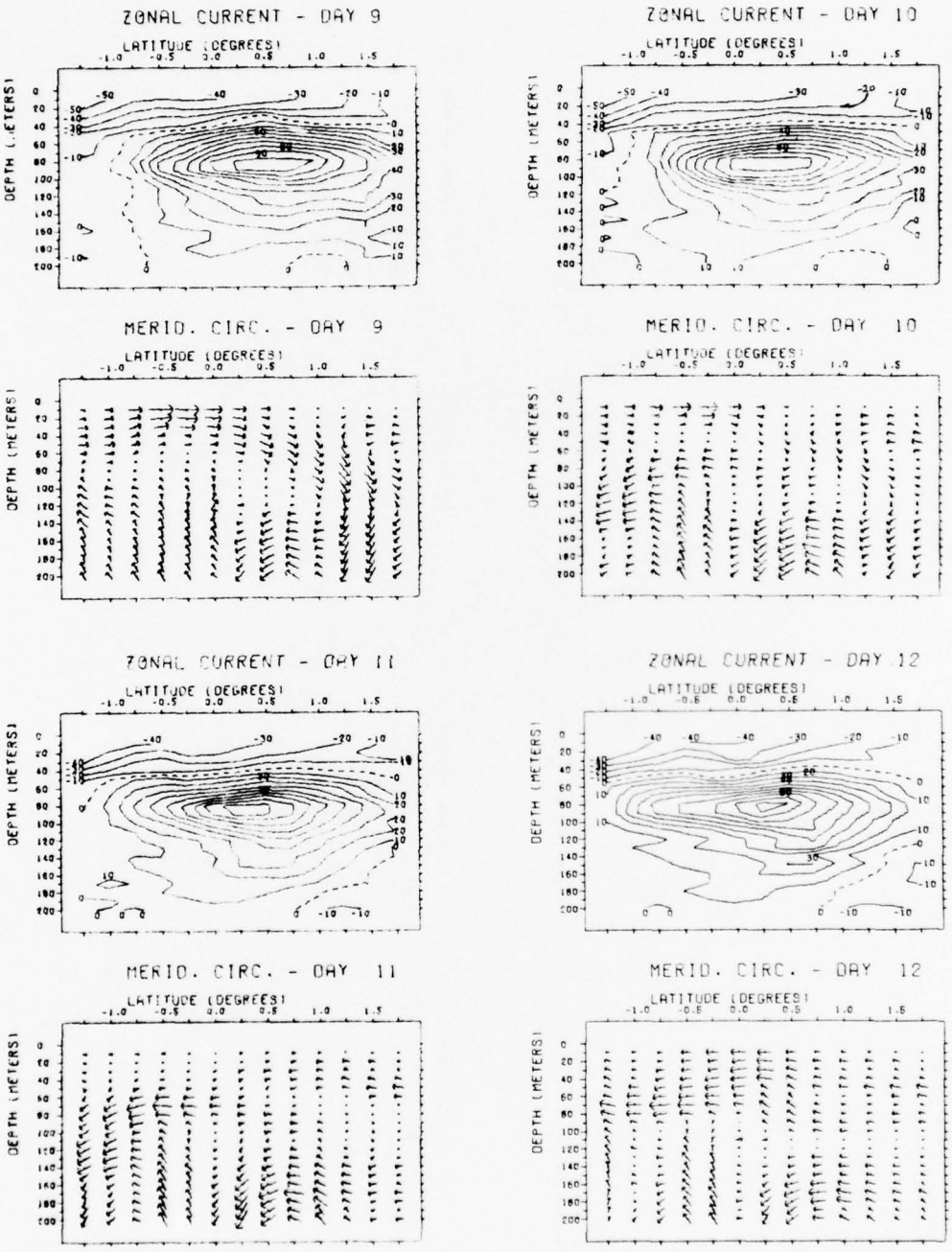
BEST AVAILABLE COPY

Figure 7



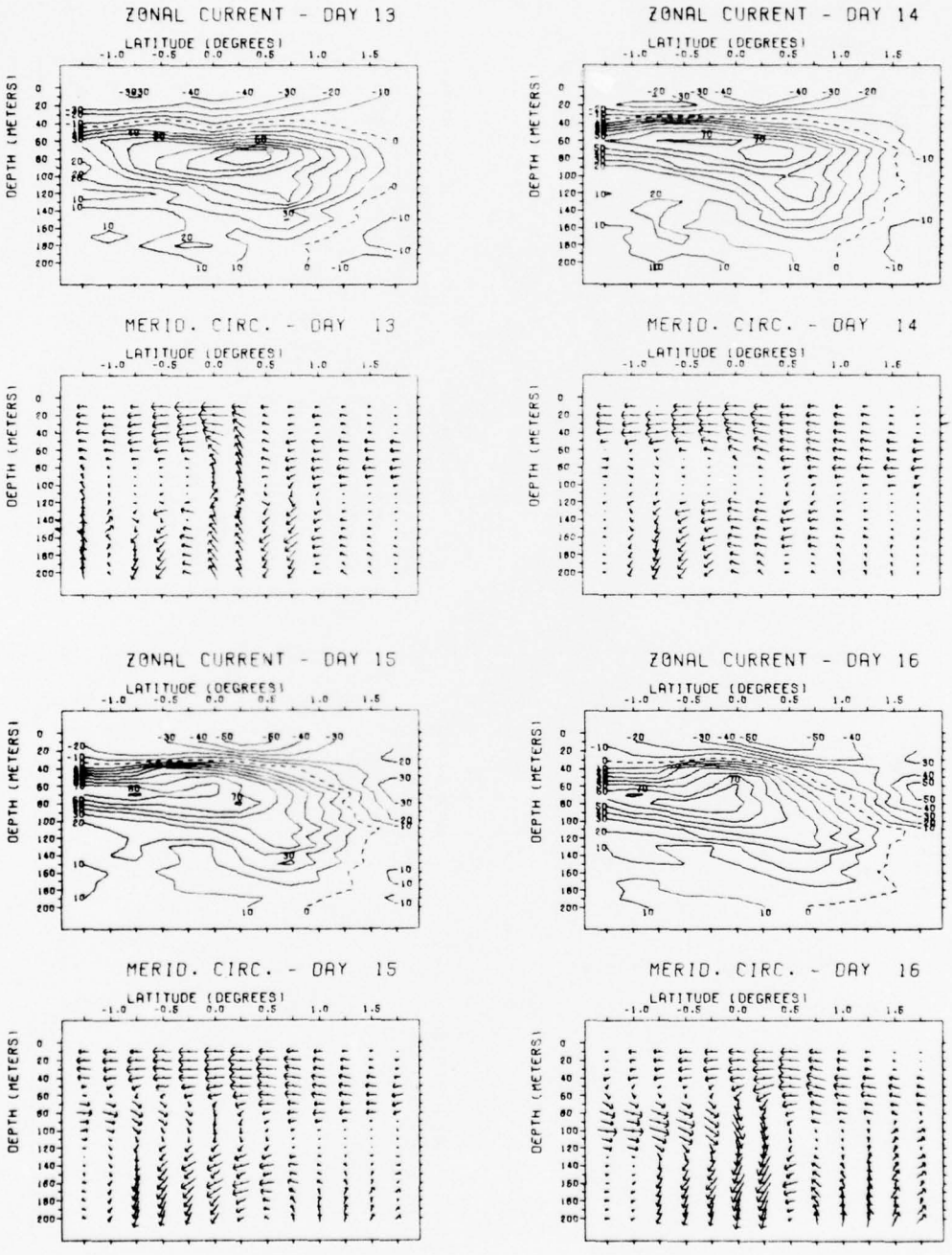
BEST AVAILABLE COPY

Figure 8



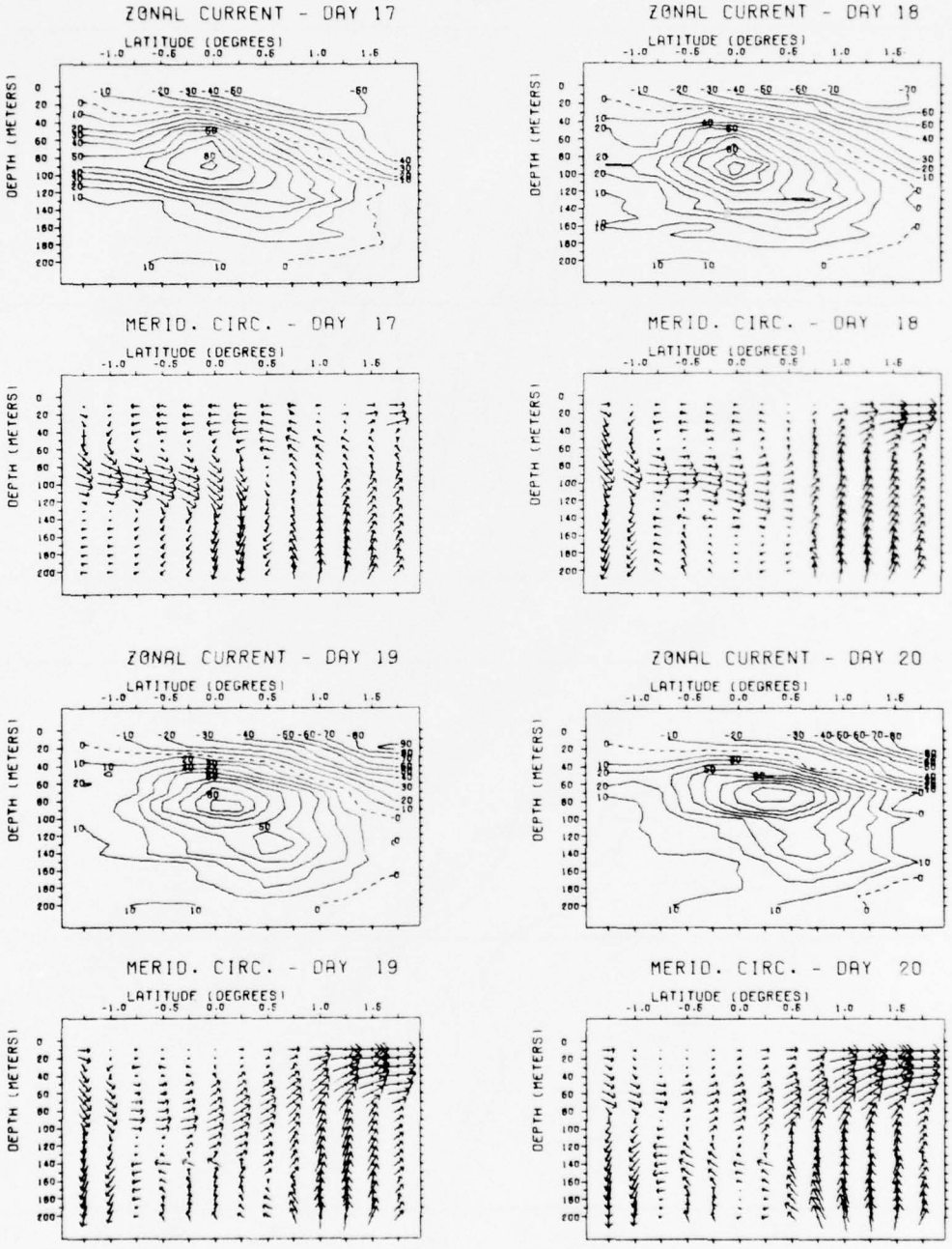
BEST AVAILABLE COPY

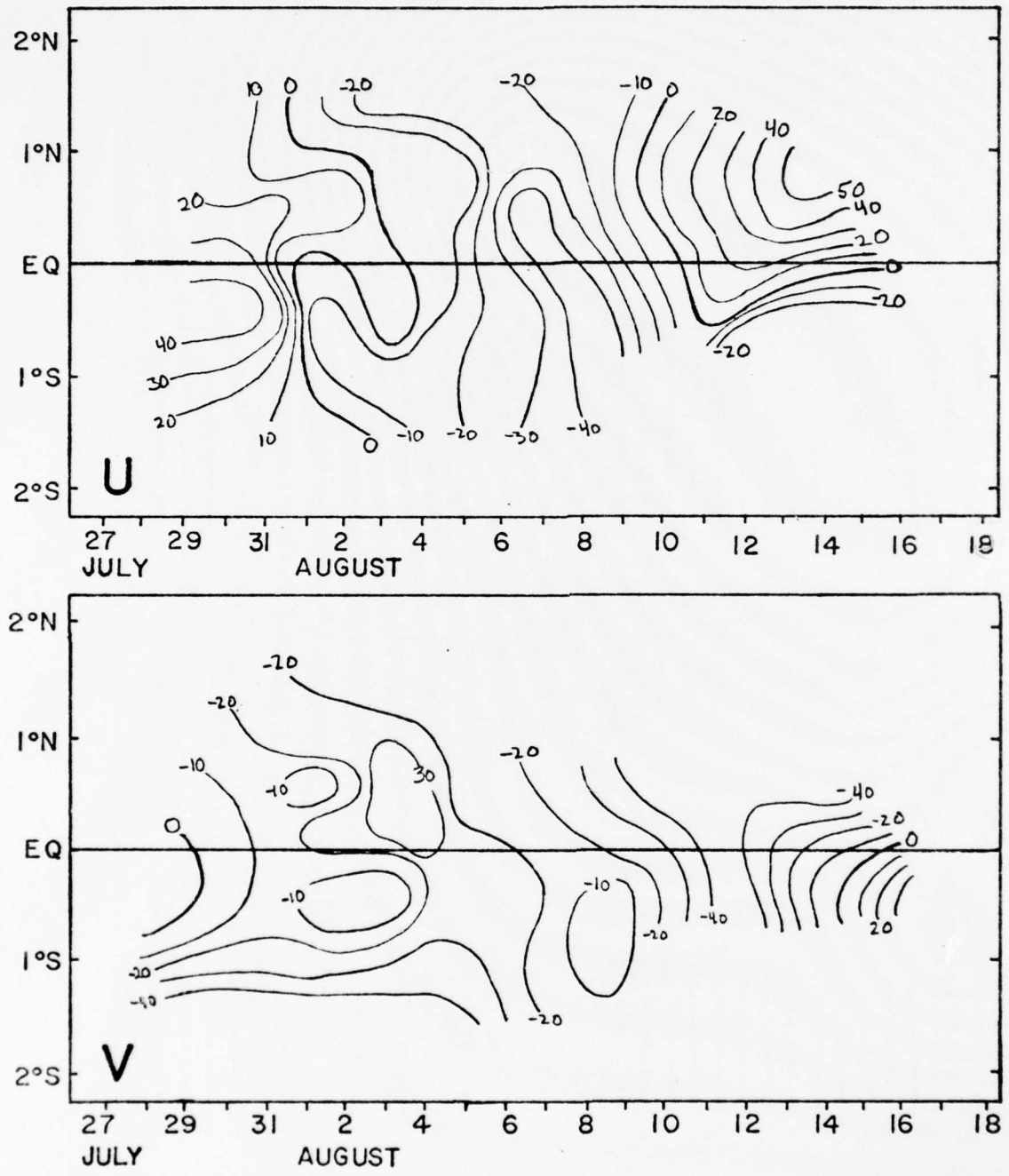
Figure 9



BEST AVAILABLE COPY

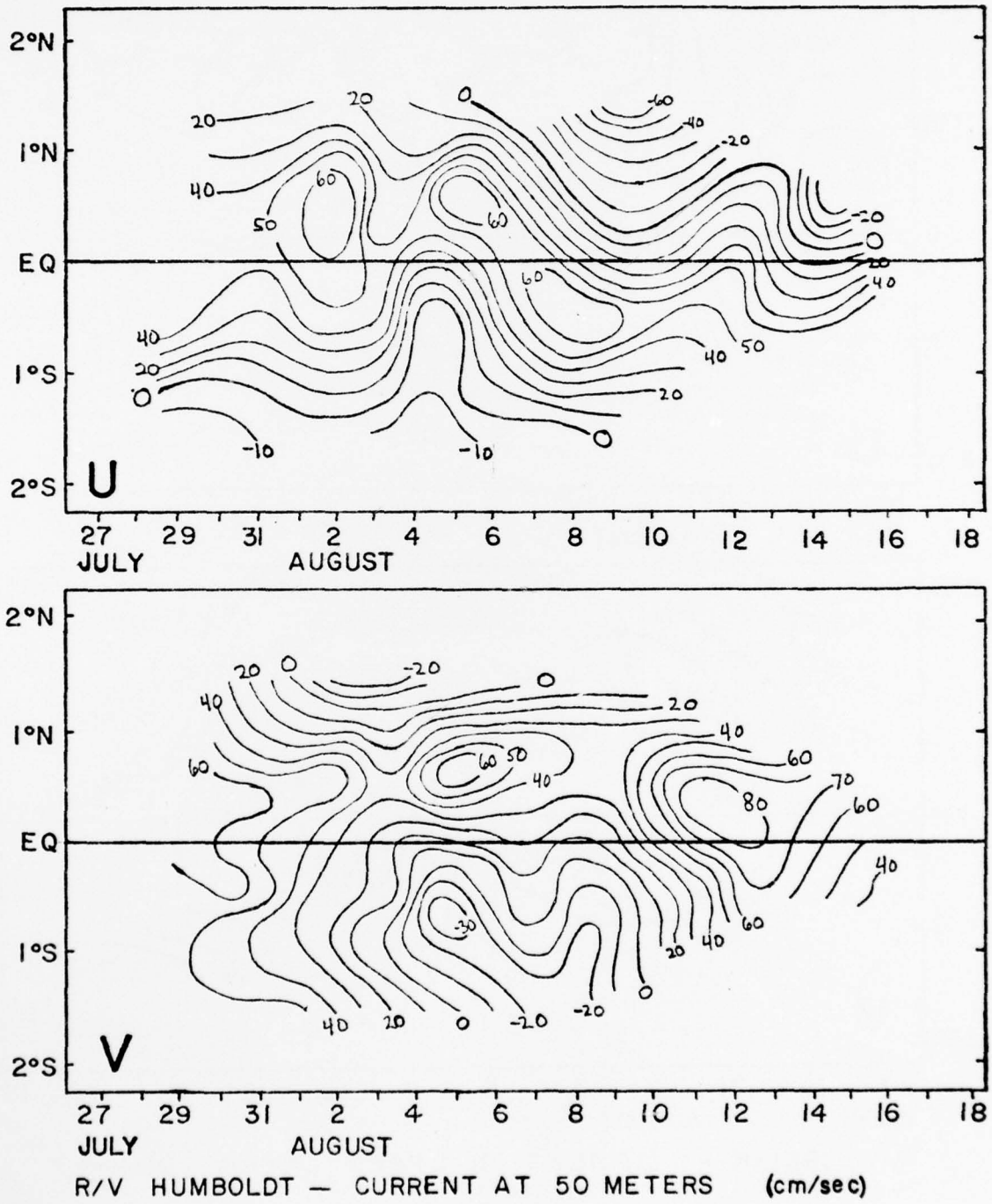
Figure 10





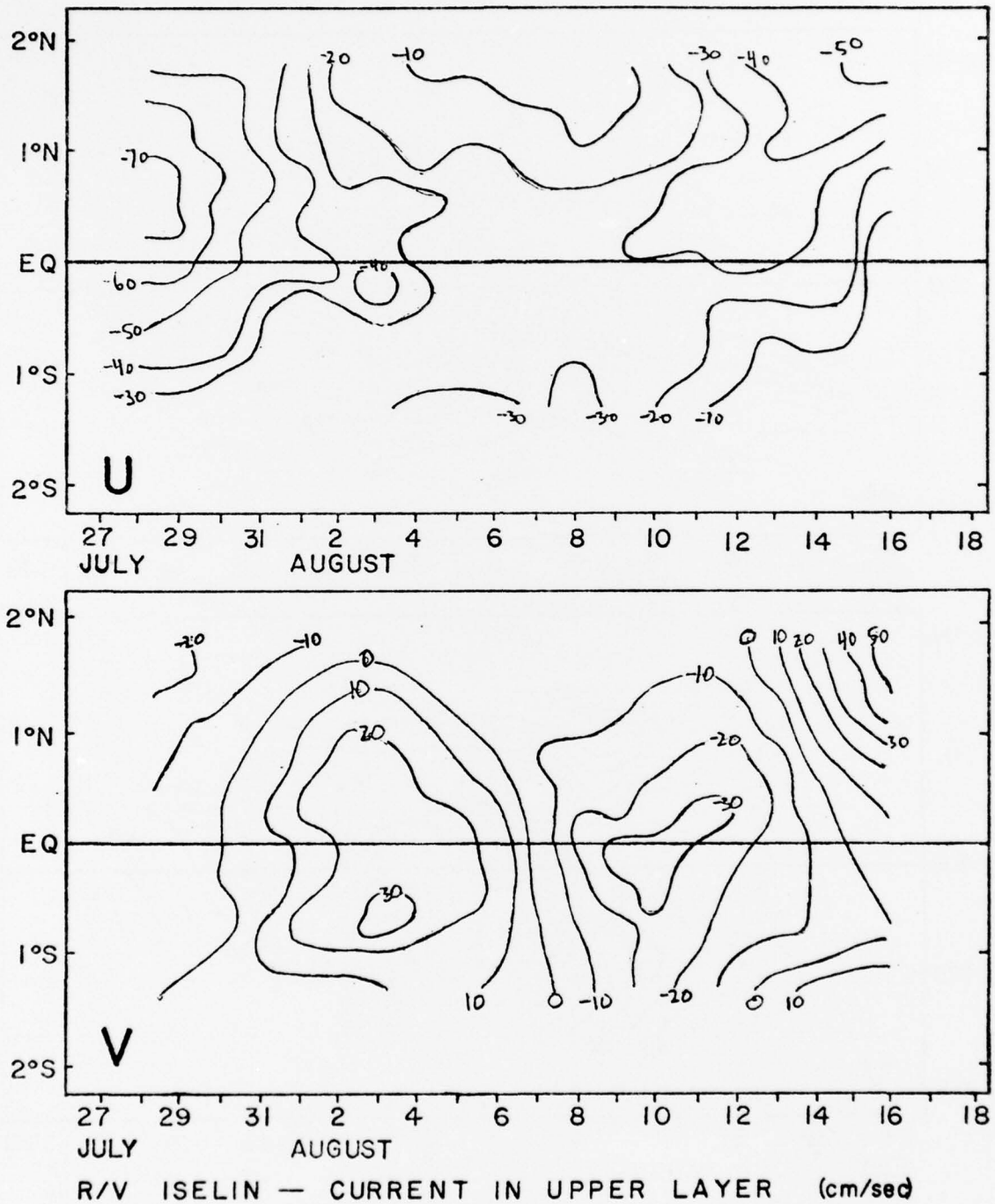
R/V HUMBOLDT — CURRENT AT 10 METERS (cm/sec)

Figure 11



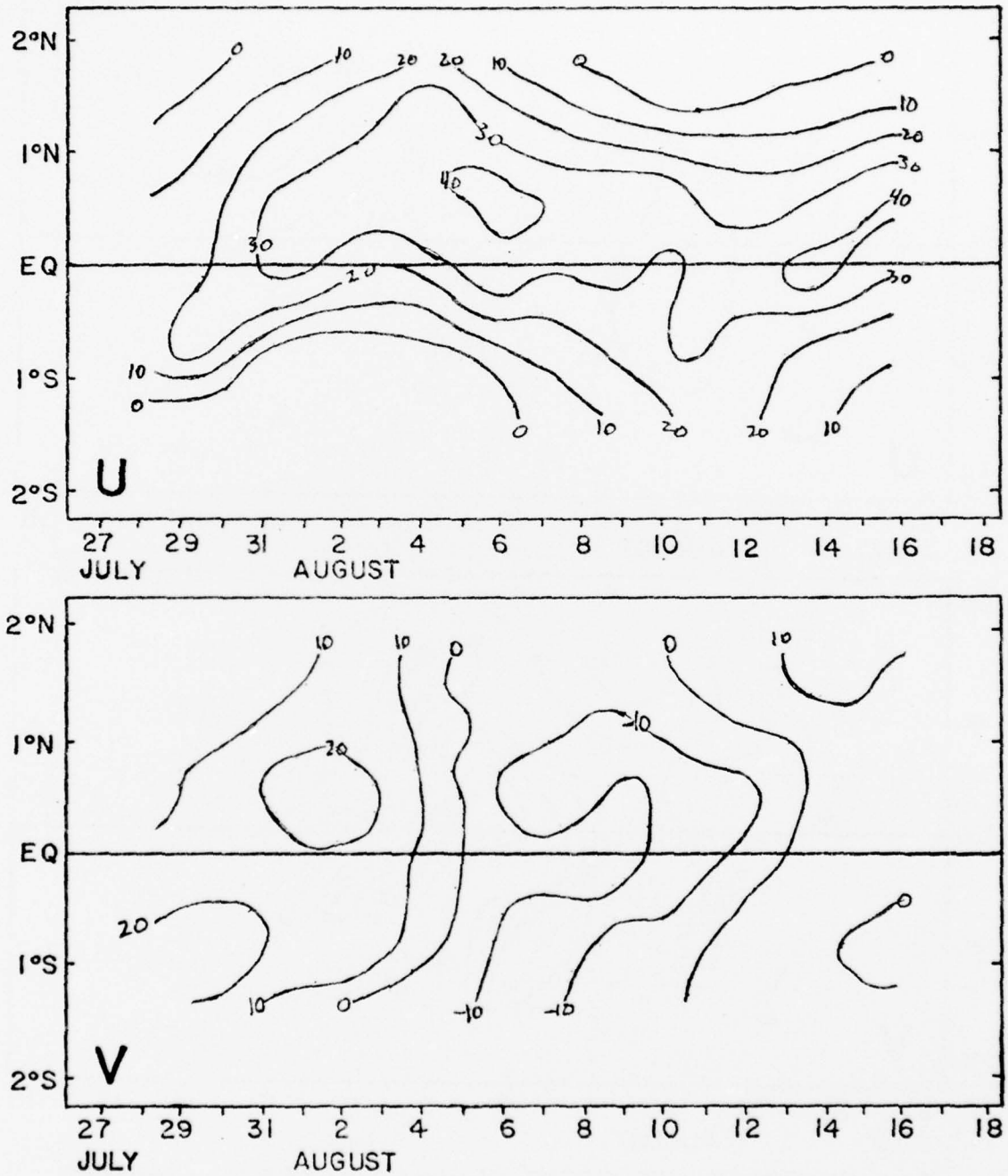
R/V HUMBOLDT — CURRENT AT 50 METERS (cm/sec)

Figure 12



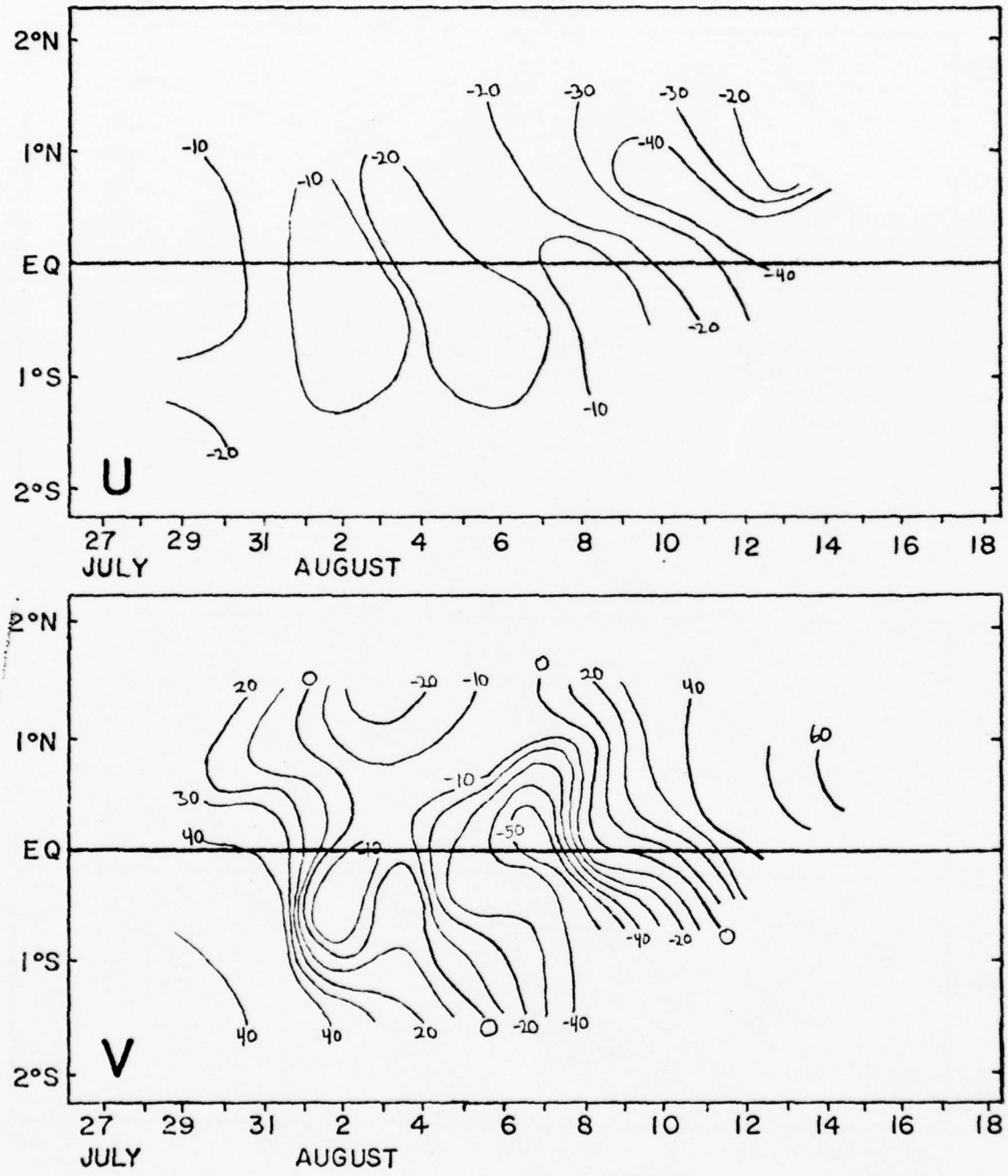
R/V ISELIN — CURRENT IN UPPER LAYER (cm/sec)

Figure 13



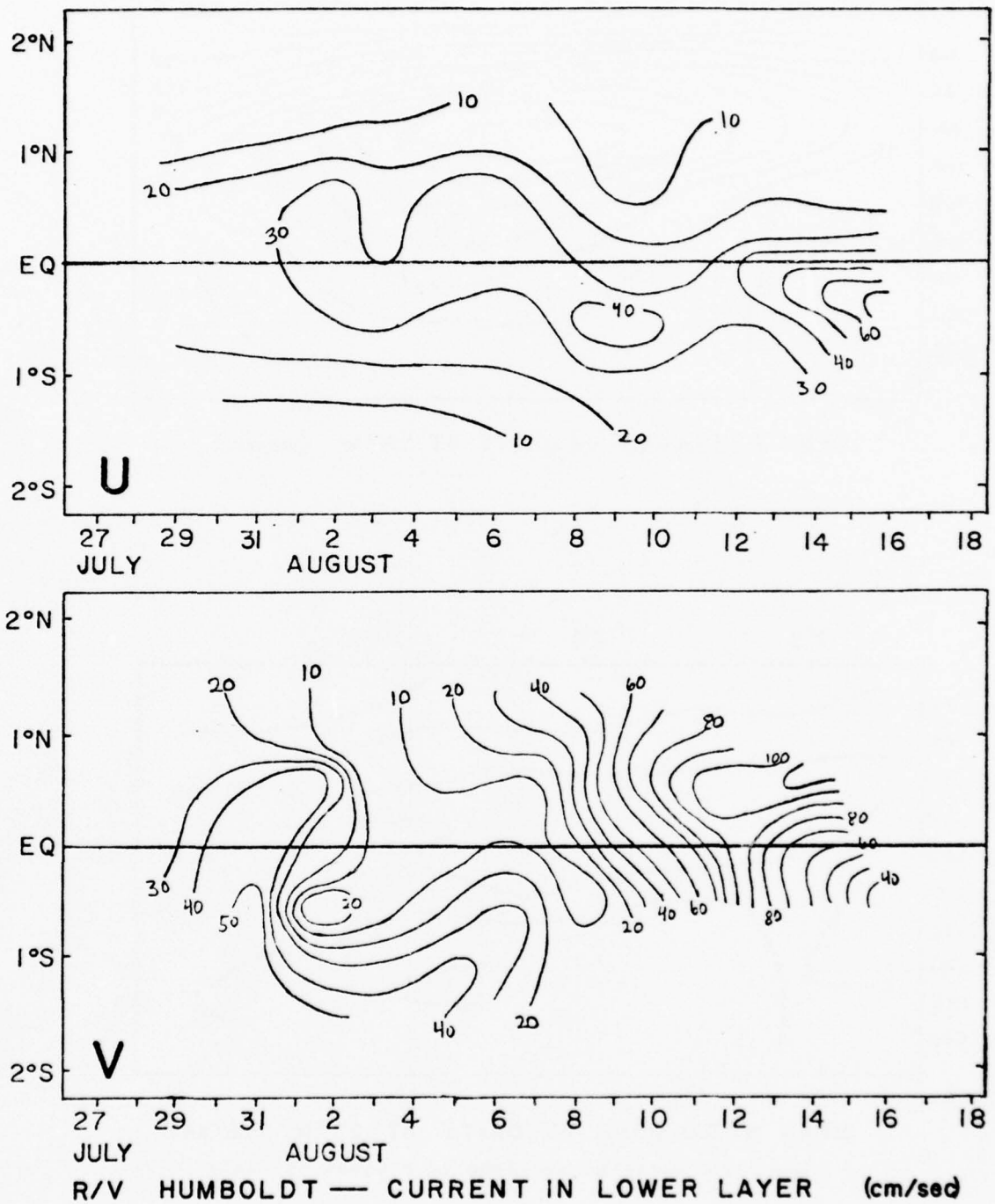
R/V ISELIN — CURRENT IN LOWER LAYER (cm/sec)

Figure 14



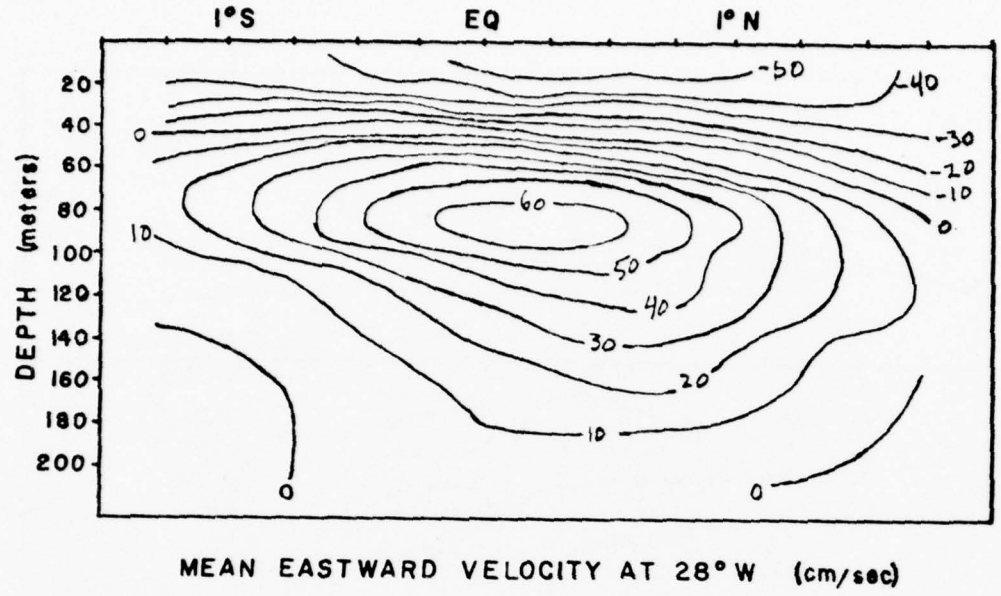
R/V HUMBOLDT — CURRENT IN UPPER LAYER (cm/sec)

Figure 15

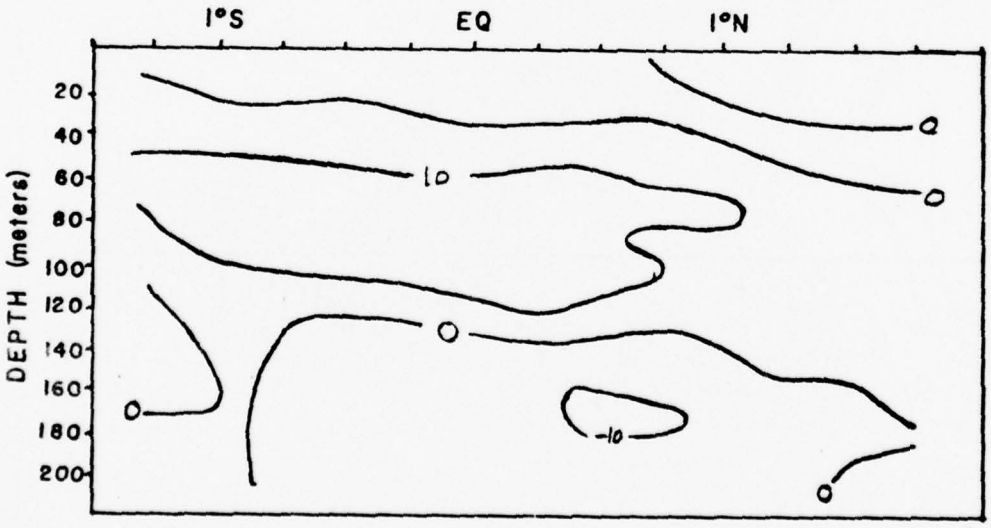


R/V HUMBOLDT — CURRENT IN LOWER LAYER (cm/sec)

Figure 16



MEAN EASTWARD VELOCITY AT 28°W (cm/sec)



MEAN NORTHWARD VELOCITY AT 28°W (cm/sec)

Figure 17: Vertical sections of average velocity

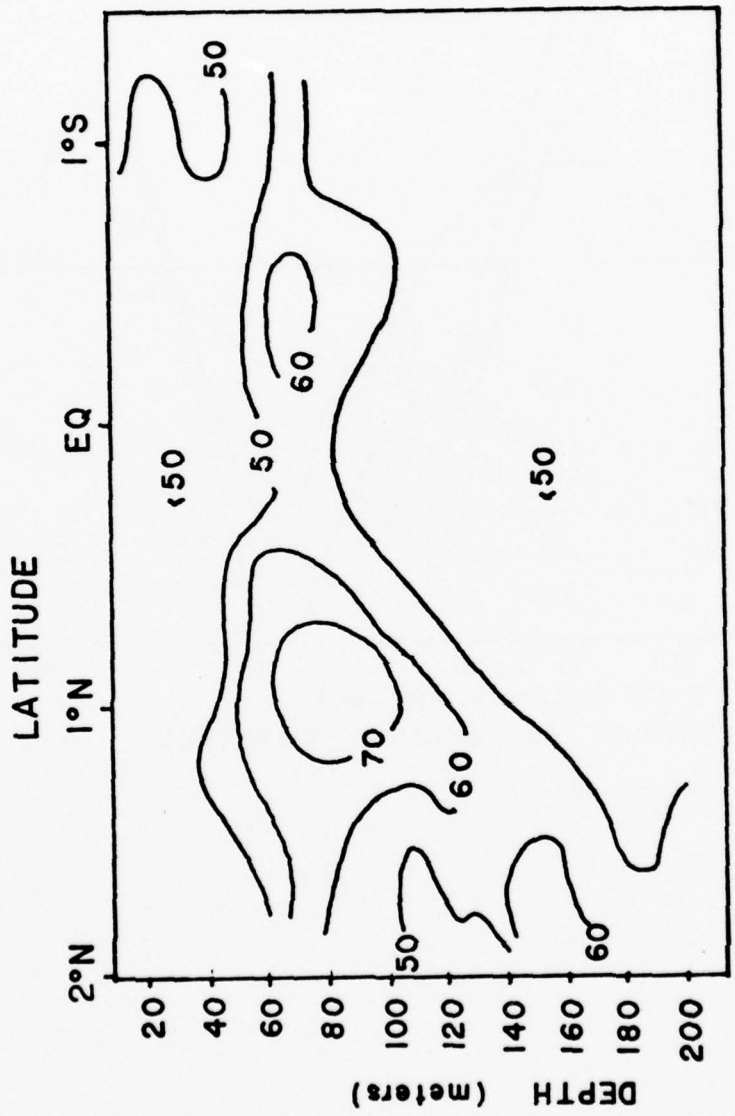
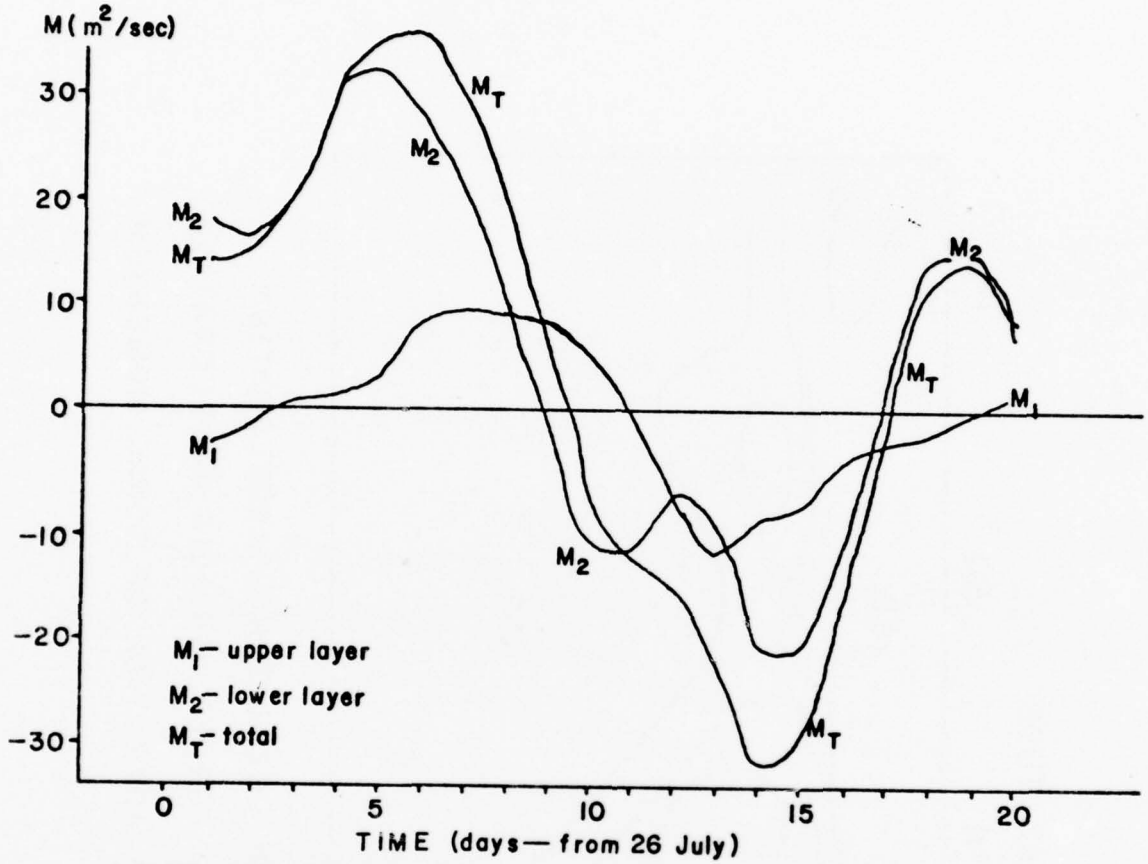


Figure 18 PERCENT OF LOCAL ZONAL ACCELERATION ACCOUNTED FOR BY CORIOLIS ACCELERATION MERIDIONAL ADVECTION OF ZONAL MOMENTUM



LAYER TRANSPORTS AT THE EQUATOR— OBSERVED

Figure 19

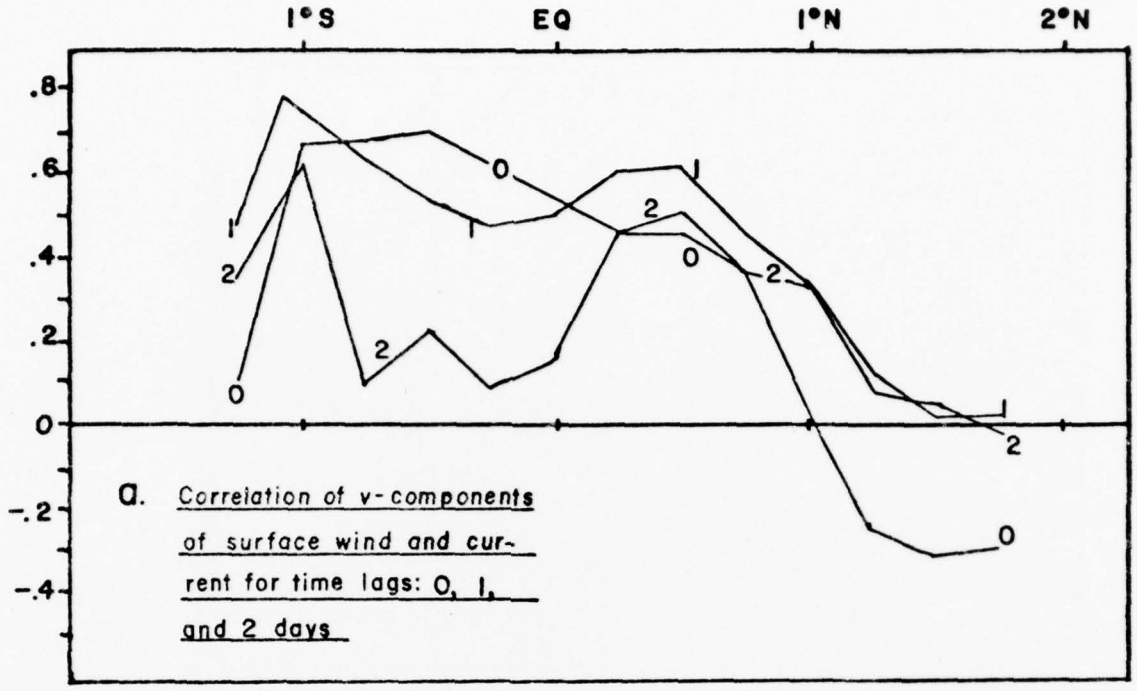
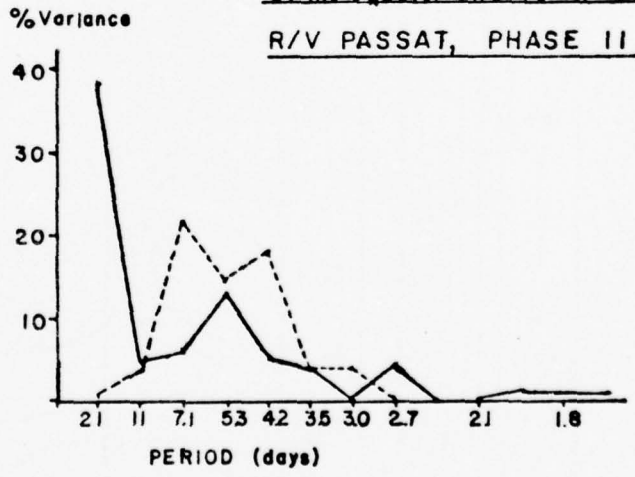

1°S
EQ
1°N
2°N
.8
.6
.4
.2
0
-.2
-.4
0
1
2
a. Correlation of v-components of surface wind and current for time lags: 0, 1, and 2 days

Figure 20


b. Periodogram of surface wind at the equator and 10°W R/V PASSAT, PHASE II
% Variance
40
30
20
10
21 11 7.1 5.3 4.2 3.5 3.0 2.7 2.1 1.8
PERIOD (days)

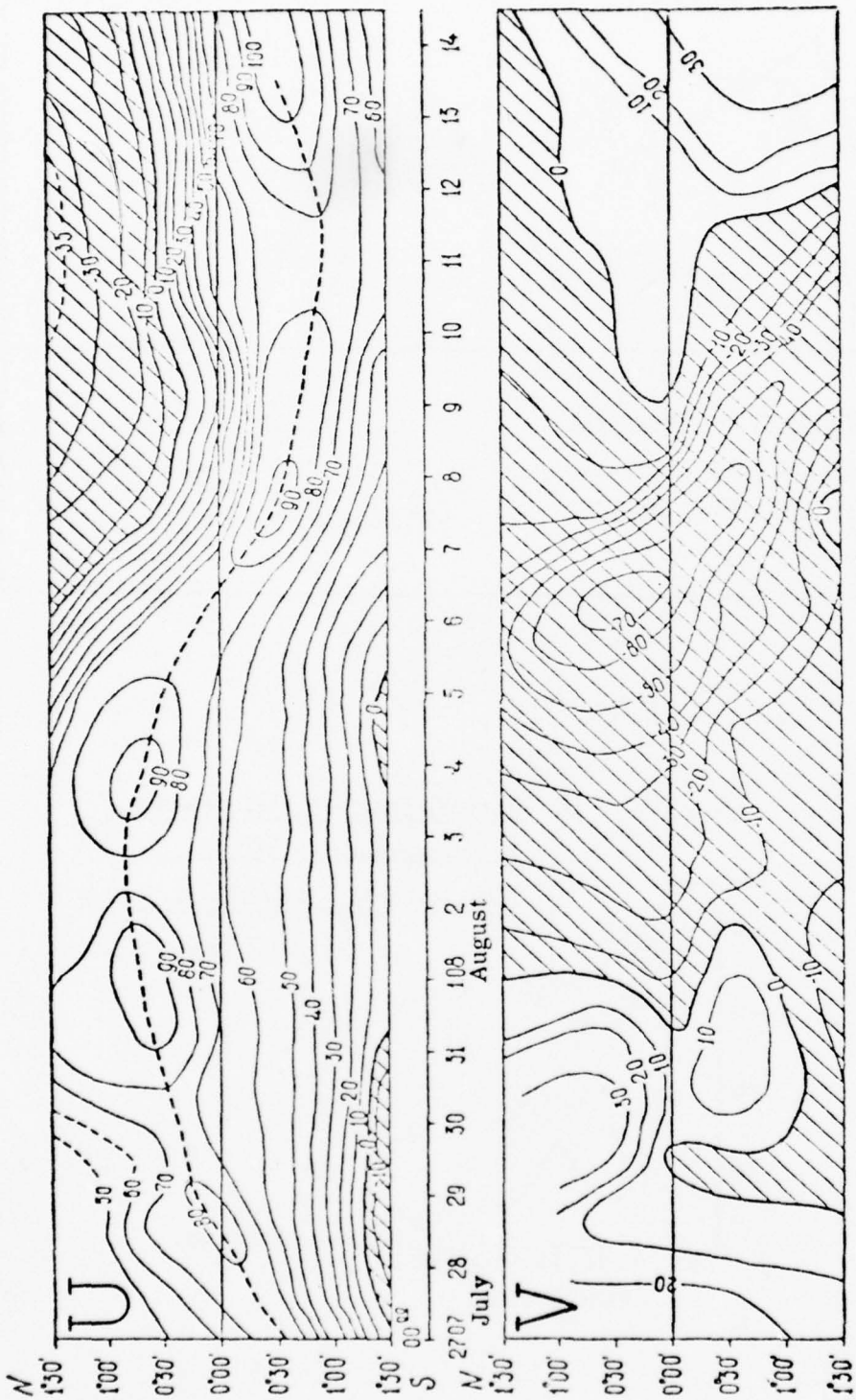


Figure 21: Current velocity at Undercurrent core at 23.5°W as observed from R/V Kurchatov

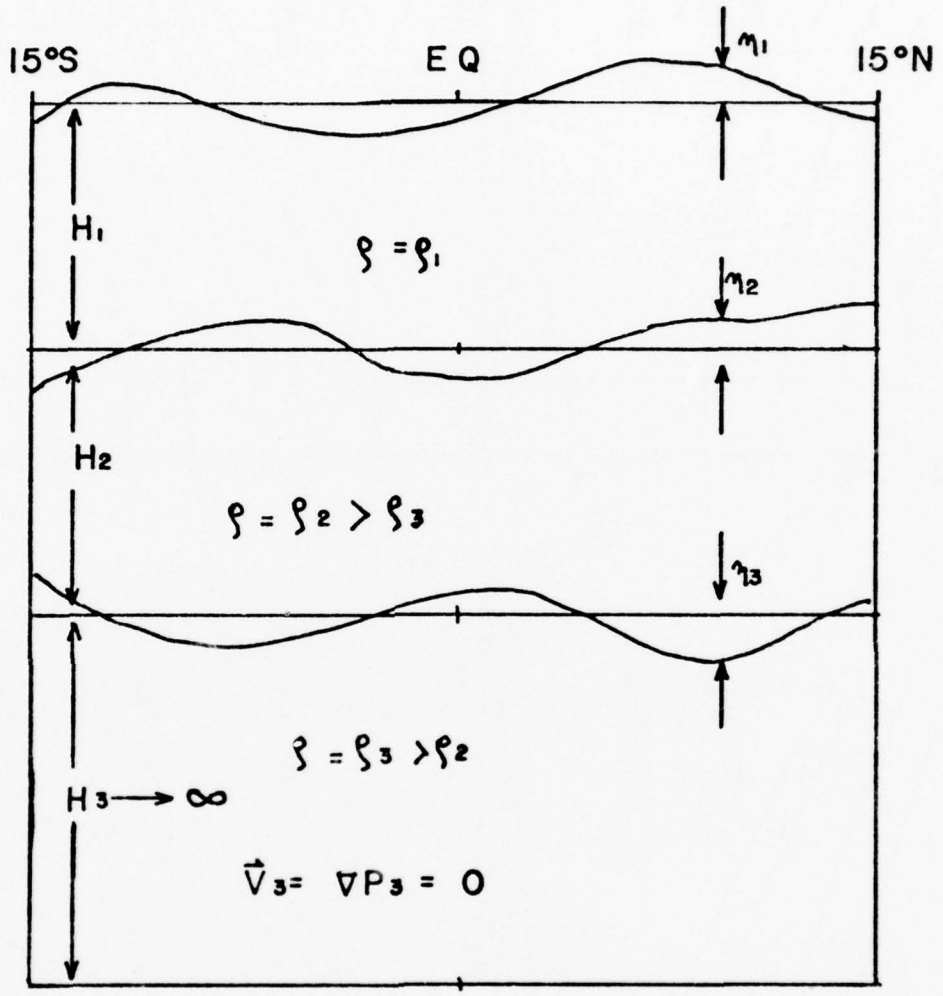
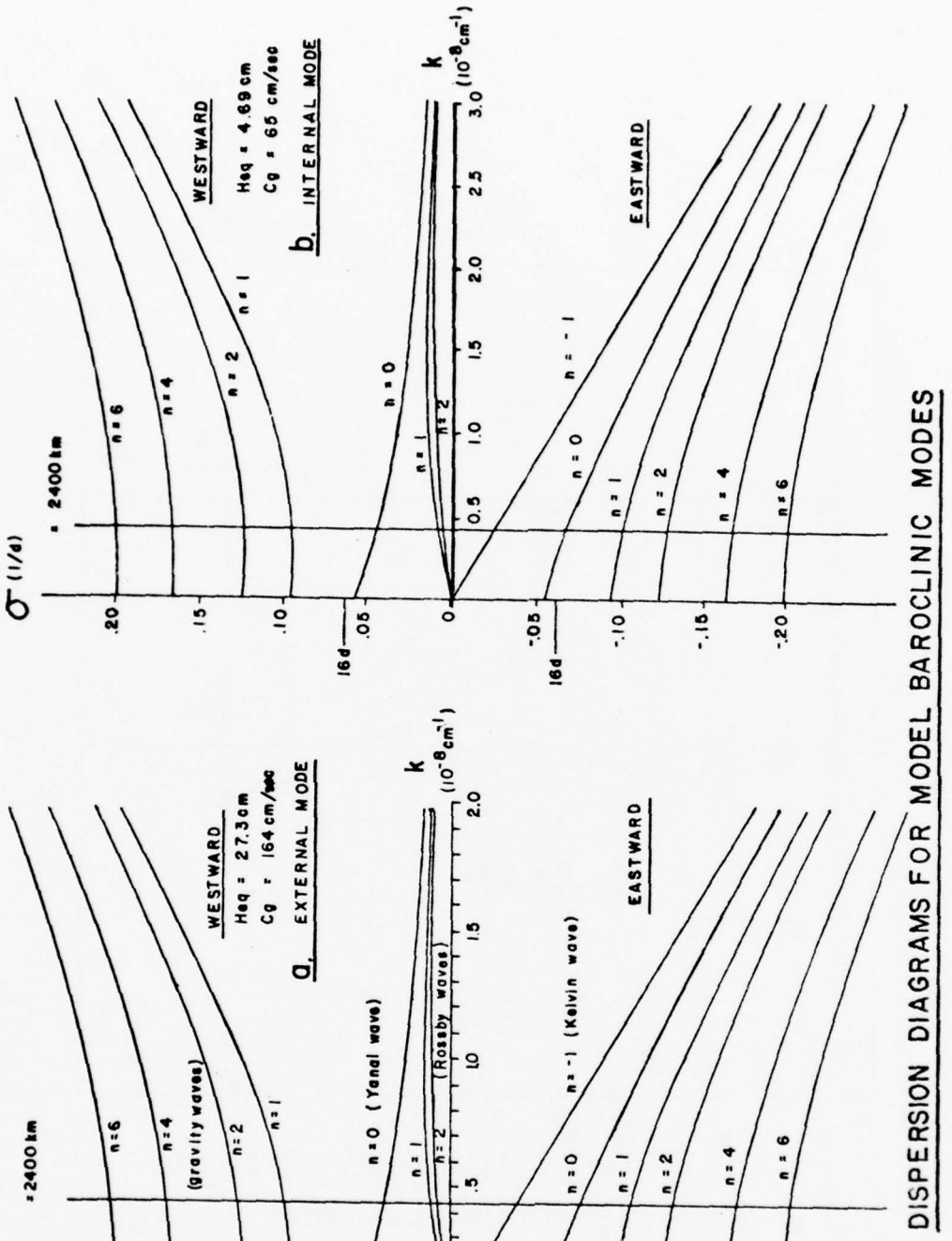


DIAGRAM OF SYSTEM USED TO STUDY WIND-FORCED OSCILLATIONS

Figure 22



DISPERSION DIAGRAMS FOR MODEL BAROCLINIC MODES

Figure 23

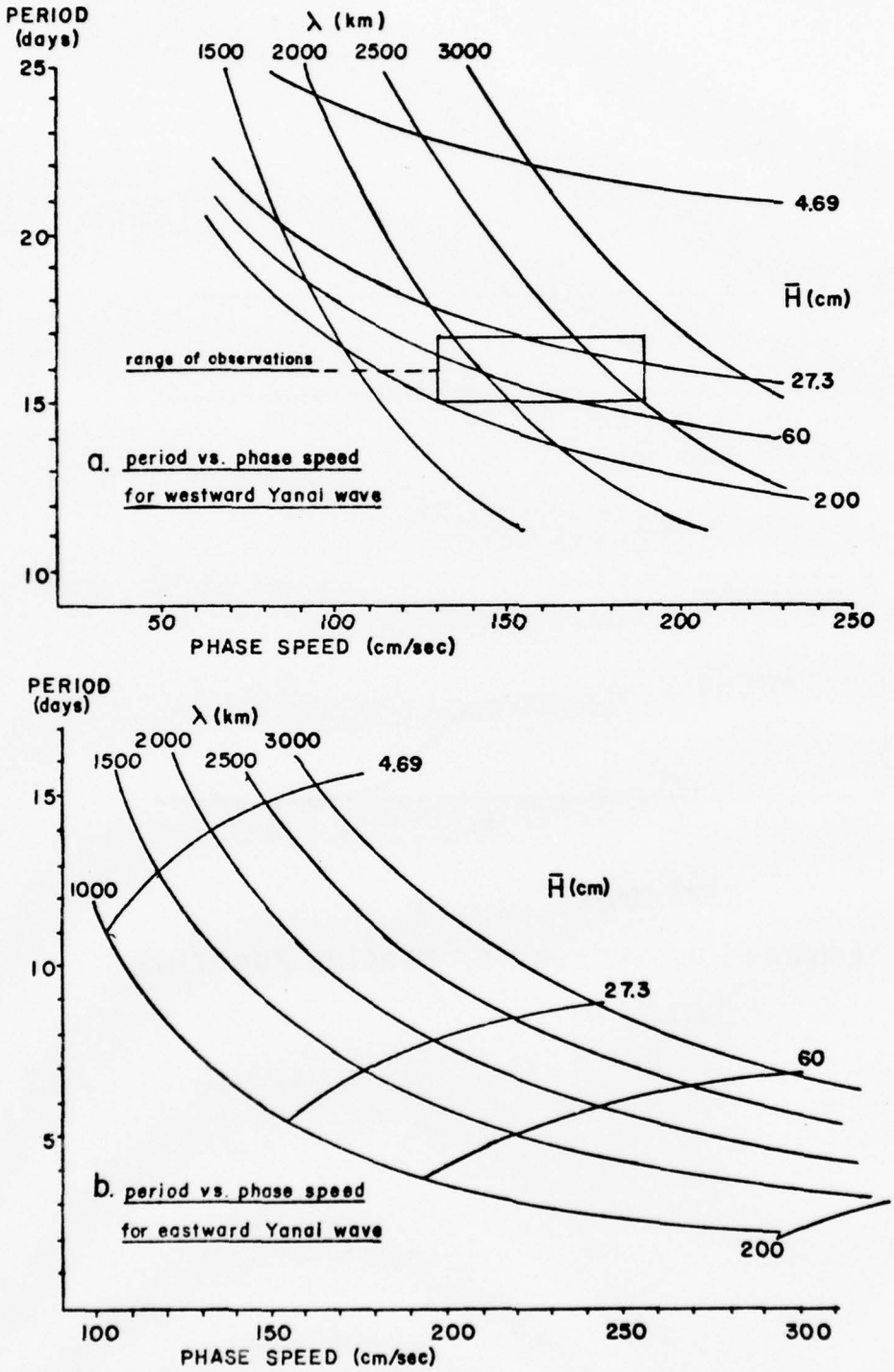
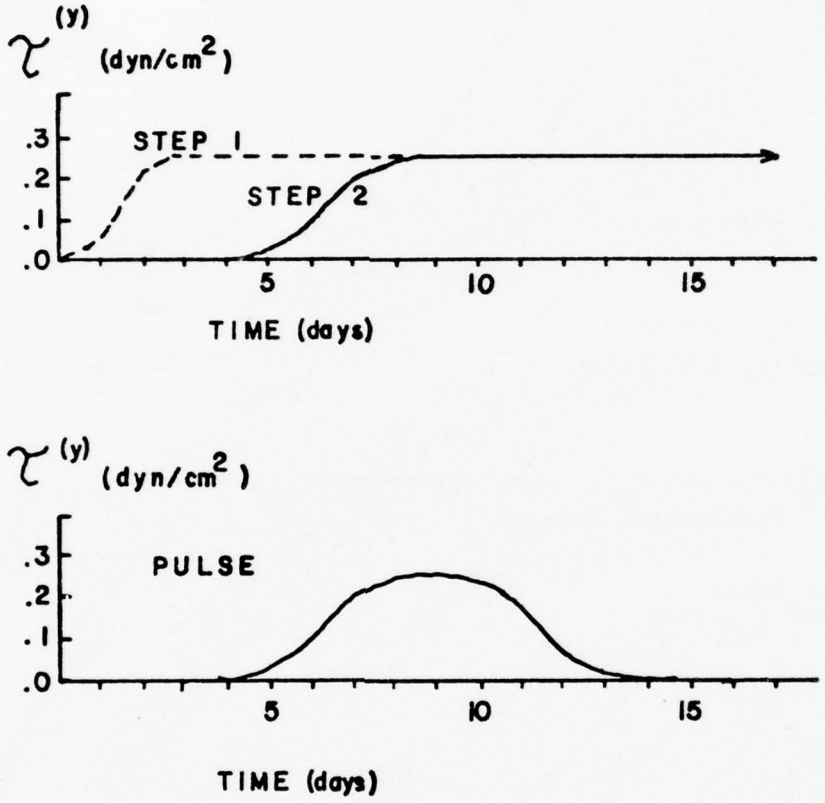

PERIOD
(days)
λ (km)
1500
2000
2500
3000
25
20
15
10
4.69
H̄ (cm)
27.3
60
200
range of observations
a. period vs. phase speed
for westward Yanai wave
50
100
150
200
250
PHASE SPEED (cm/sec)
PERIOD
(days)
λ (km)
2000
3000
1500
2500
4.69
15
1000
H̄ (cm)
10
27.3
60
5
b. period vs. phase speed
for eastward Yanai wave
200
100
150
200
250
300
PHASE SPEED (cm/sec)

Figure 24



TEMPORAL DEPENDENCE OF FORCING FUNCTION

Figure 25

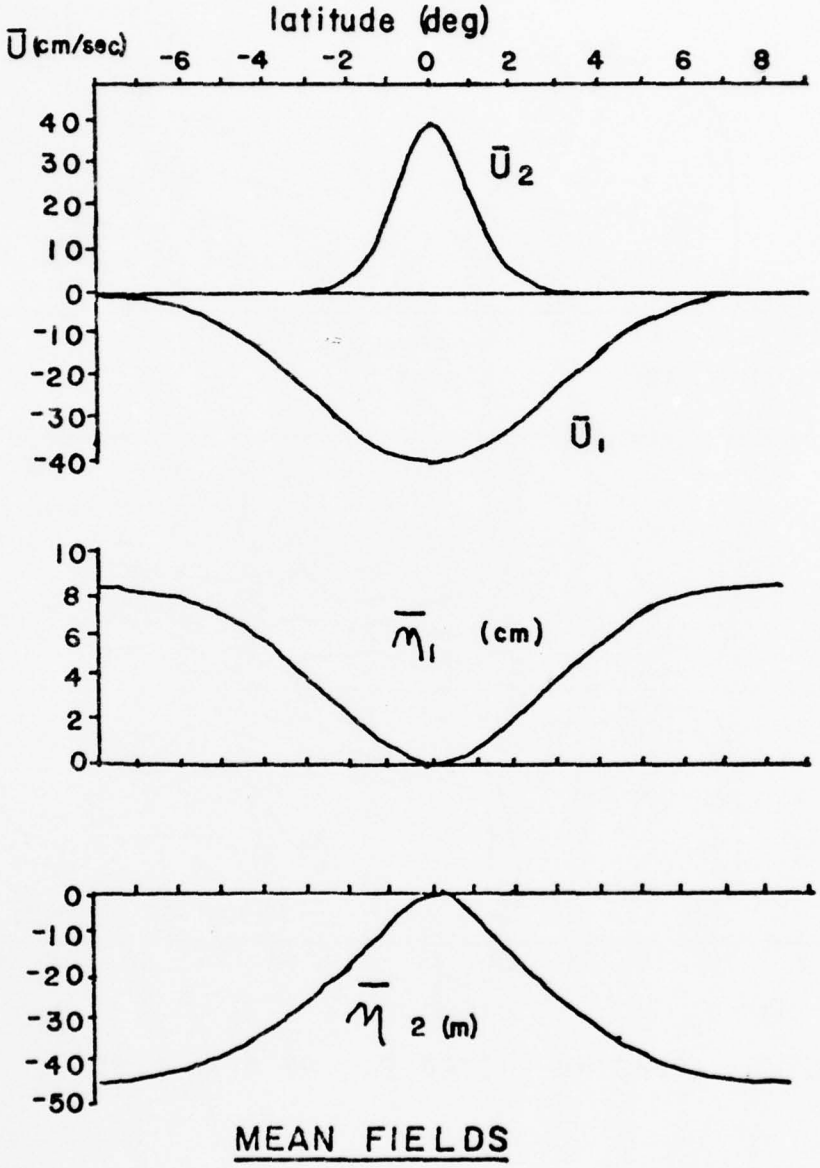
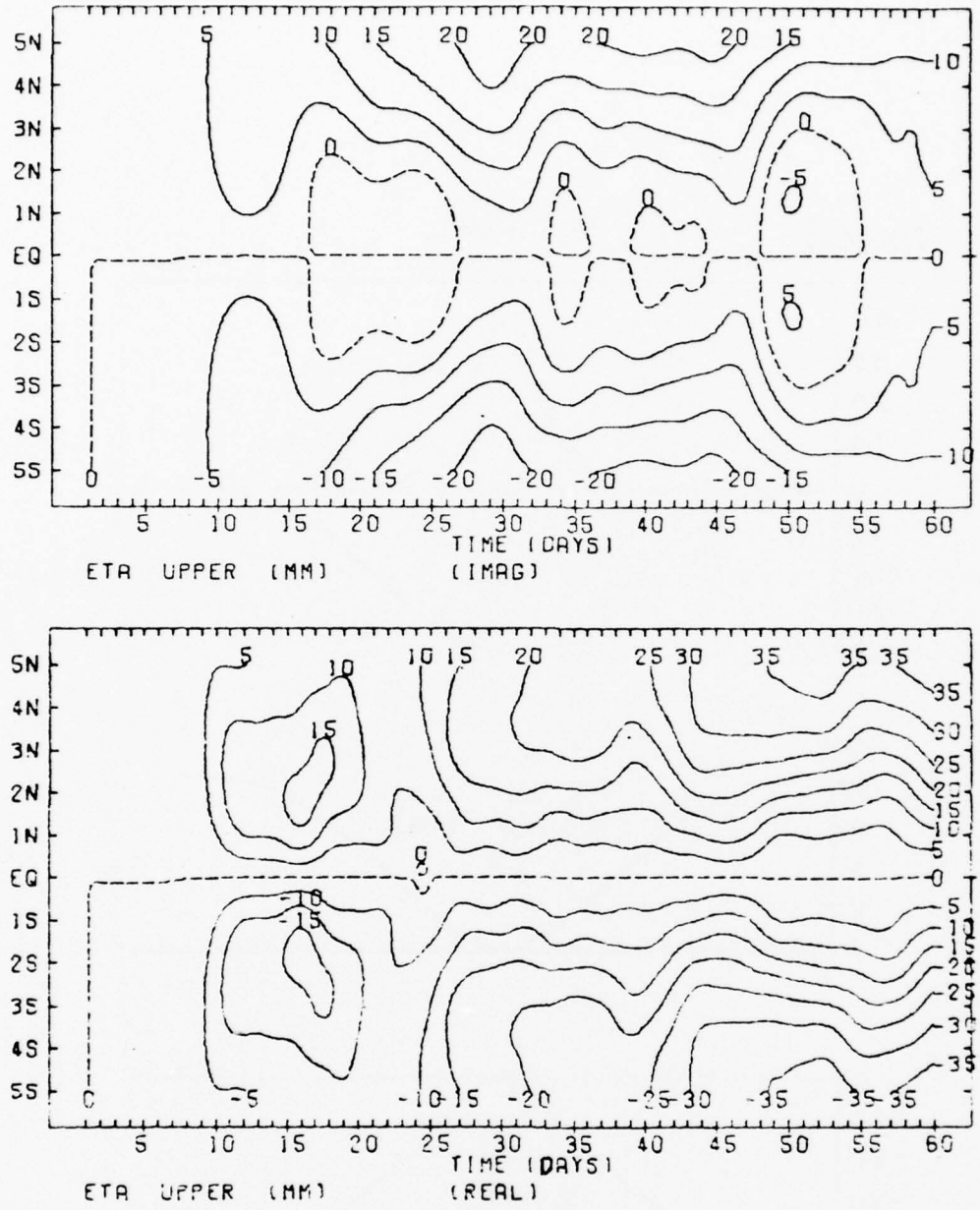
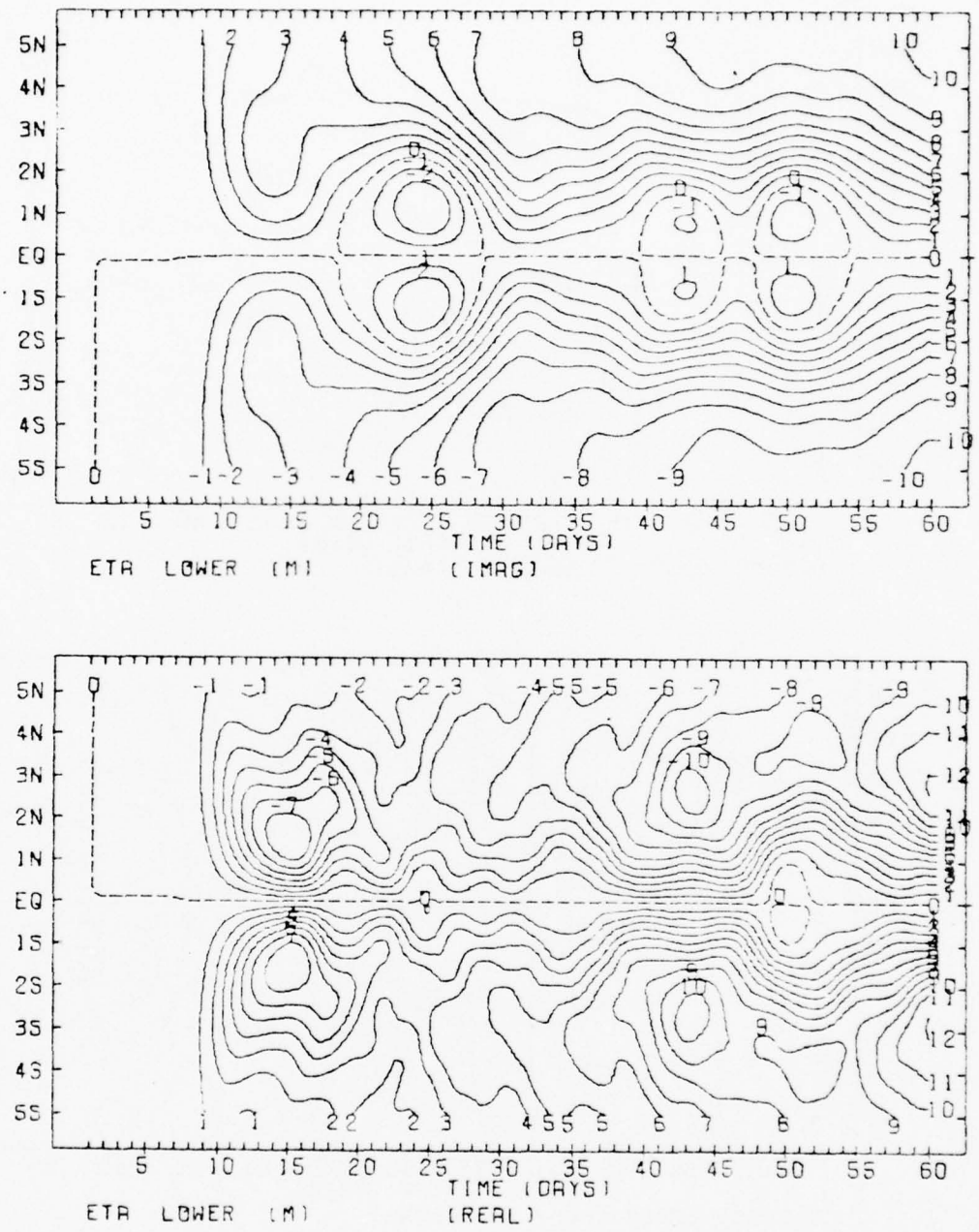

latitude (deg)
$\bar{U}$ (cm/sec)
-6
-4
-2
0
2
4
6
8
40
30
20
10
0
-10
-20
-30
-40
$\bar{U}_2$
$\bar{U}_1$
10
8
6
4
2
0
$\bar{\eta}_1$ (cm)
0
-10
-20
-30
-40
-50
$\bar{\eta}_2$ (m)
MEAN FIELDS

Figure 26



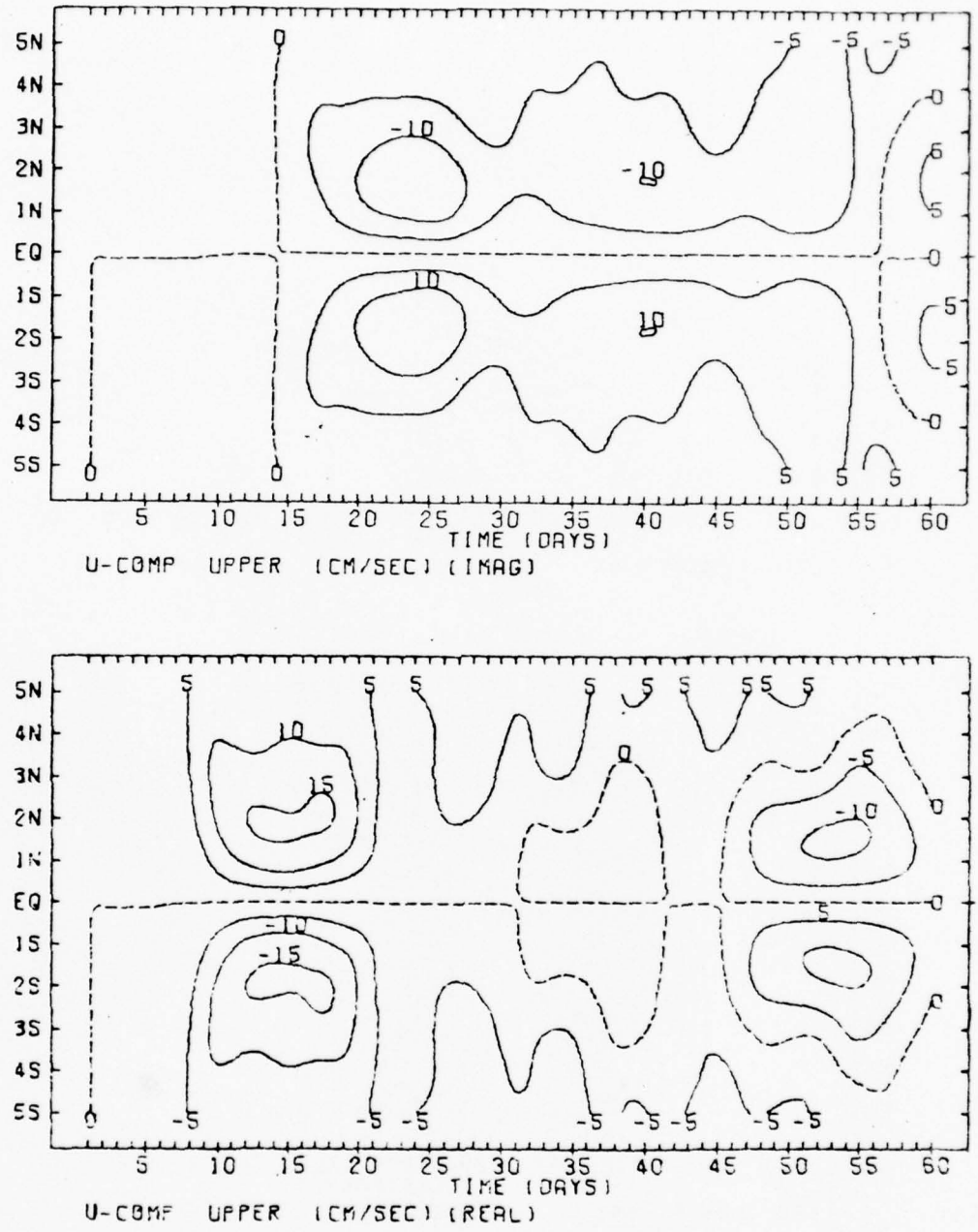
CASE 3: FORCING = STEP 2, NO MEAN FLOW

Figure 27



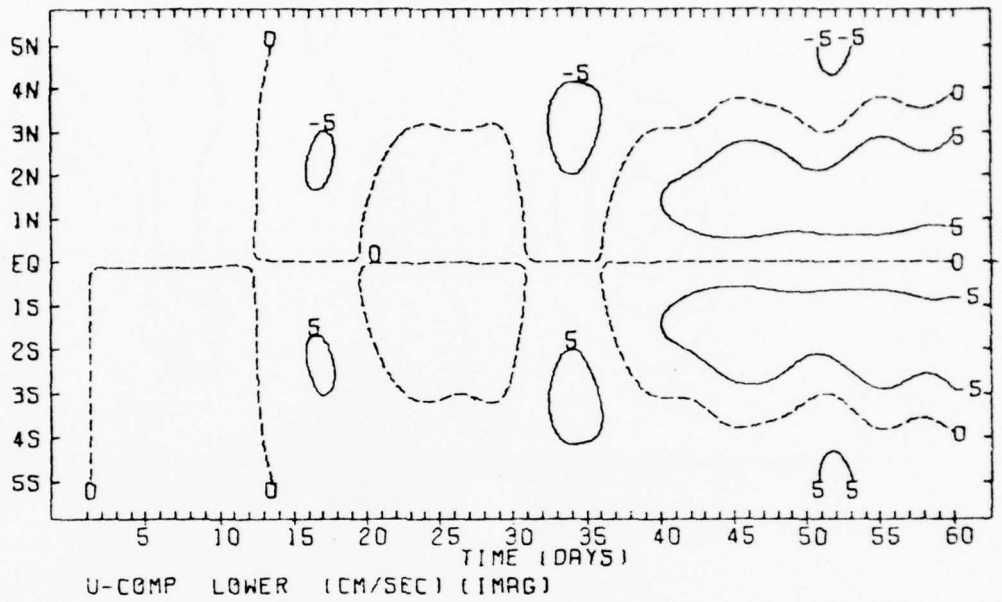
CASE 3: FORCING = STEP 2. NO MEAN FLOW

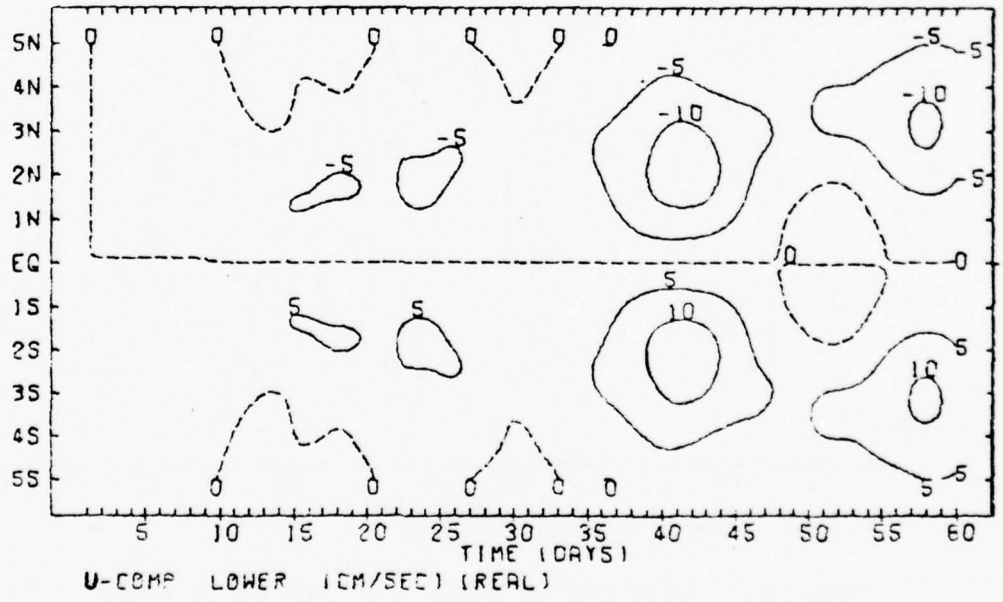
Figure 28



CASE 3: FORCING = STEP 2. NO MEAN FLOW

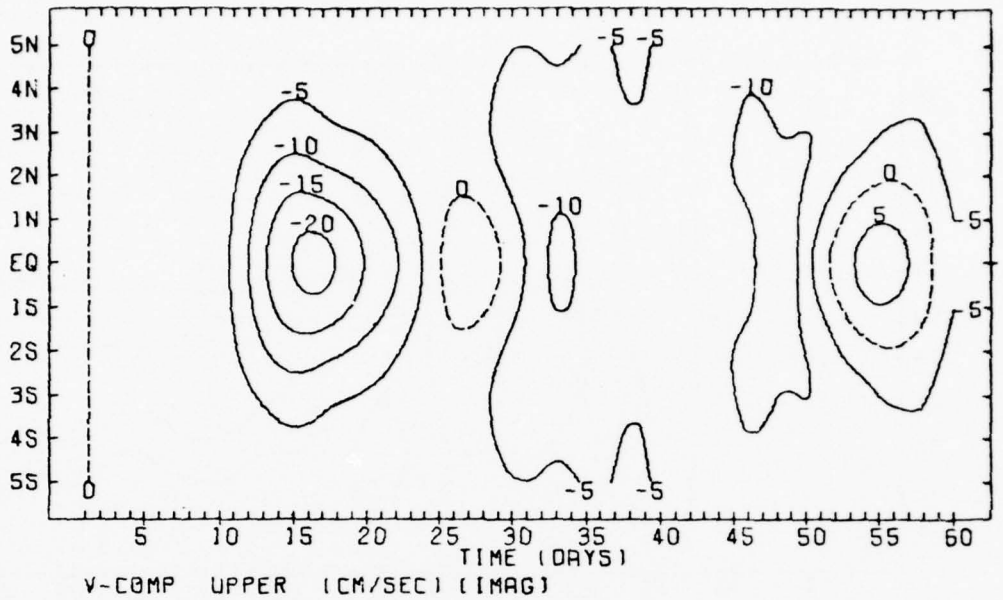
Figure 29

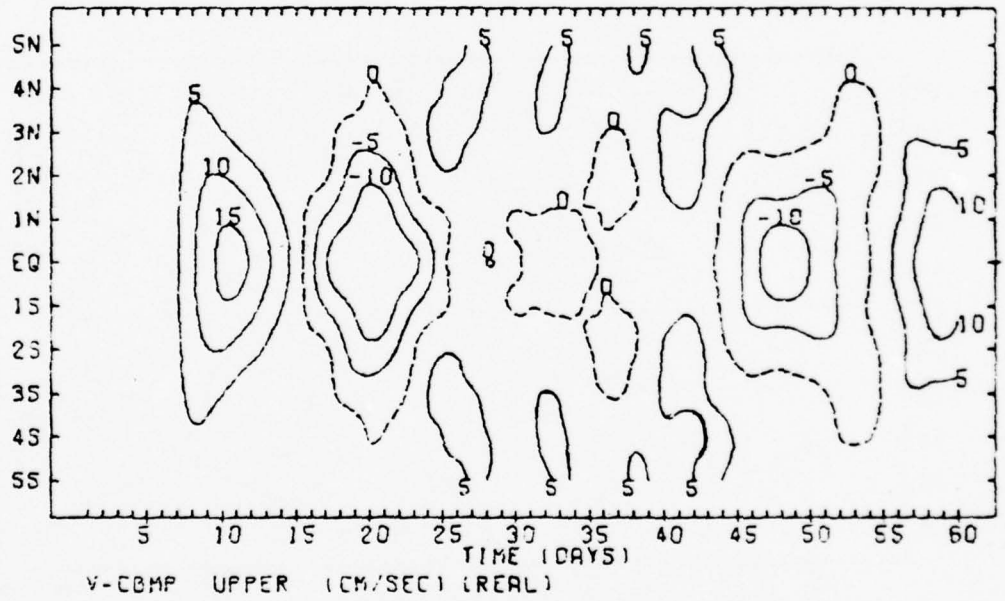




CASE 3: FORCING = STEP 2. NO MEAN FLOW

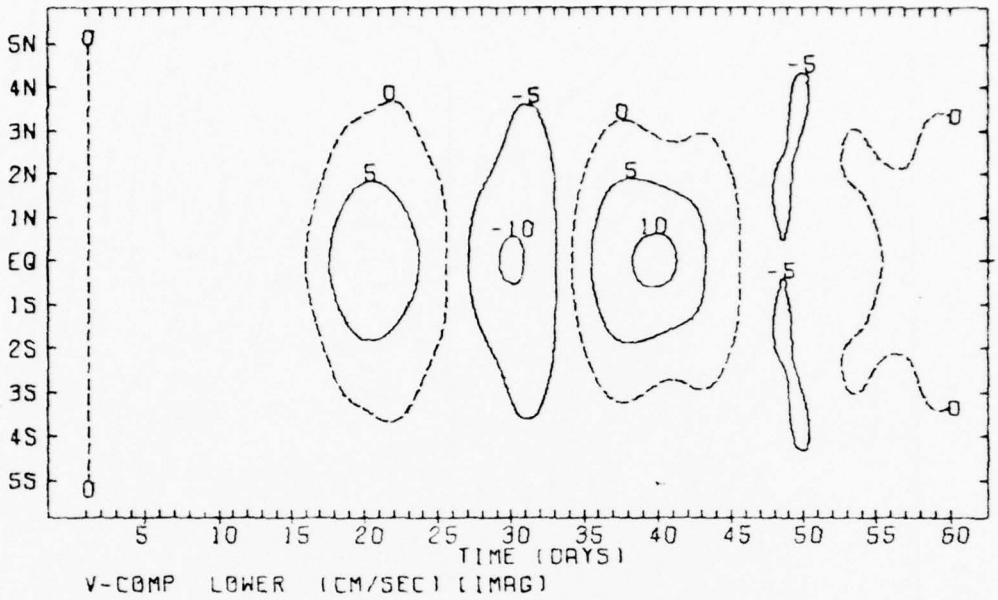
Figure 30

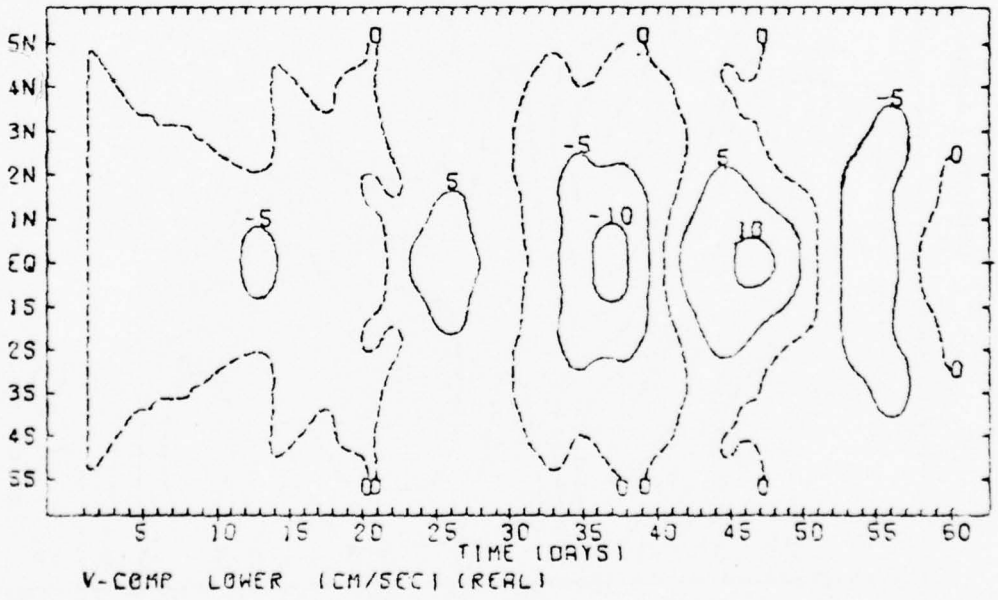




CASE 3: FORCING = STEP 2. NO MEAN FLOW

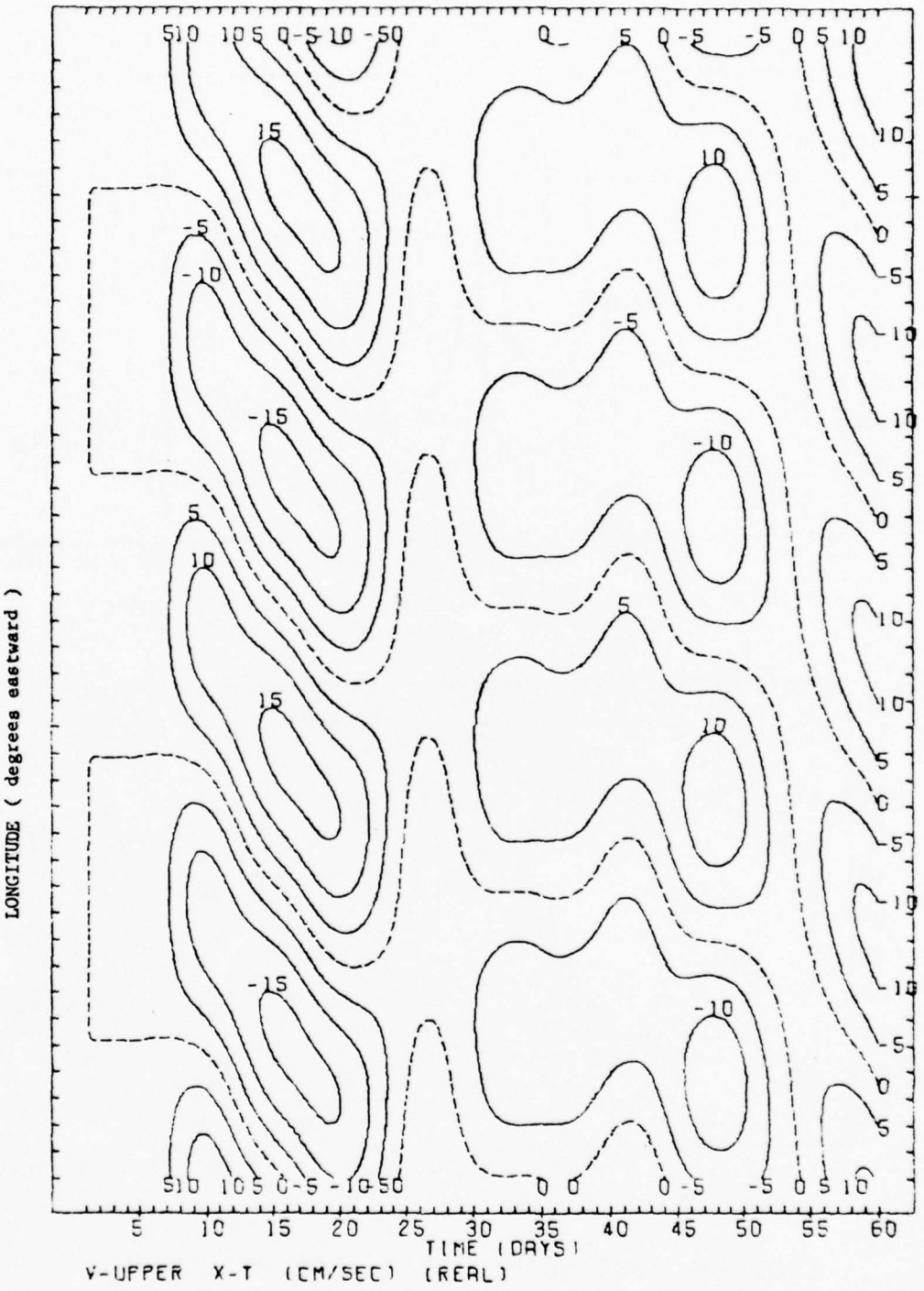
Figure 31





CASE 3: FORCING = STEP 2. NO MEAN FLOW

Figure 32



CASE 3: FORCING = STEP 2. NO MEAN FLOW

Figure 33

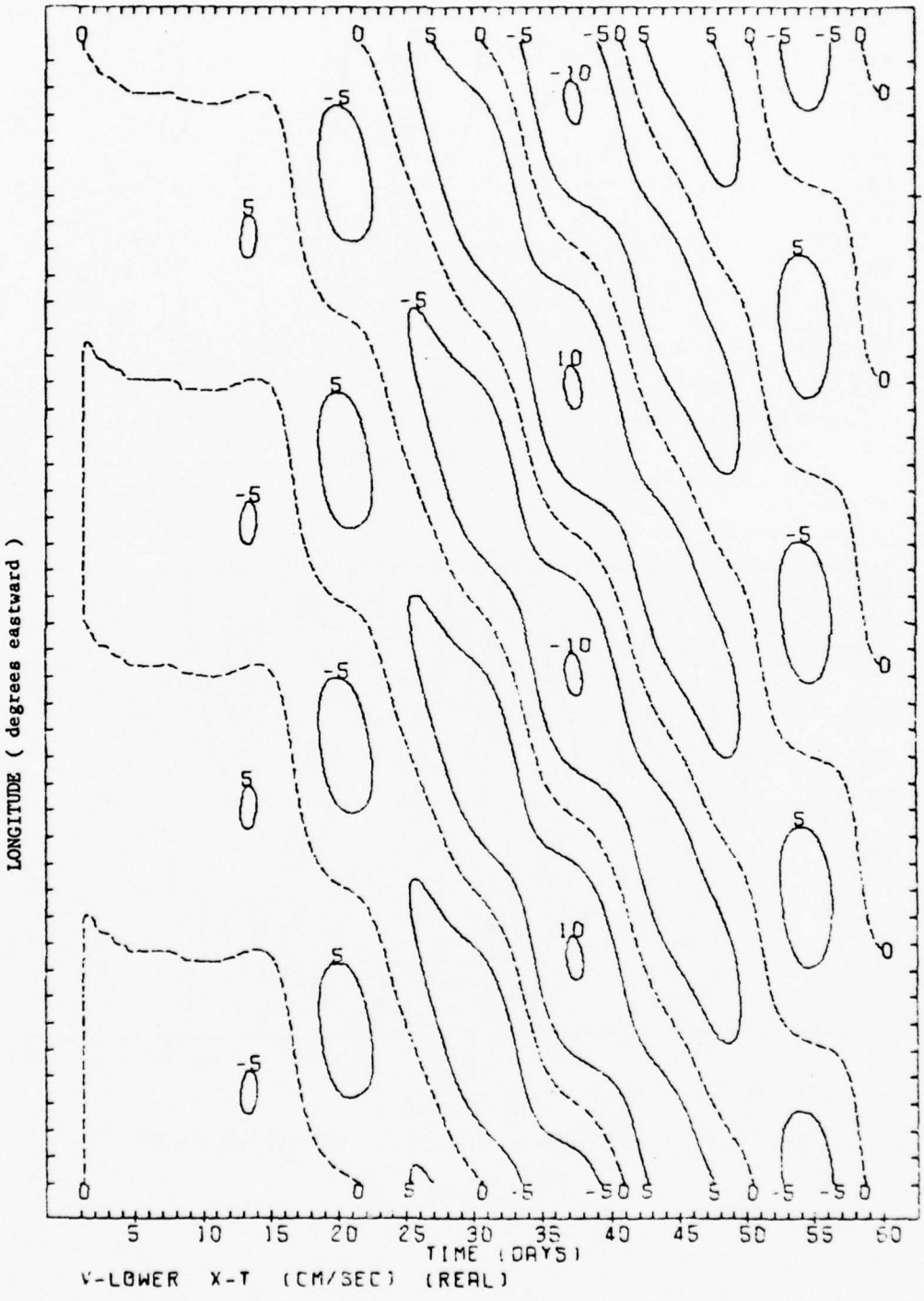
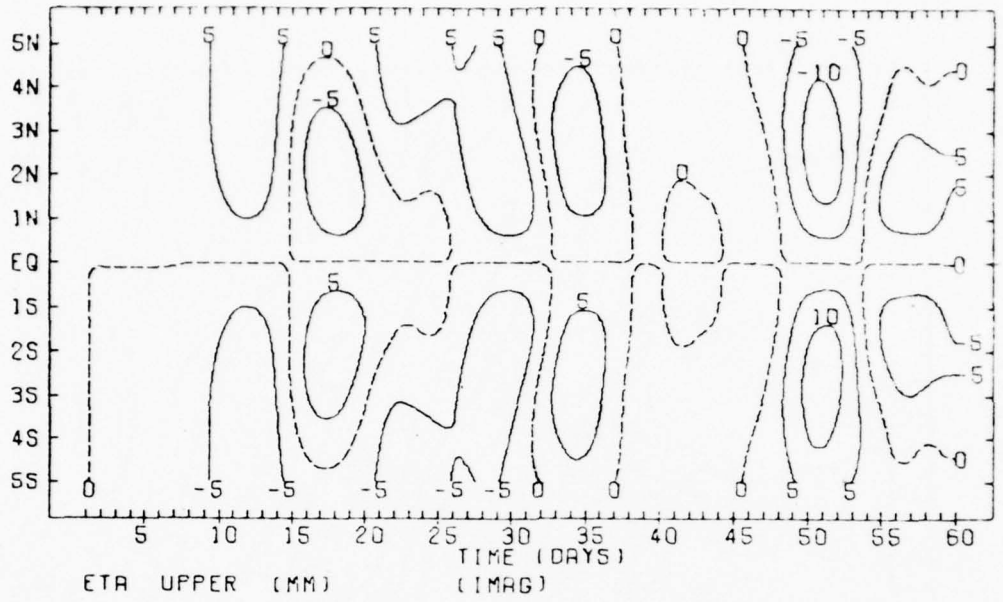
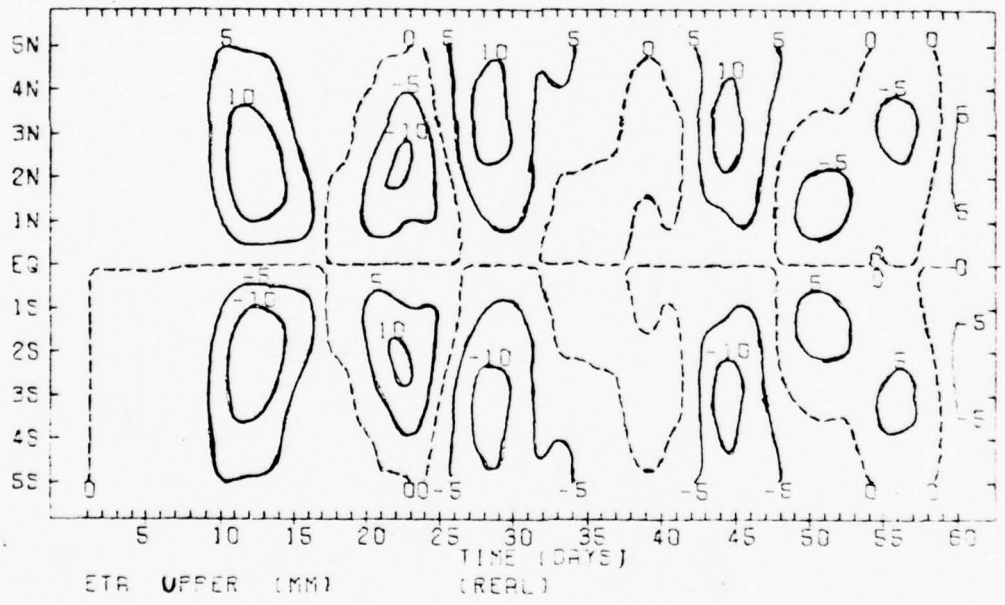

LONGITUDE (degrees eastward)
5 10 15 20 25 30 35 40 45 50 55 60
TIME (DAYS)
V-LOWER X-T (CM/SEC) (REAL)
CASE 3: FORCING = STEP 2. NO MEAN FLOW

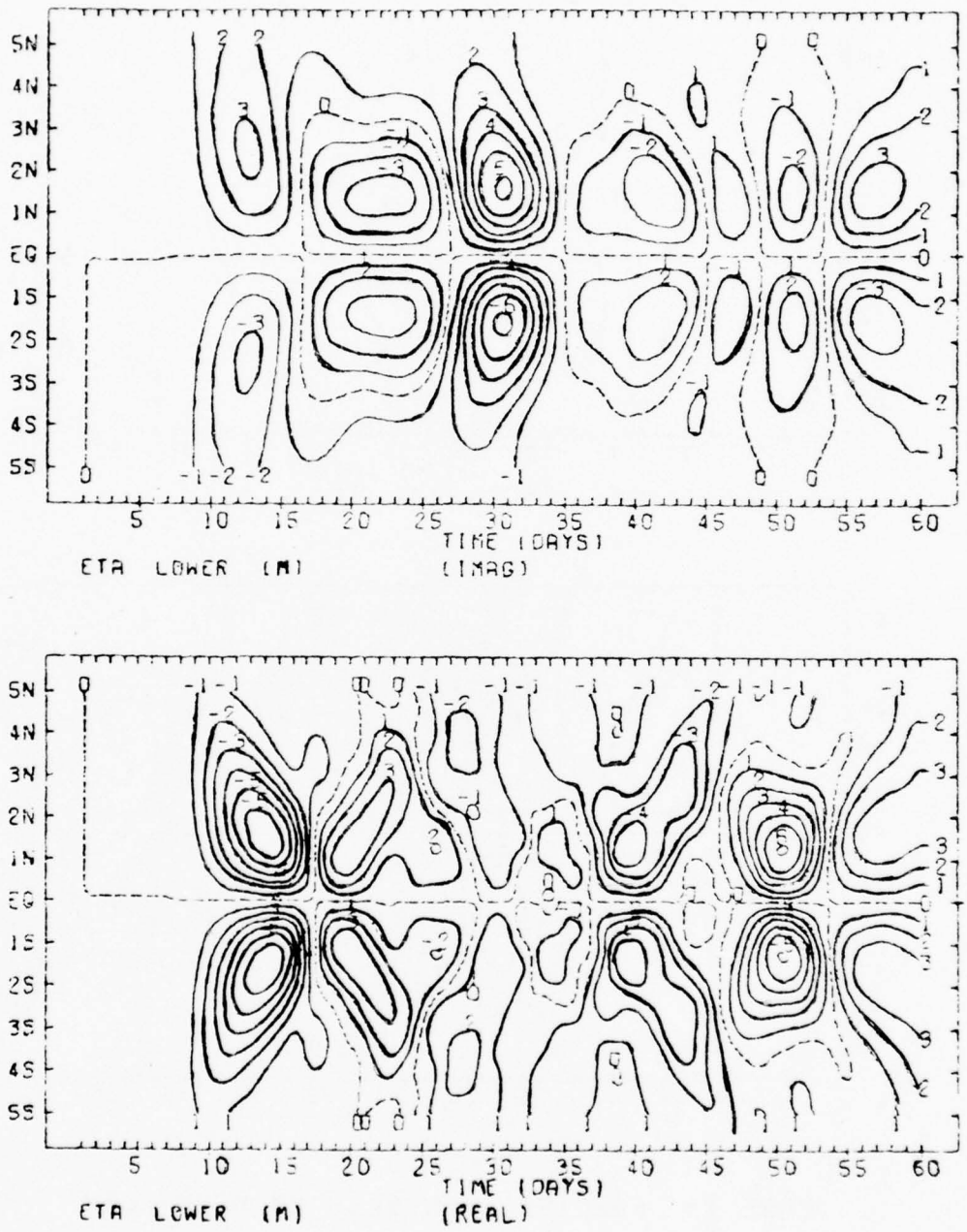
Figure 34





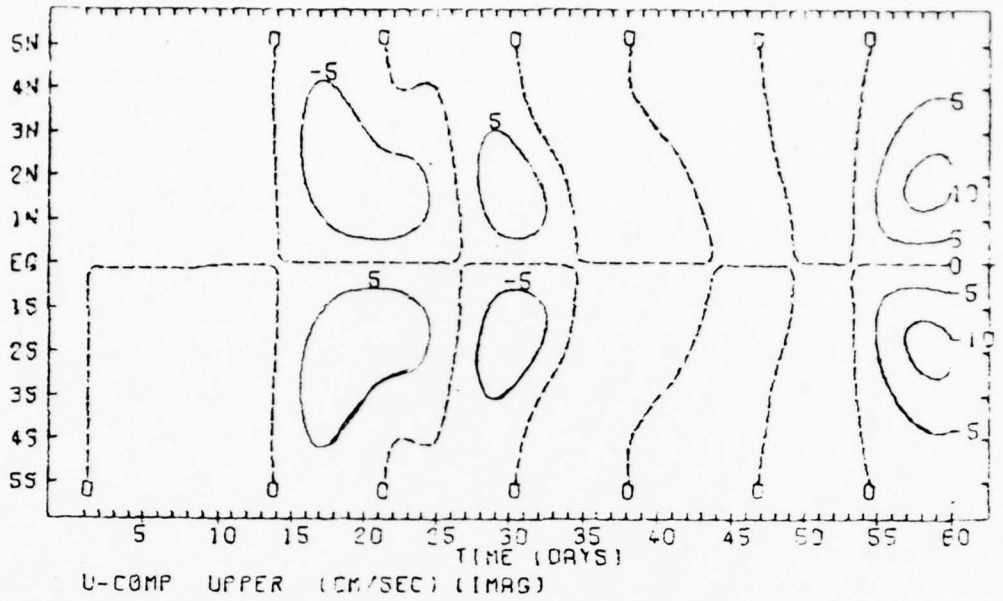
CASE 4: FORCING = PULSE. NO MEAN FLOW

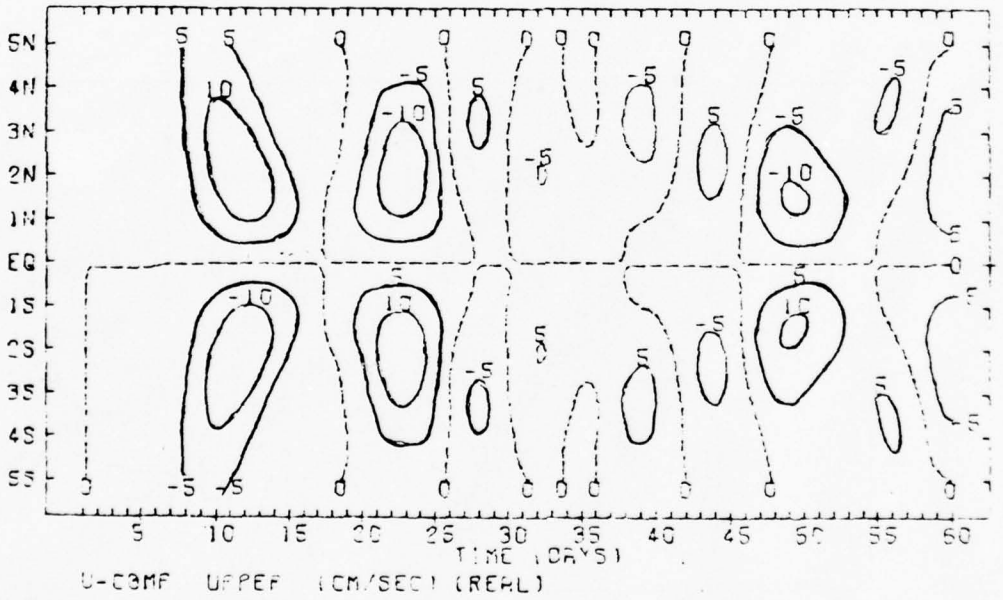
Figure 35



CASE 4: FORCING = PULSE. NO MEAN FLOW

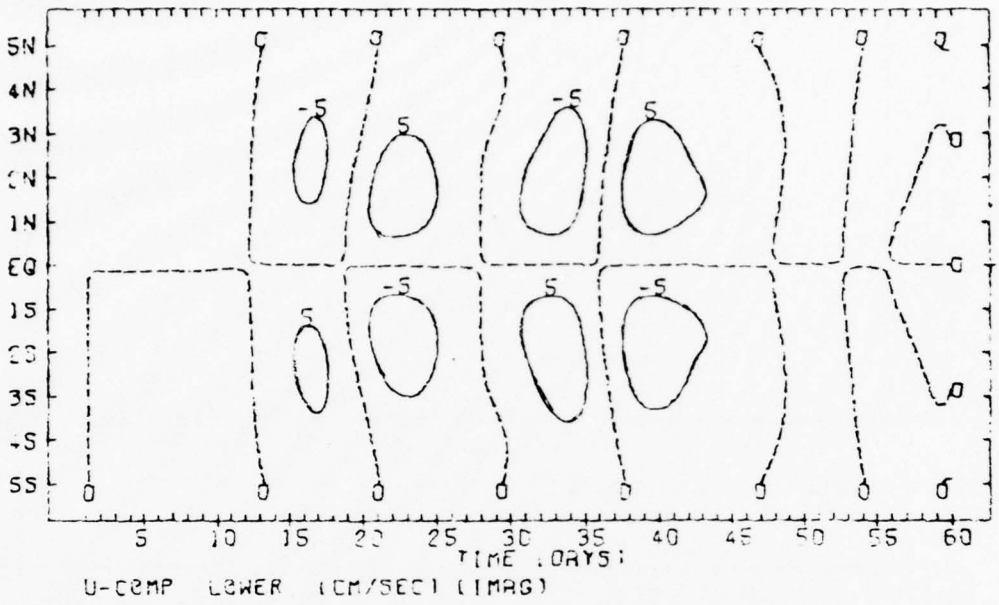
Figure 36

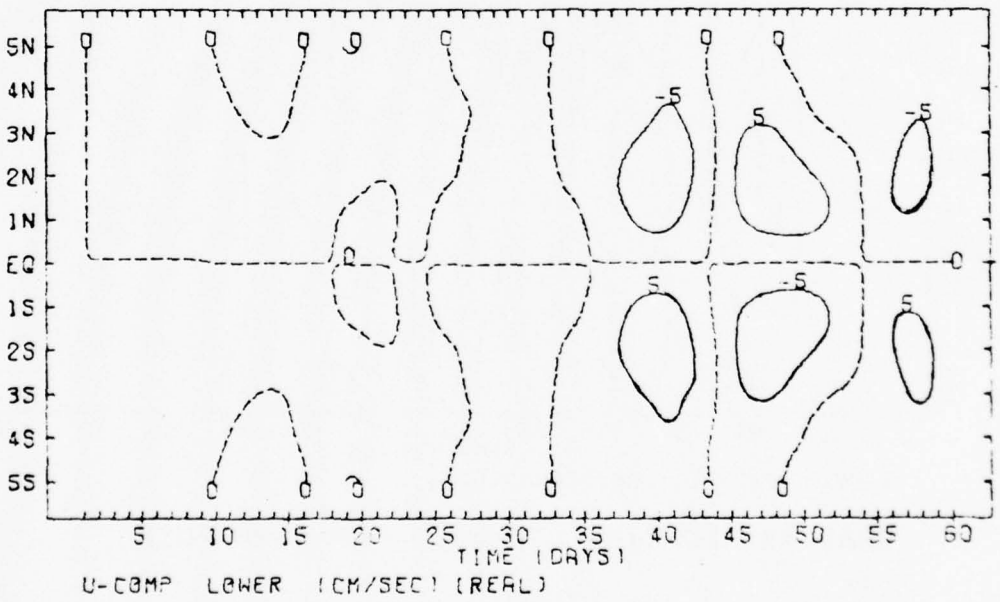




CASE 4: FORCING = PULSE. NO MEAN FLOW

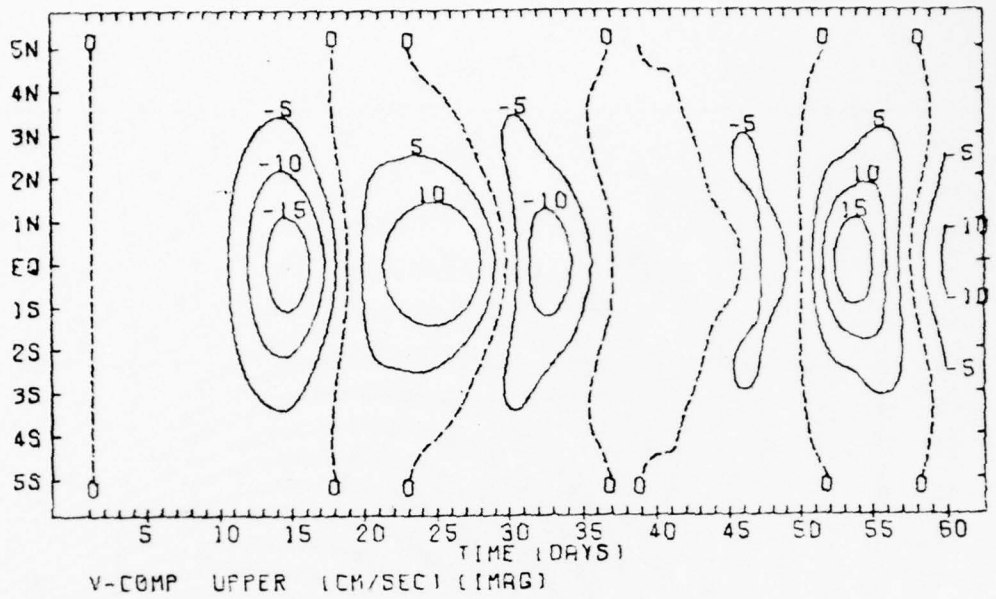
Figure 37



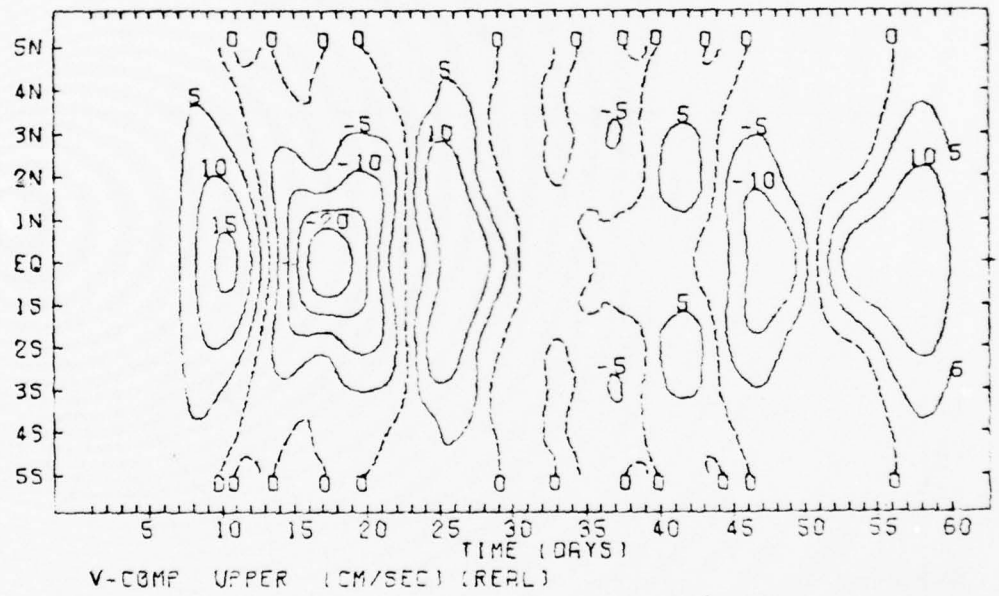


CASE 4: FORCING = PULSE. NO MEAN FLOW

Figure 38



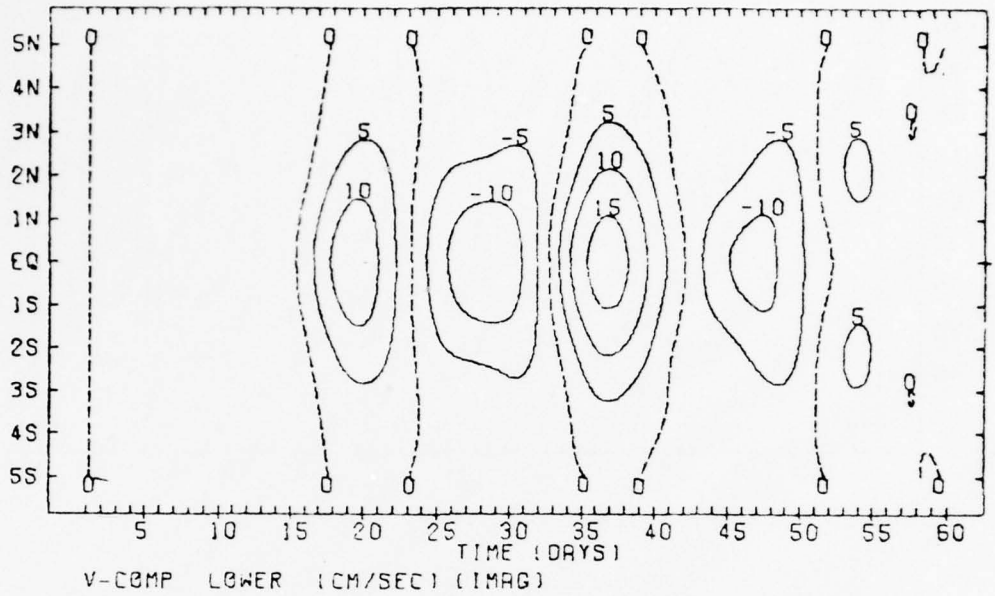
V-COMP UPPER (CM/SEC) (IMAG)

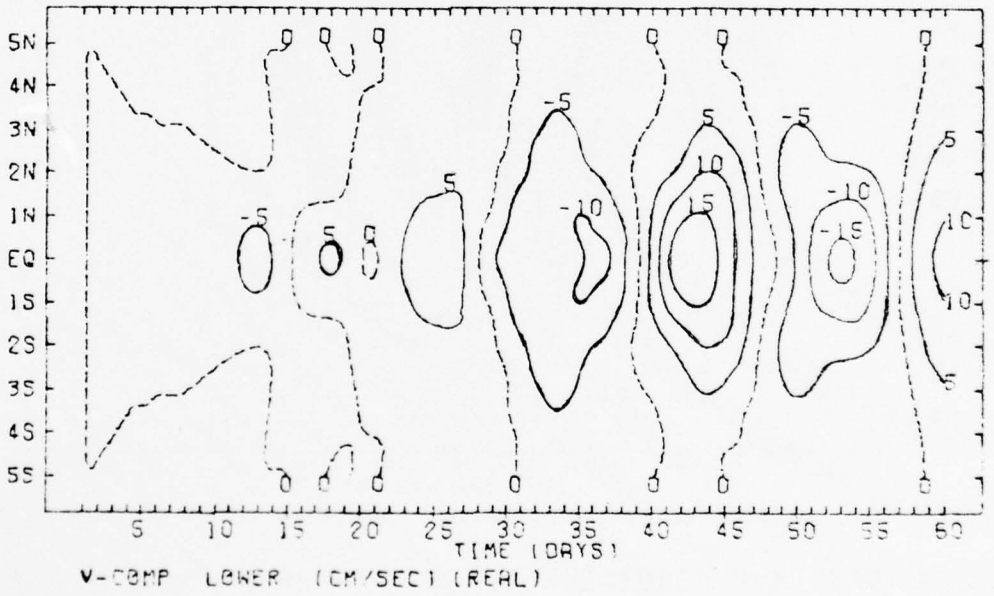


V-COMP UPPER (CM/SEC) (REAL)

CASE 4: FORCING = PULSE, NO MEAN FLOW

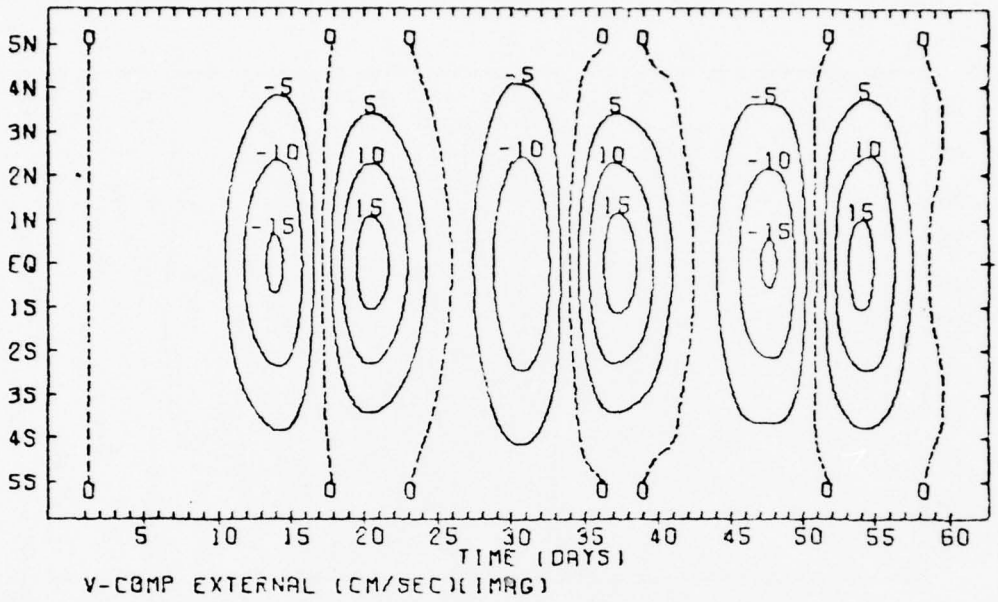
Figure 39

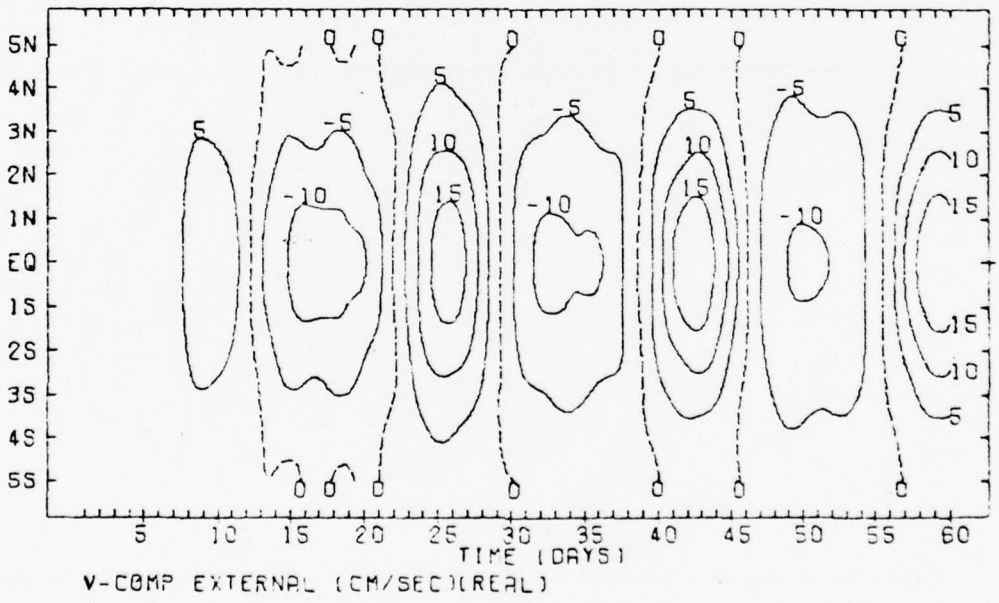




CASE 4: FORCING = PULSE. NO MEAN FLOW

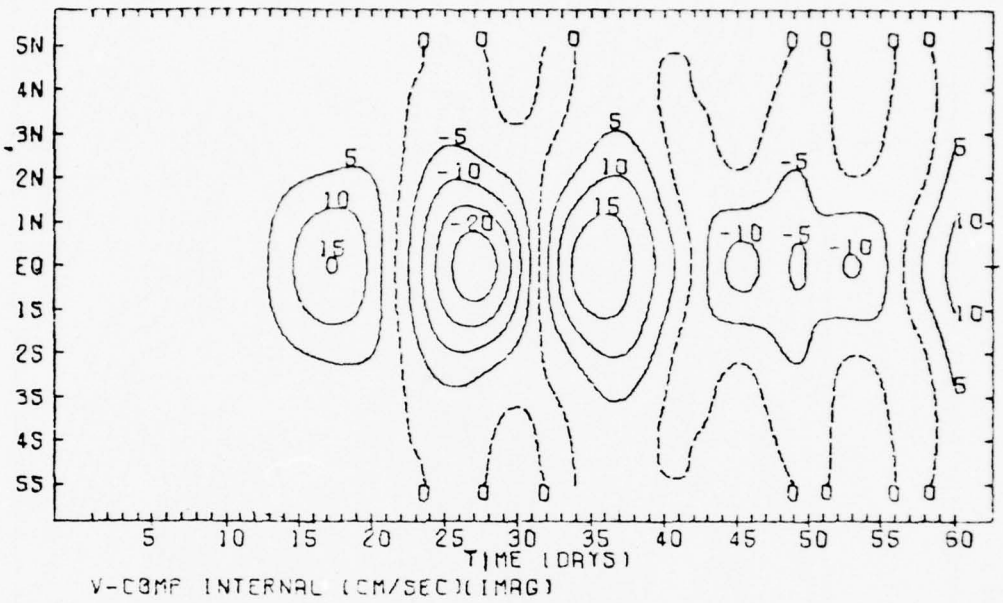
Figure 40

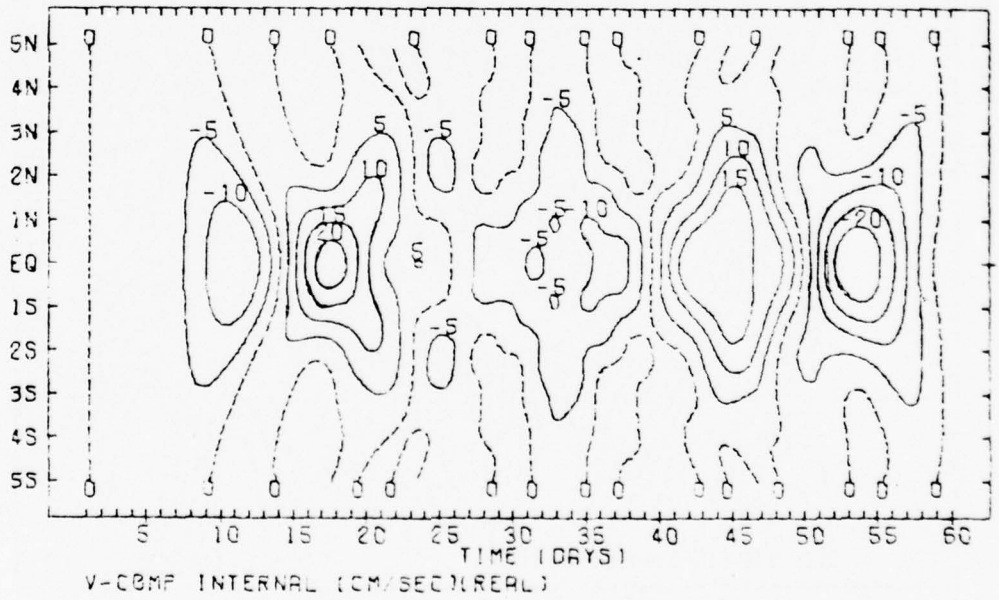




CASE 4: FORCING = PULSE. NO MEAN FLOW

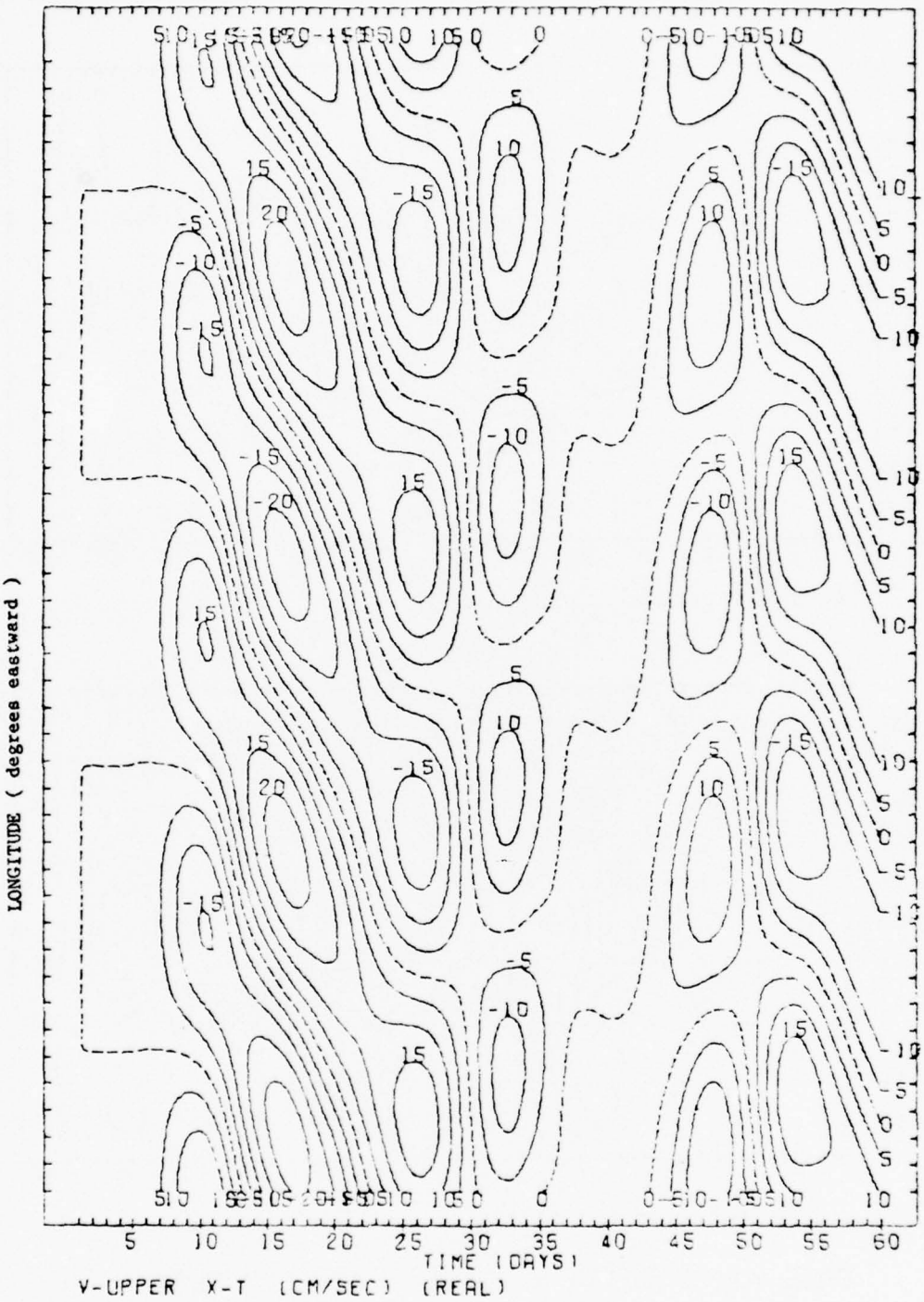
Figure 41





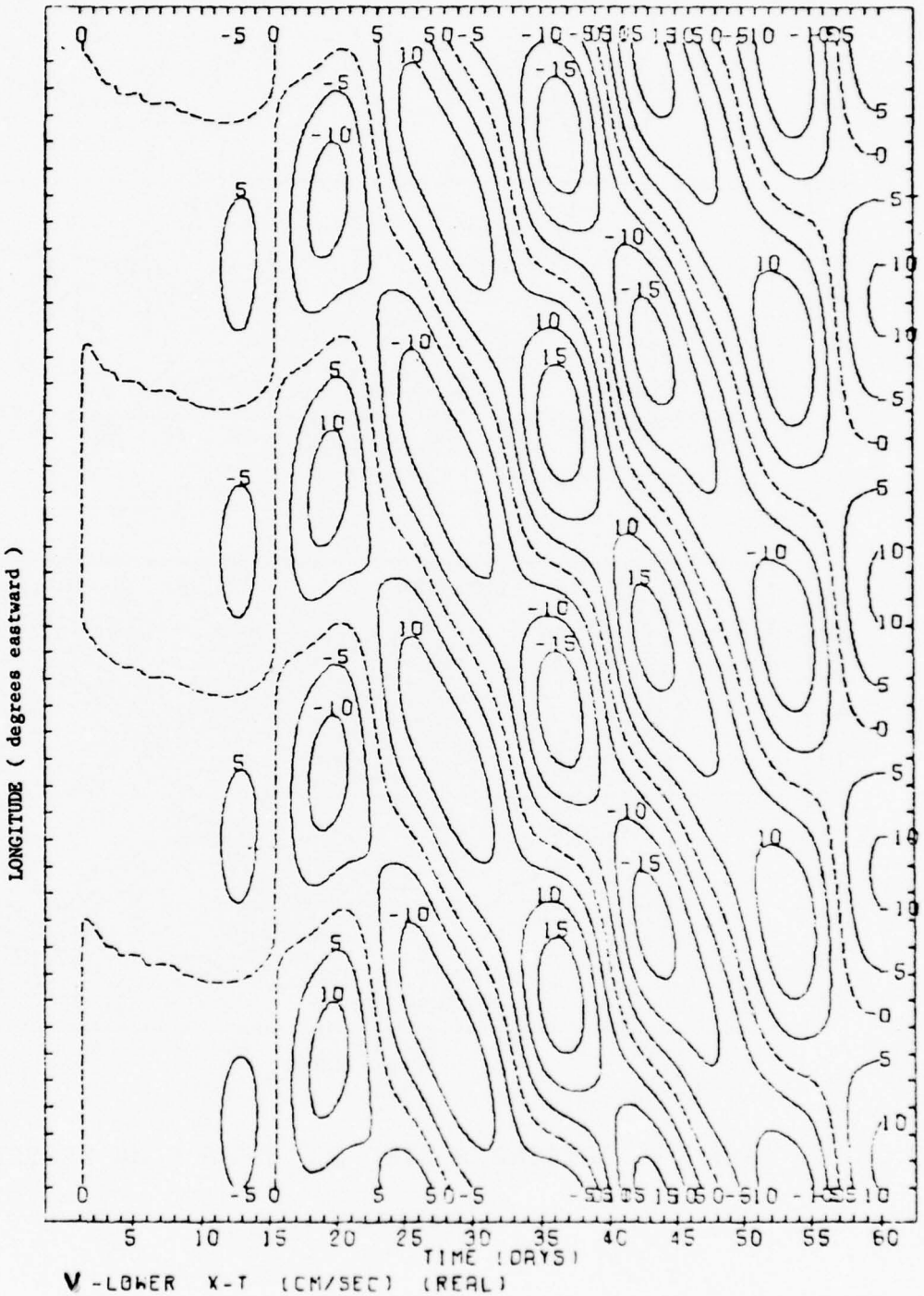
CASE 4: FORCING = PULSE, NO MEAN FLOW

Figure 42



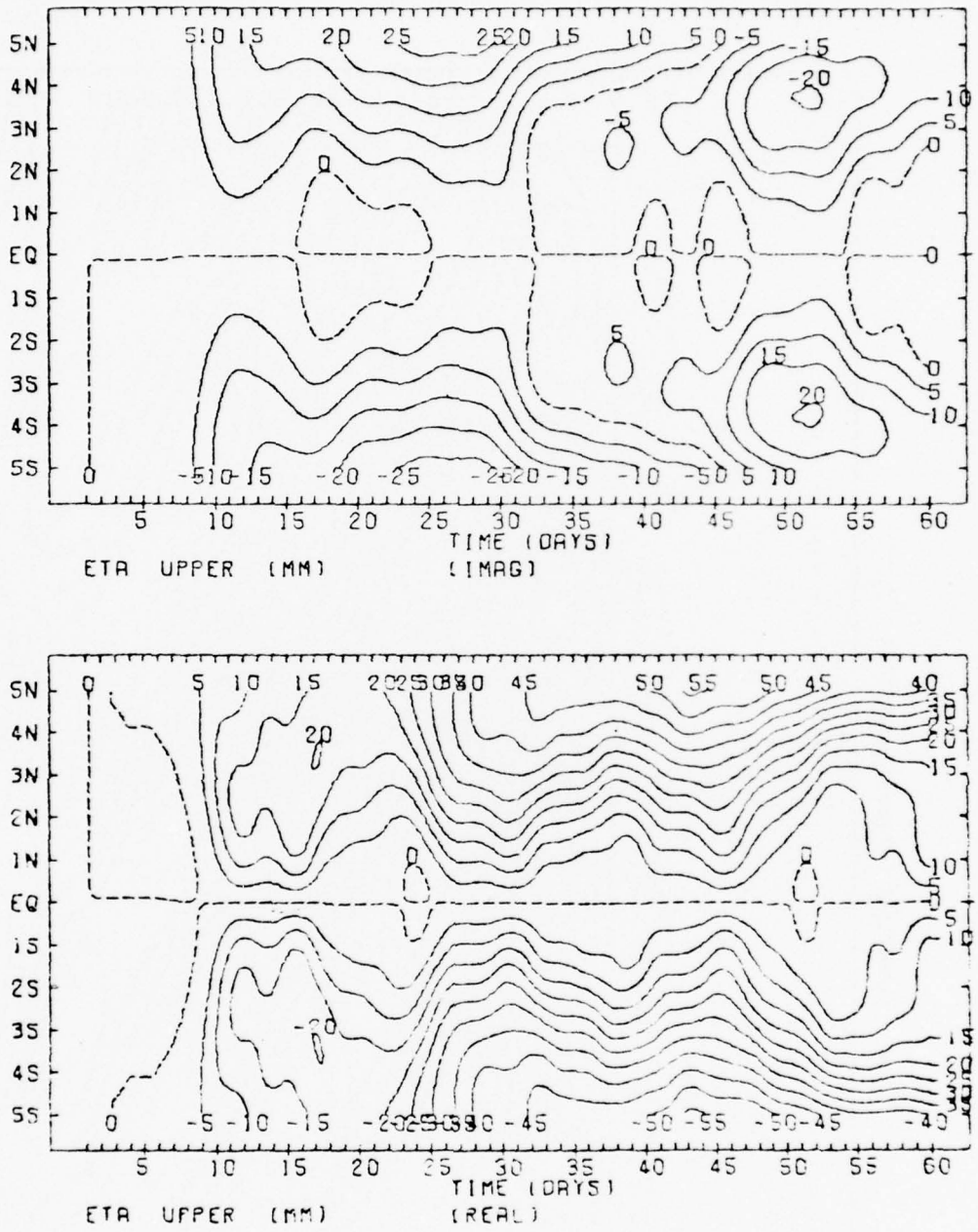
CASE 4: FORCING = PULSE. NO MEAN FLOW

Figure 43



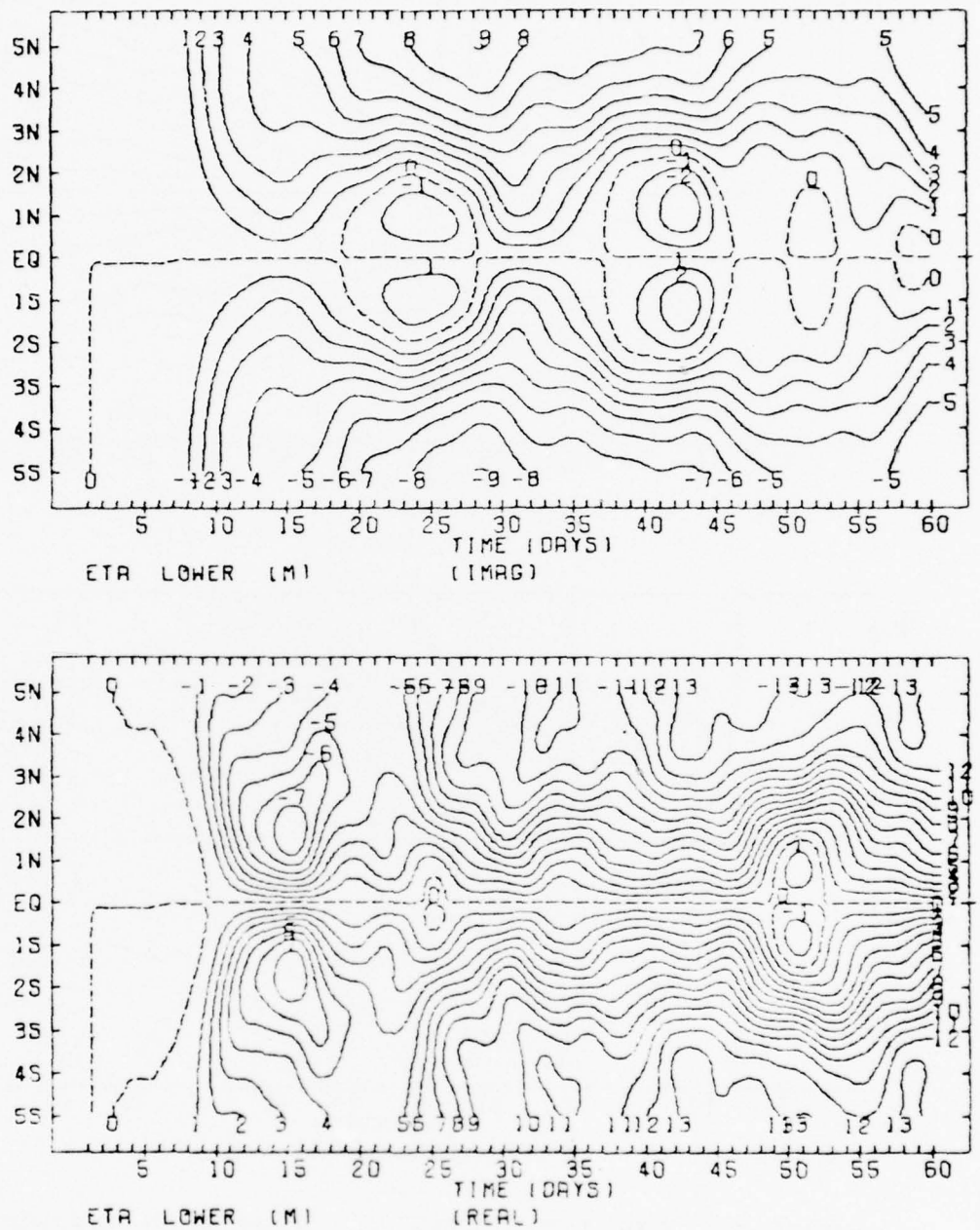
CASE 4: FORCING = PULSE. NO MEAN FLOW

Figure 44



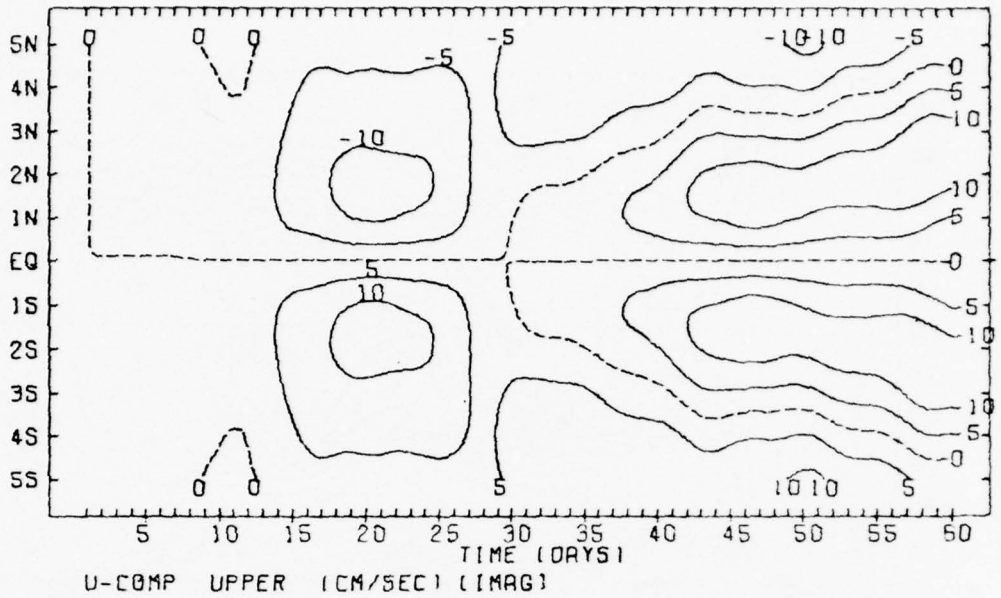
CASE 5: FORCING = STEP 2. MEAN FLOW PRESENT

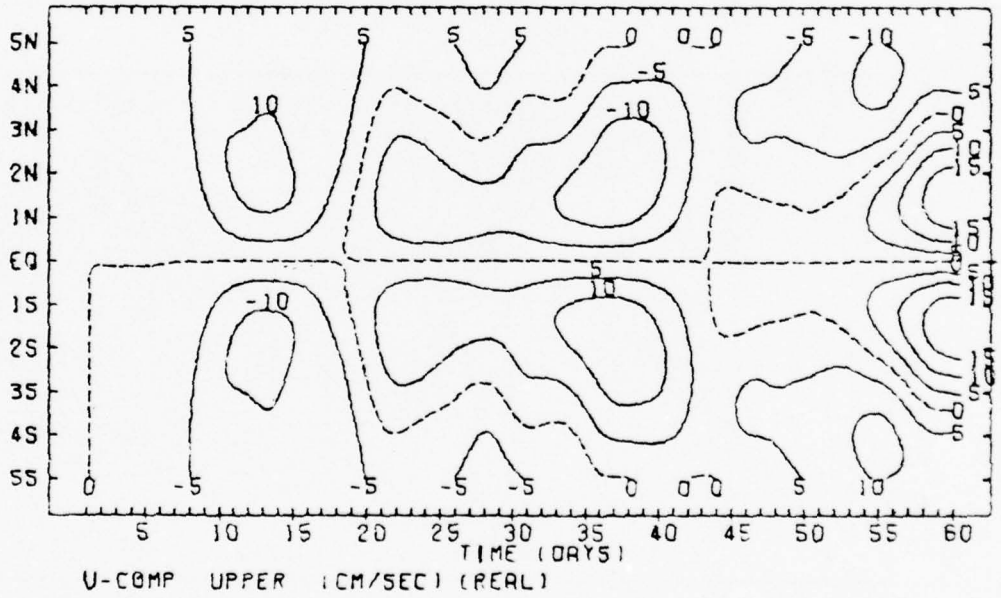
Figure 45



CASE 5: FORCING = STEP 2. MEAN FLOW PRESENT

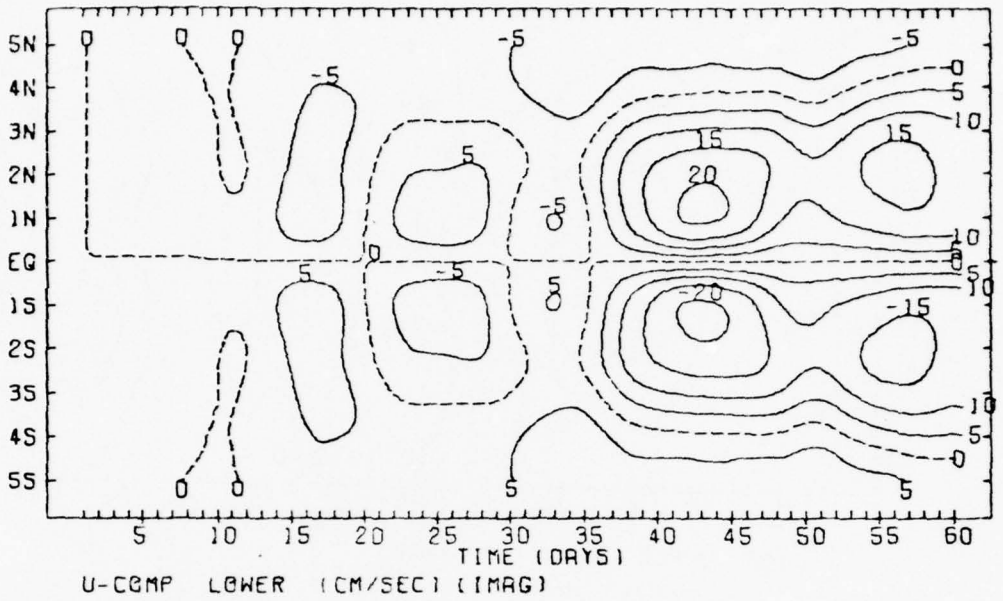
Figure 46

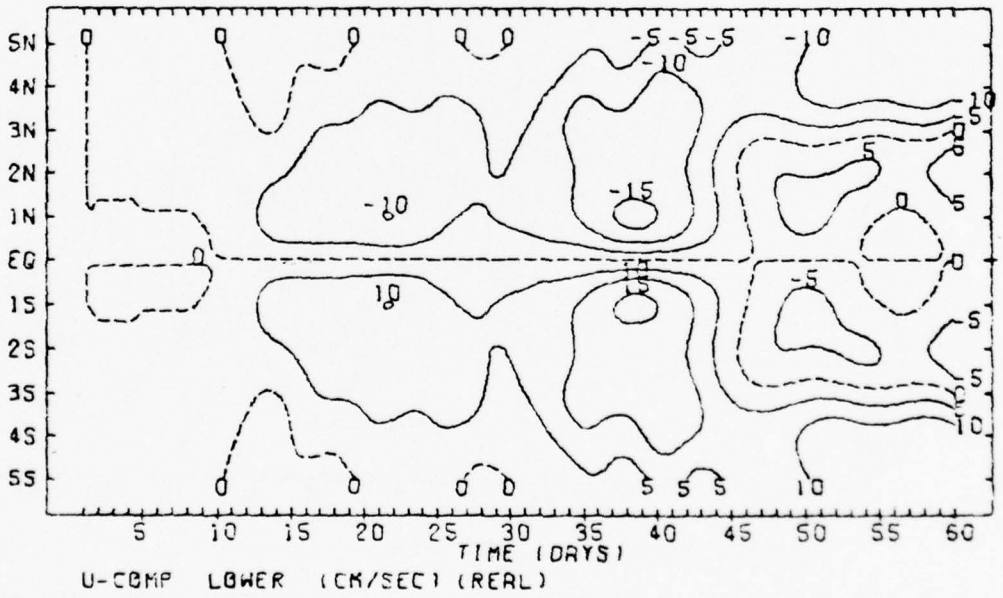




CASE 5: FORCING = STEP 2. MEAN FLOW PRESENT

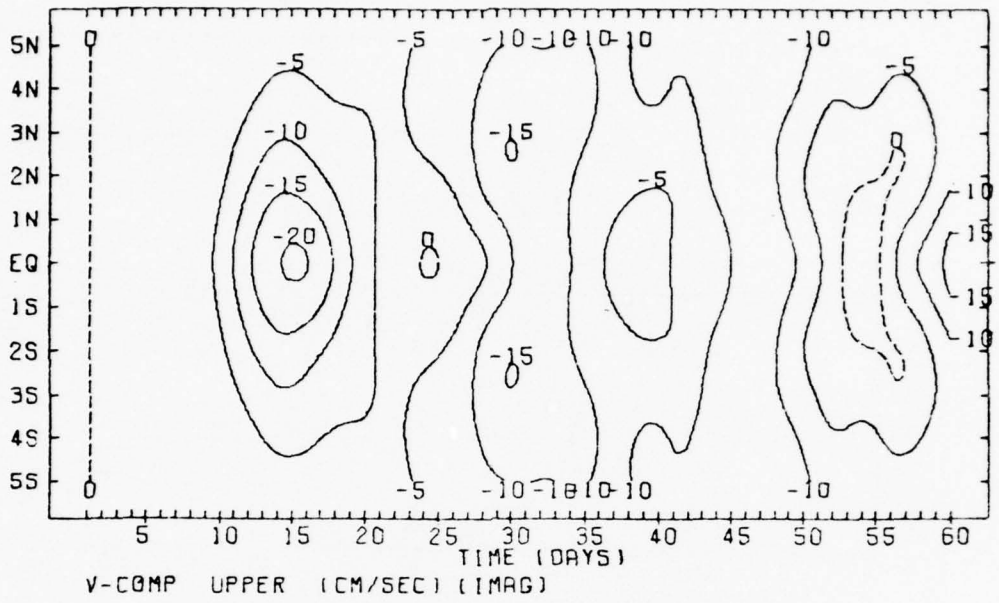
Figure 47

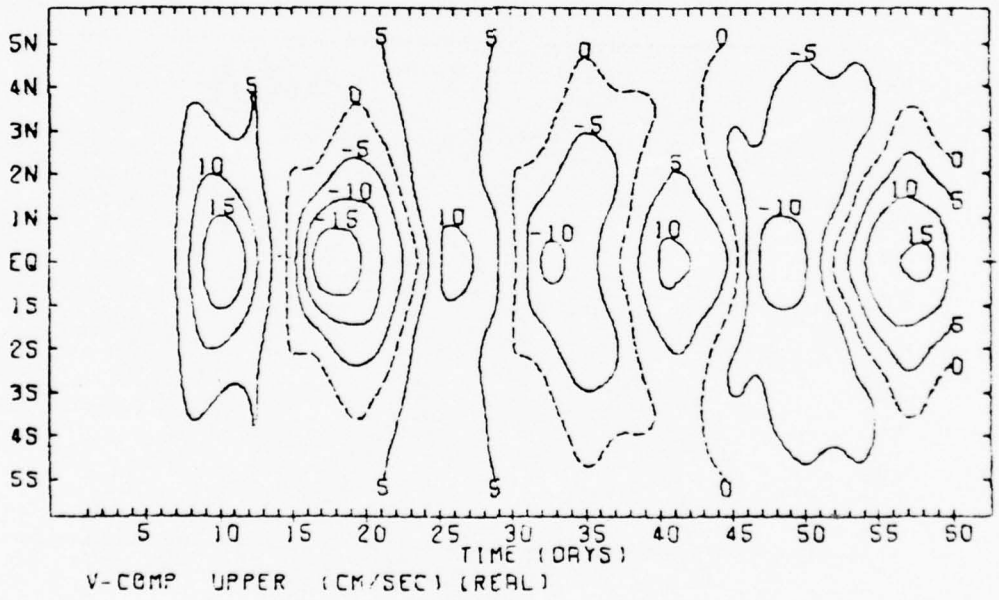




CASE 5: FORCING = STEP 2. MEAN FLOW PRESENT

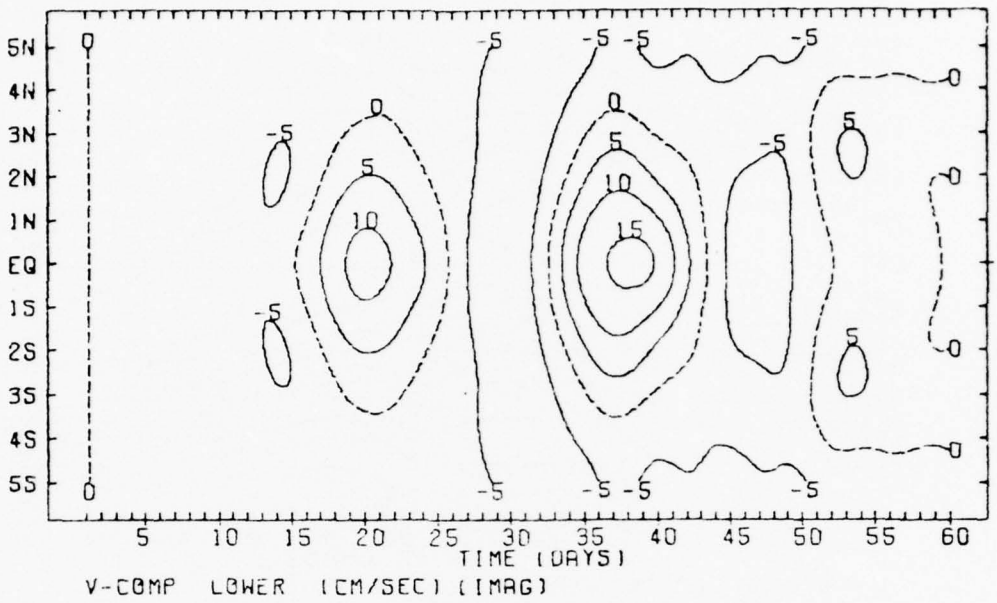
Figure 48

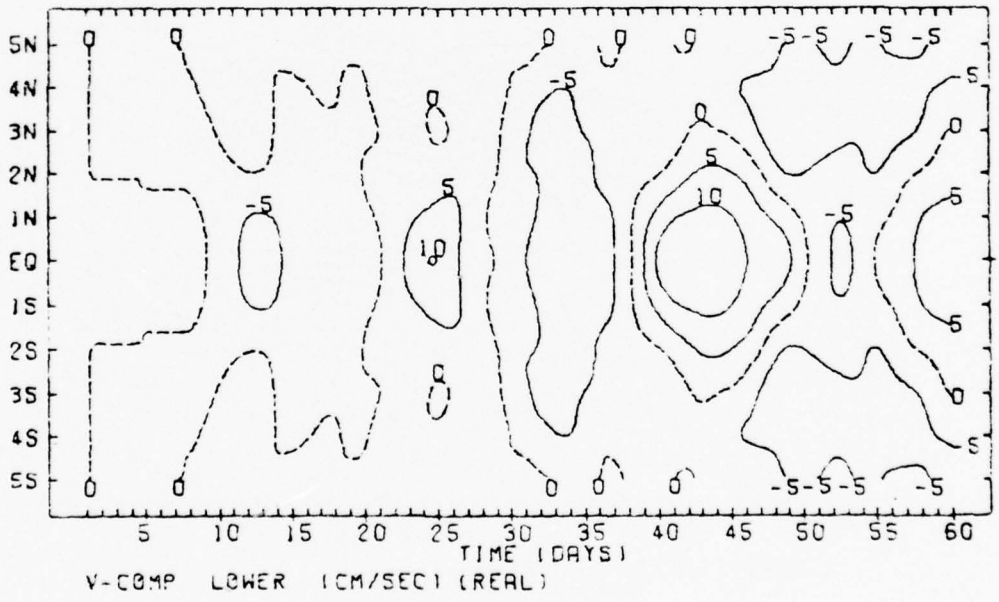




CASE 5: FORCING = STEP 2. MEAN FLOW PRESENT

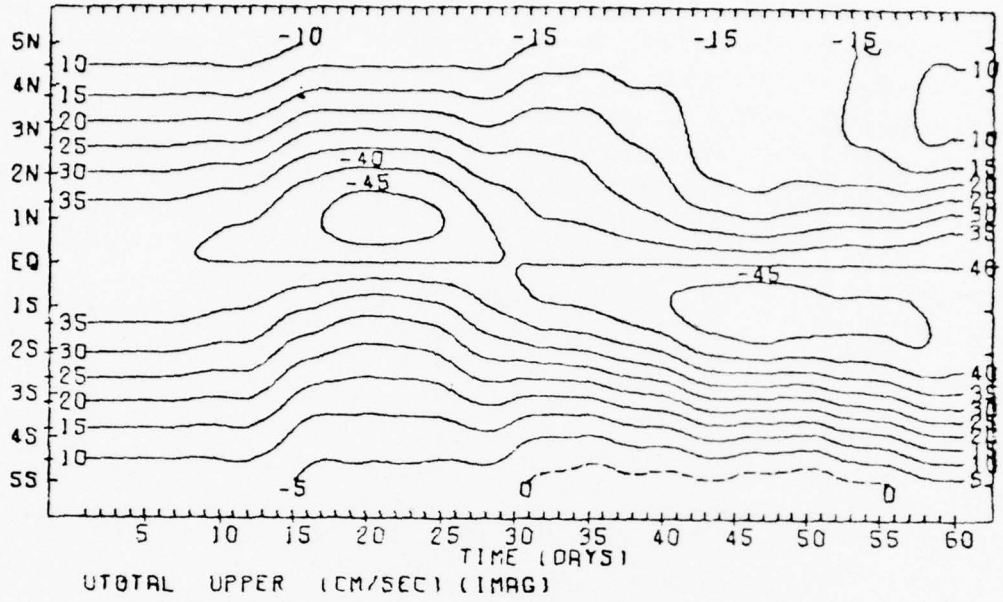
Figure 49

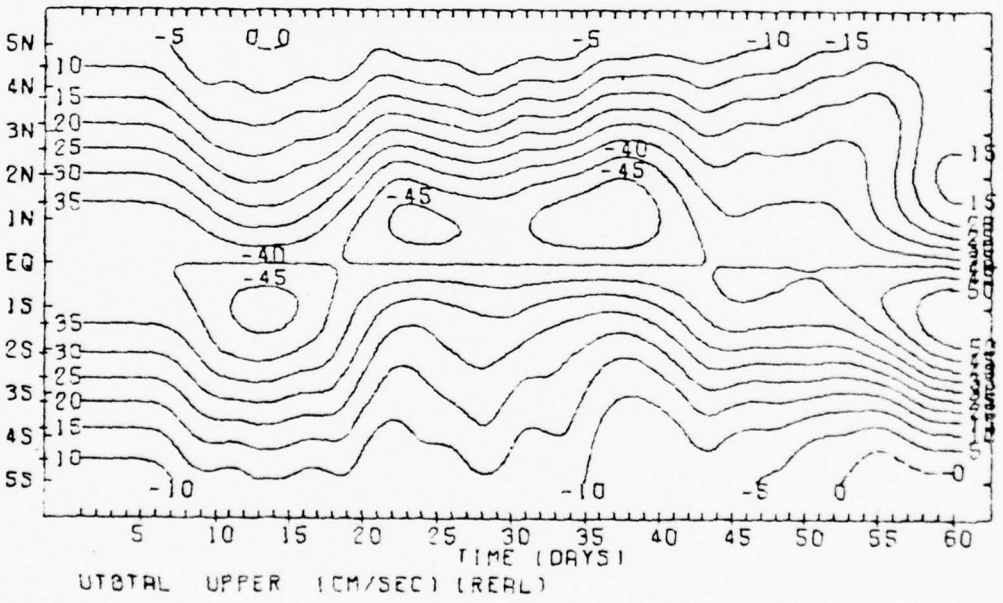




CASE 5: FORCING = STEP 2. MEAN FLOW PRESENT

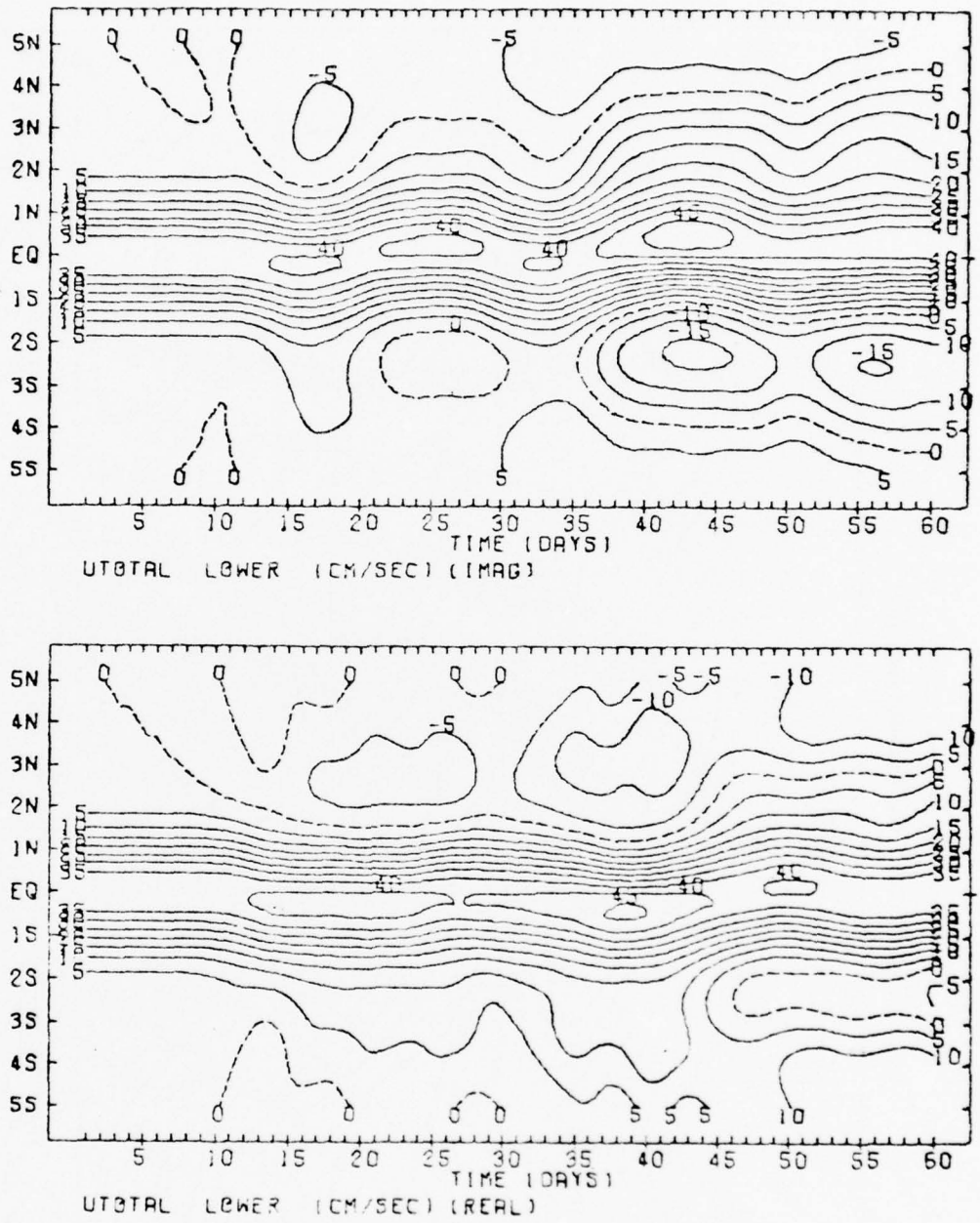
Figure 50





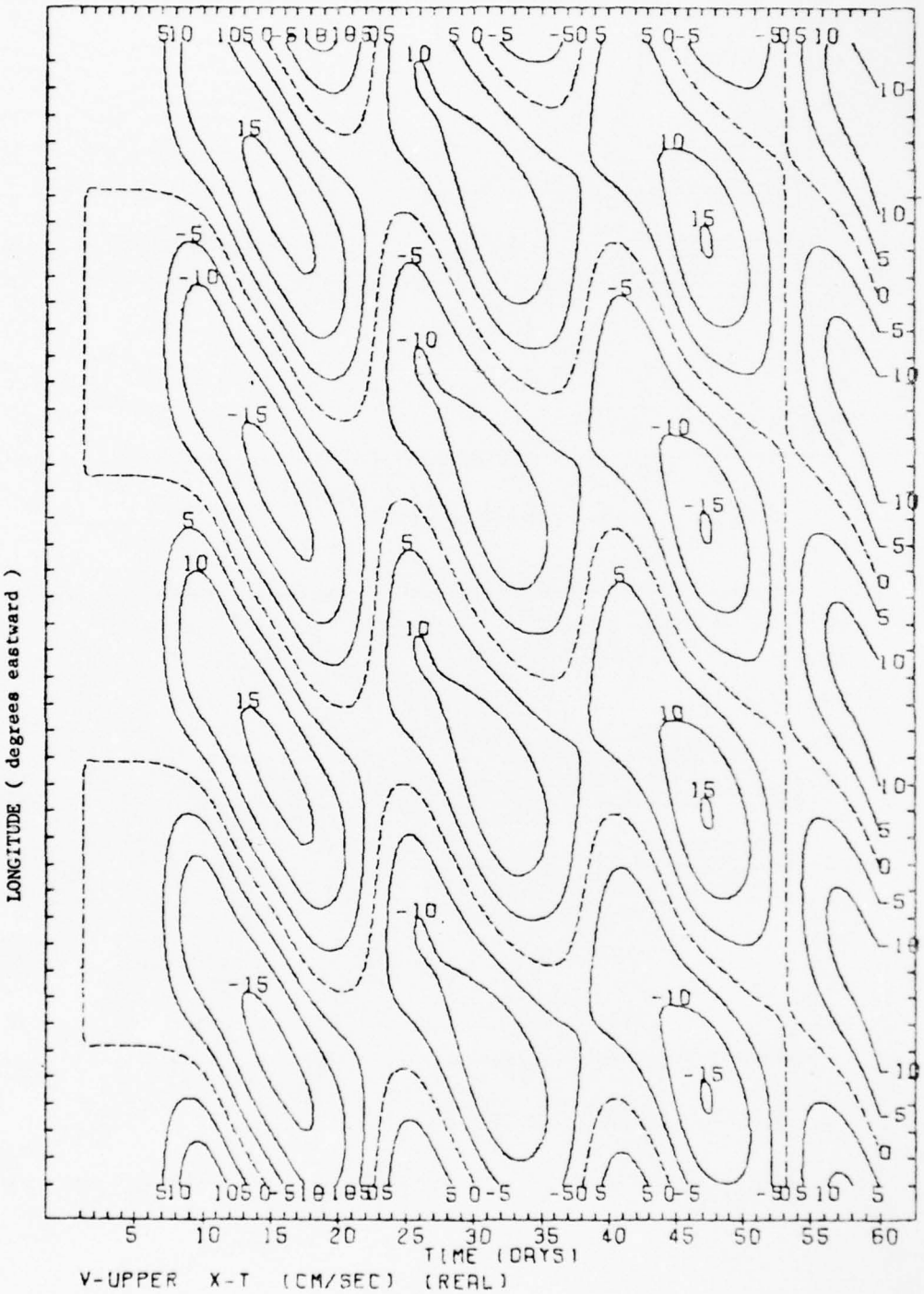
CASE 5: FORCING = STEP 2. MEAN FLOW PRESENT

Figure 51



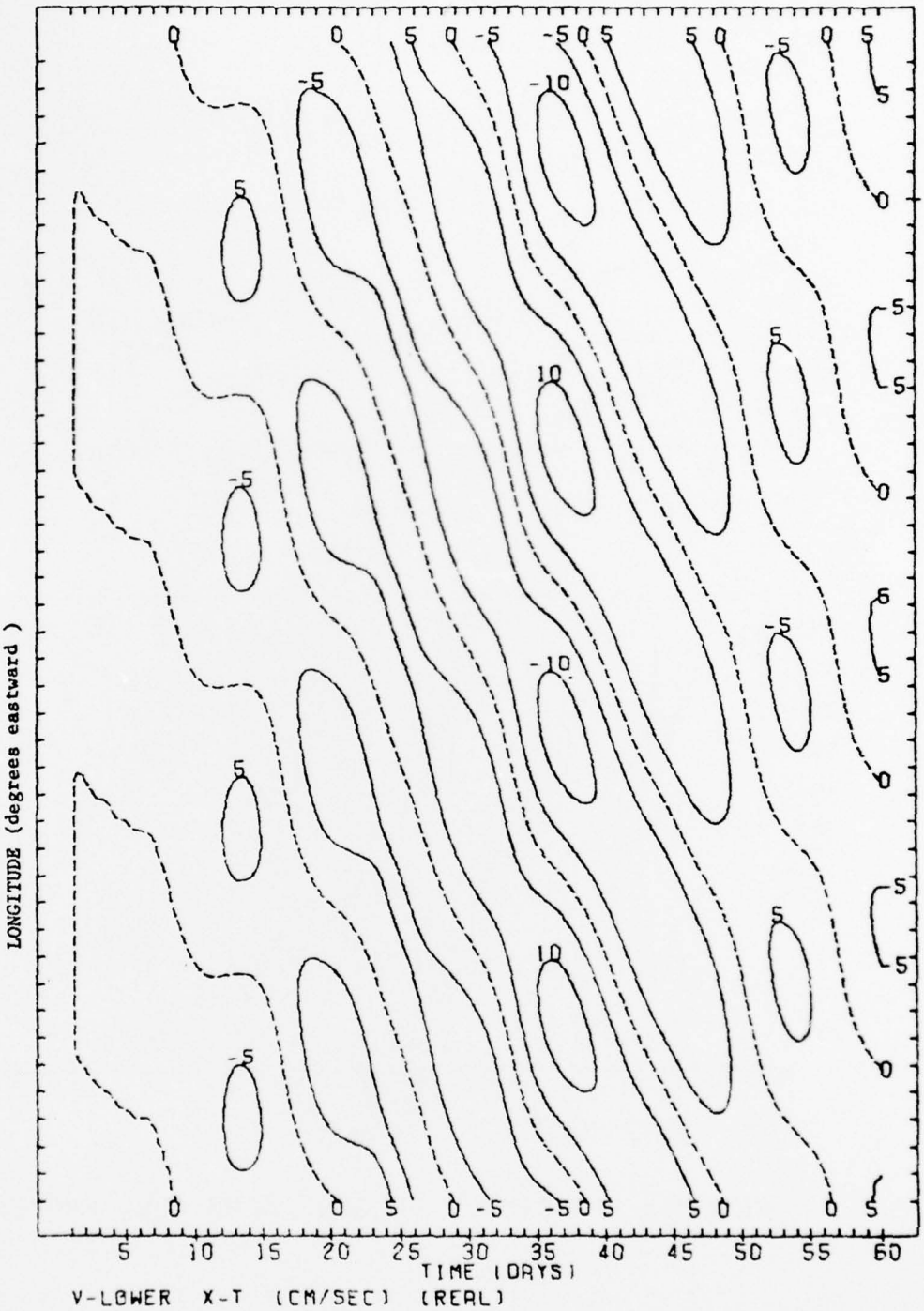
CASE 5: FORCING = STEP 2. MEAN FLOW PRESENT

Figure 52



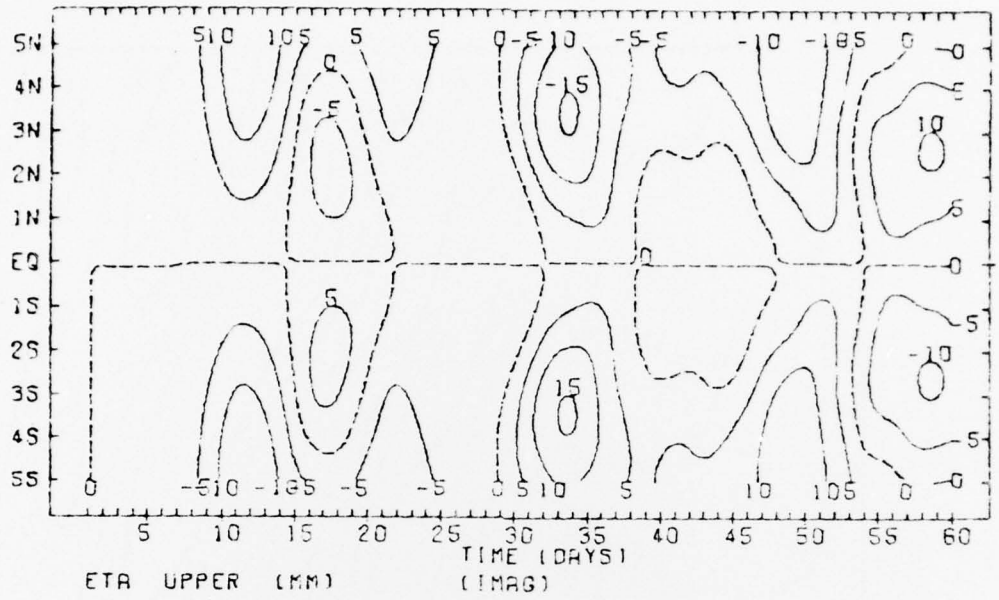
CASE 5: FORCING = STEP 2. MEAN FLOW PRESENT

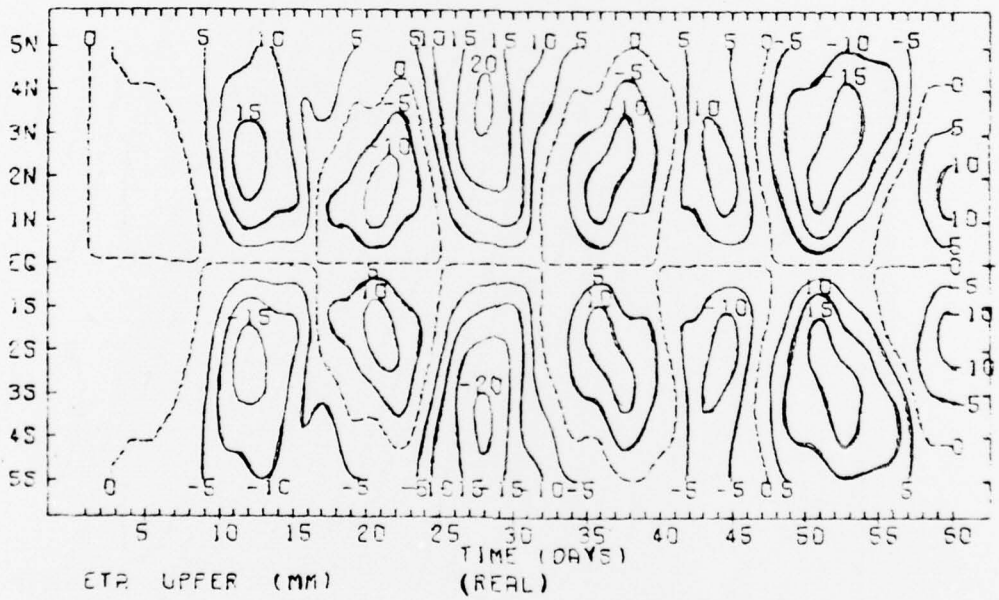
Figure 53



CASE 5 : FORCING = STEP 2. MEAN FLOW PRESENT

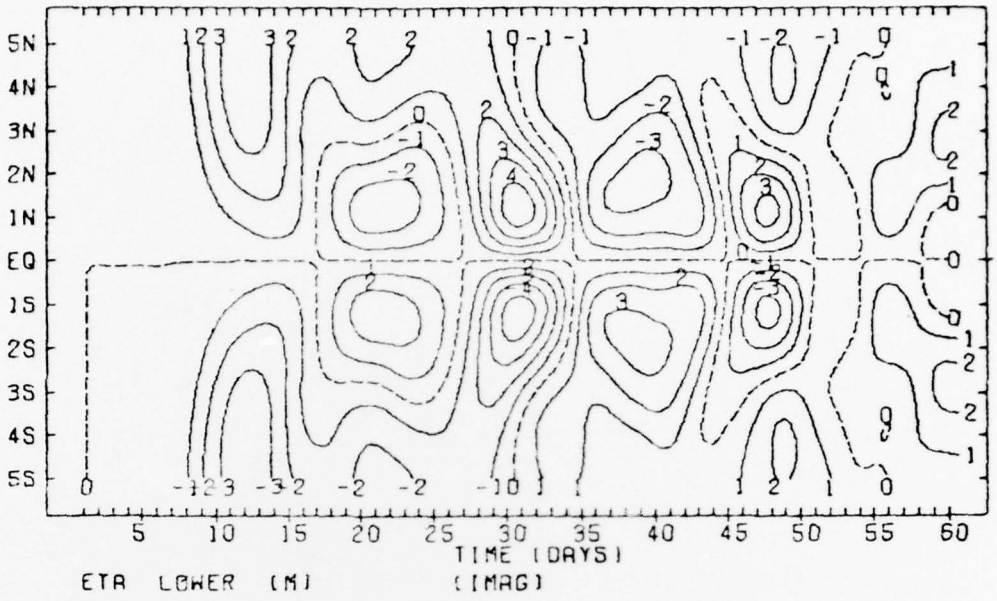
Figure 54

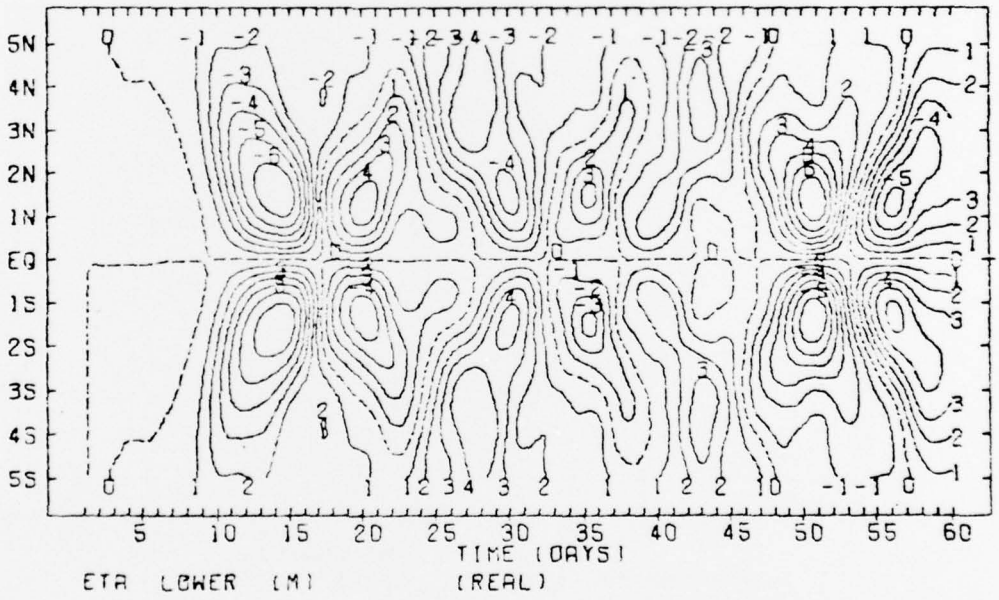




CASE 6: FORCING = PULSE. MEAN FLOW PRESENT

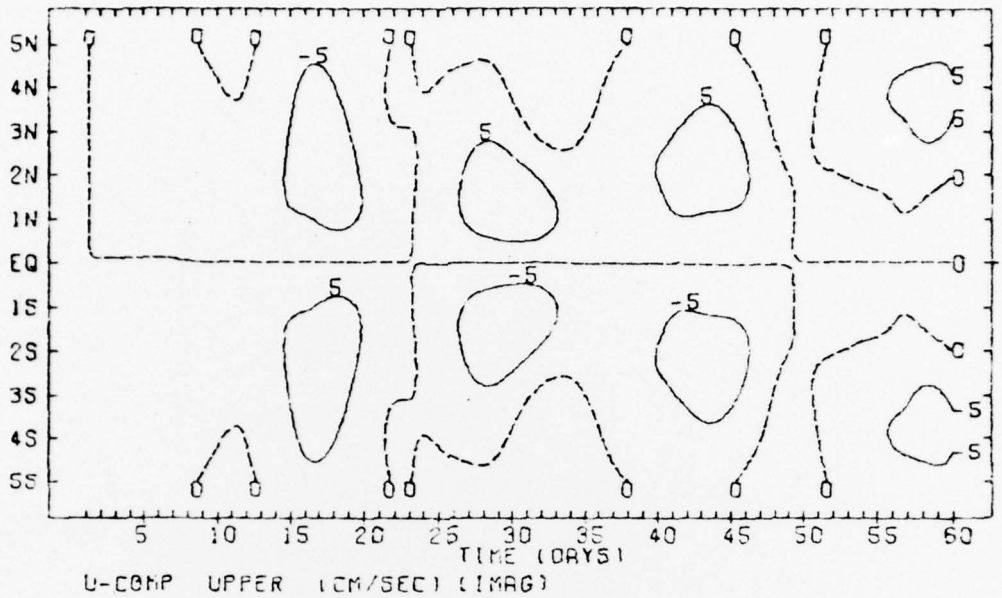
Figure 55

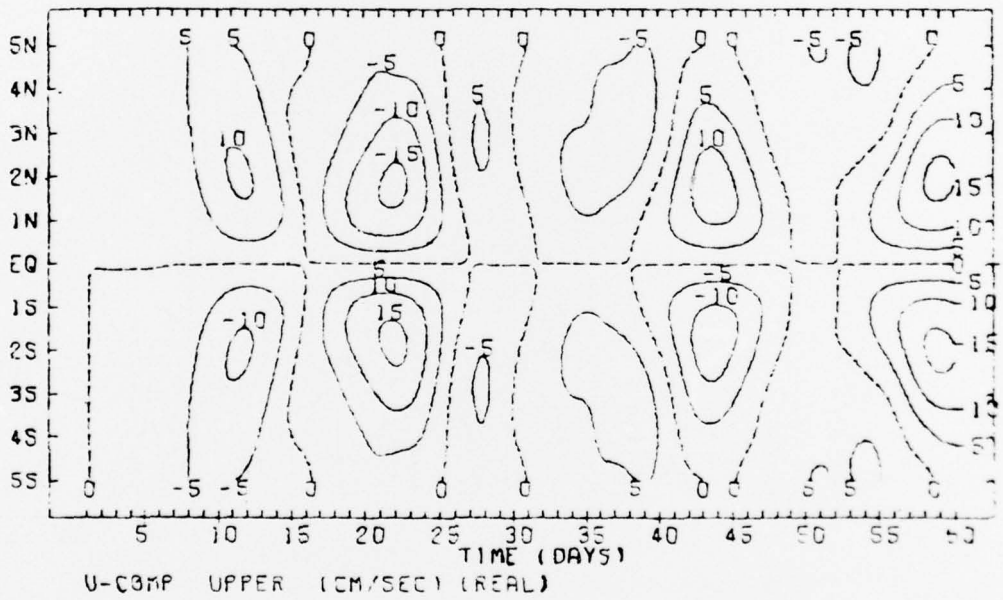




CASE 6 : FORCING = PULSE. MEAN FLOW PRESENT

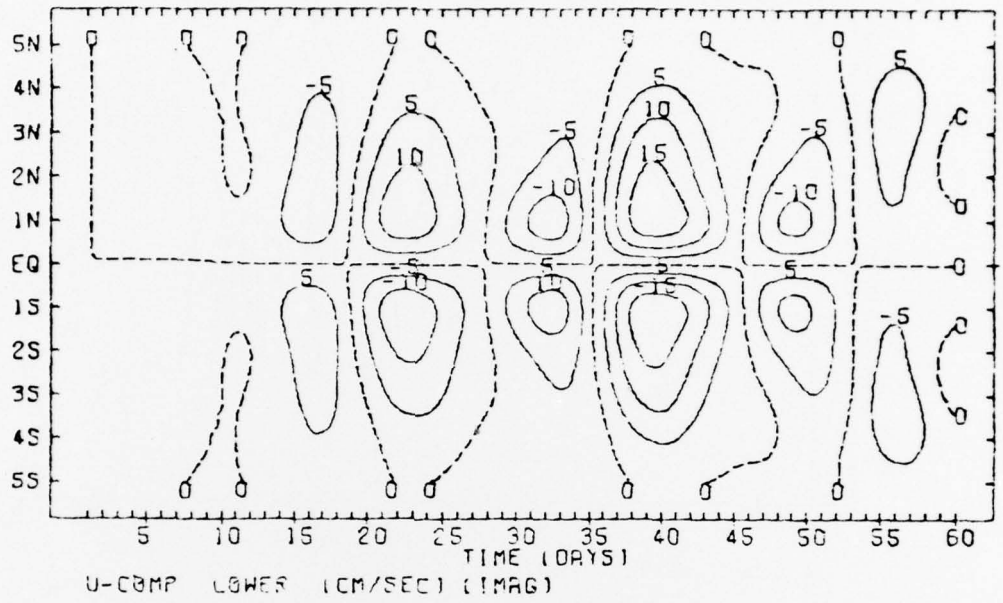
Figure 56

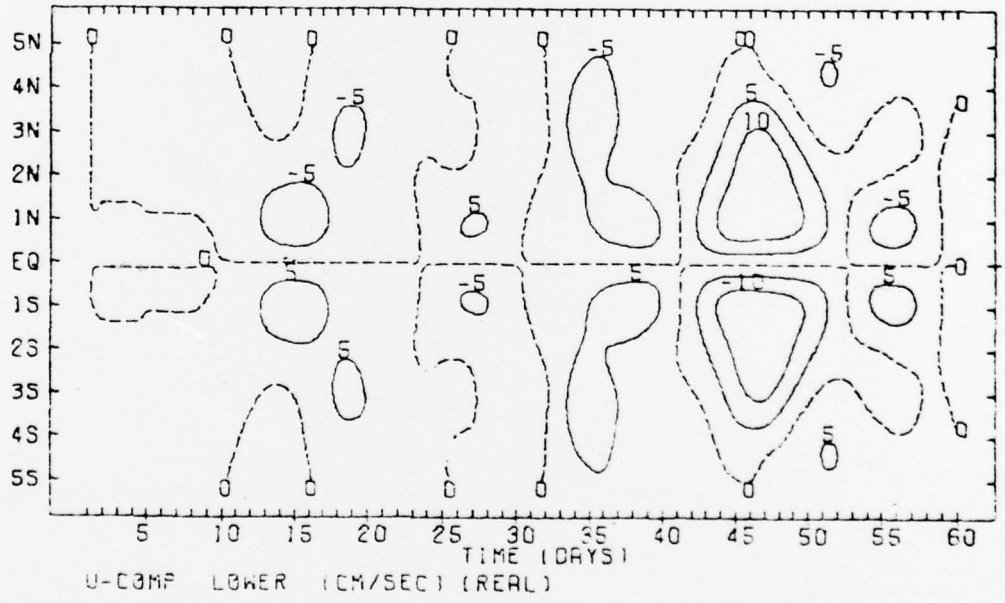




CASE 6 : FORCING = PULSE. MEAN FLOW PRESENT

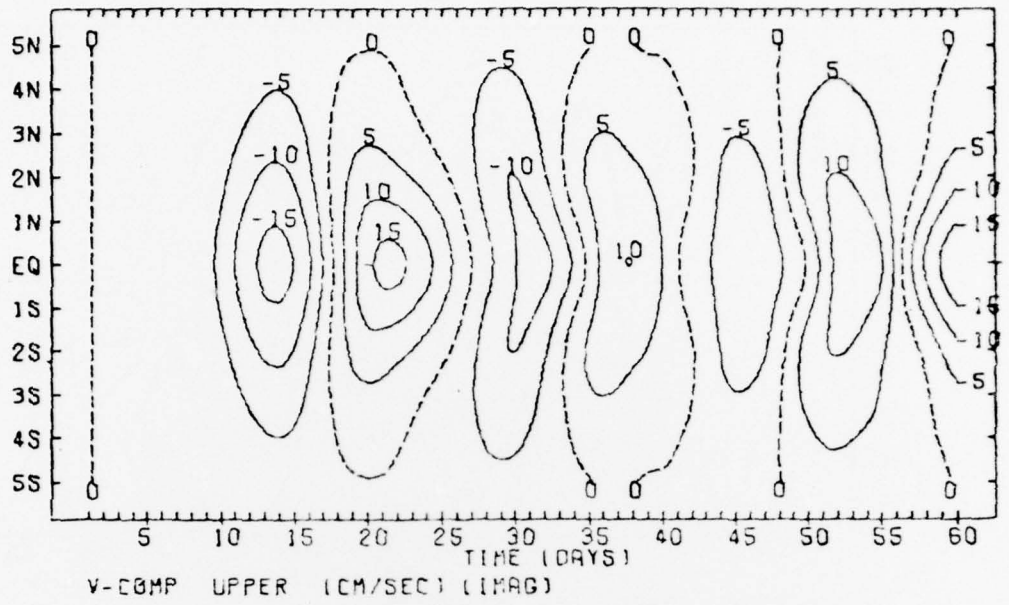
Figure 57

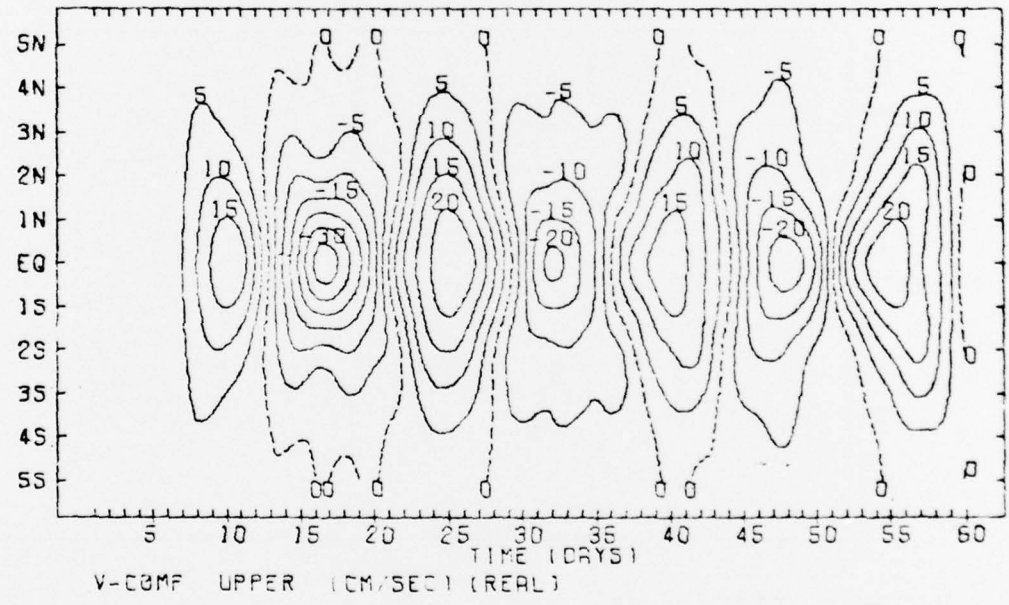




CASE 6: FORCING = PULSE. MEAN FLOW PRESENT

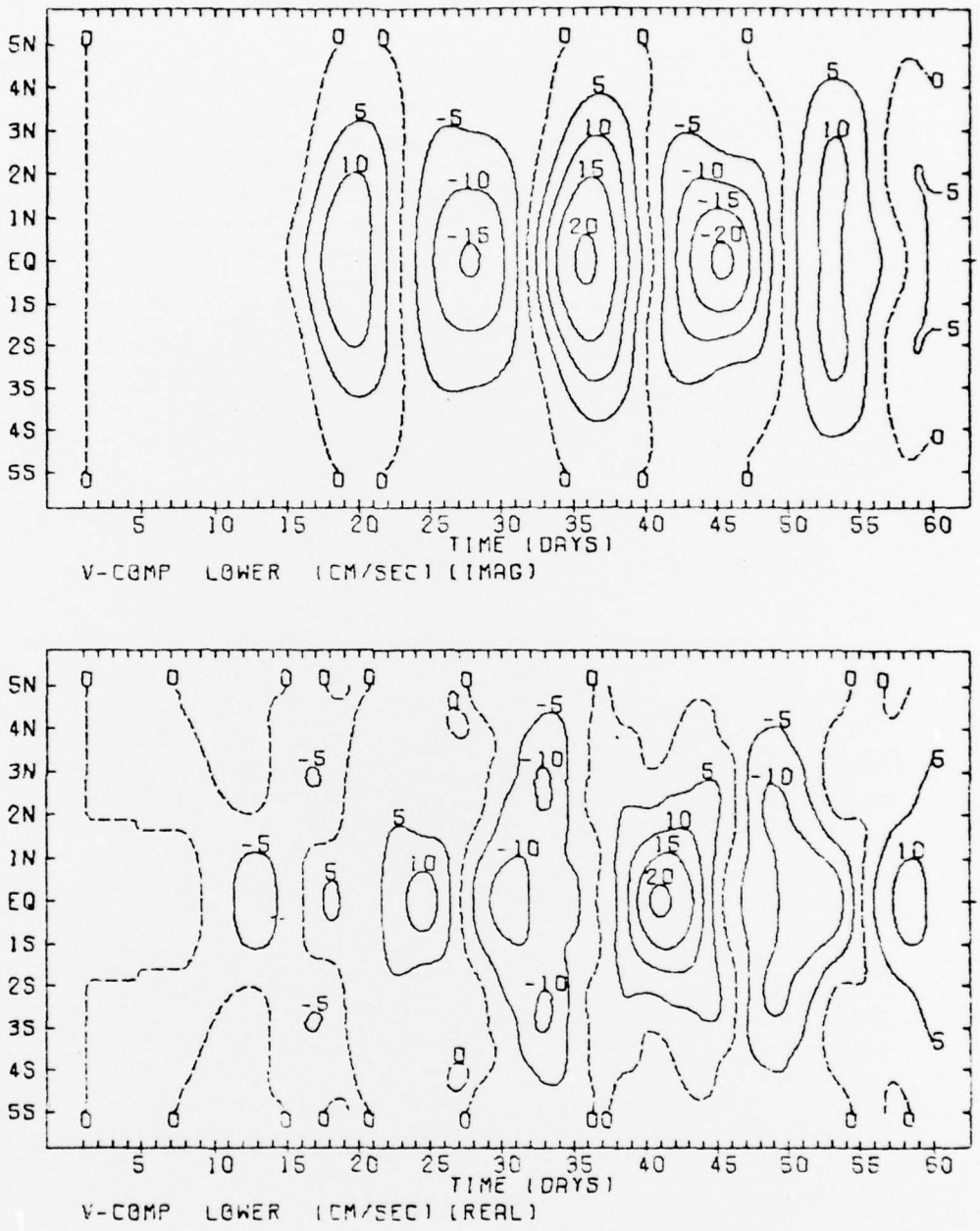
Figure 58





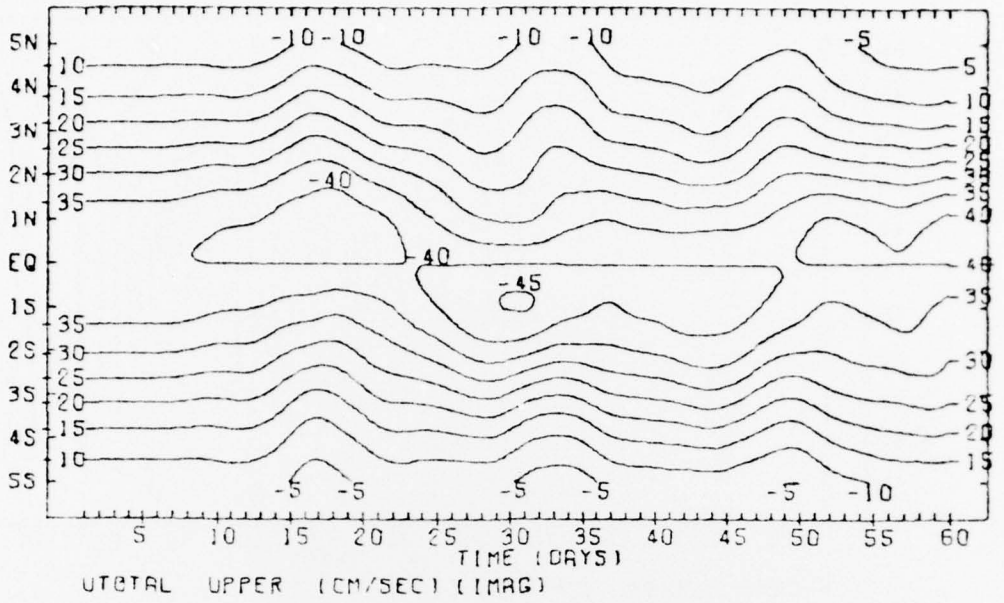
CASE 6 : FORCING = PULSE, MEAN FLOW PRESENT

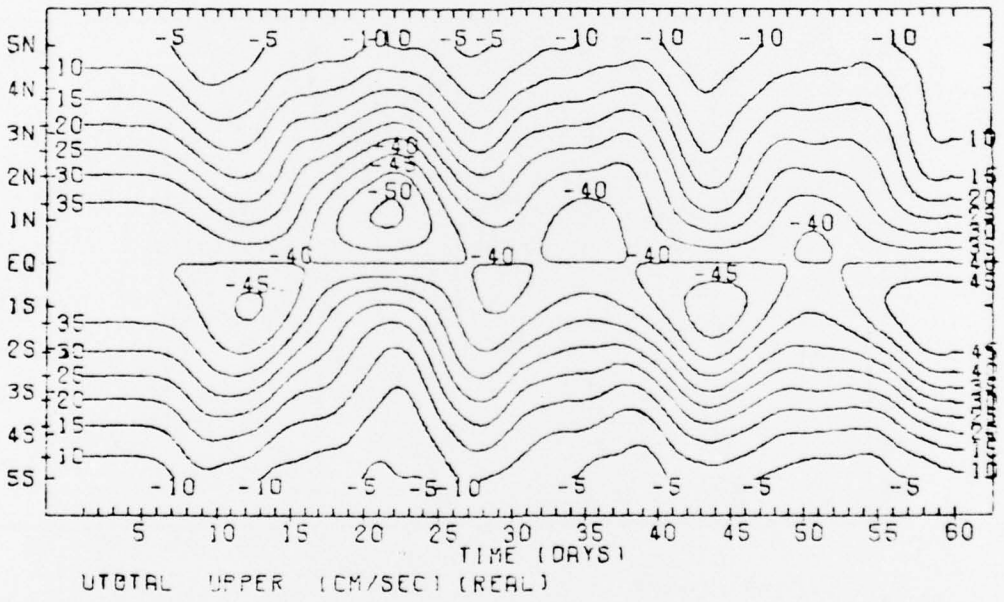
Figure 59



CASE 6: FORCING = PULSE. MEAN FLOW PRESENT

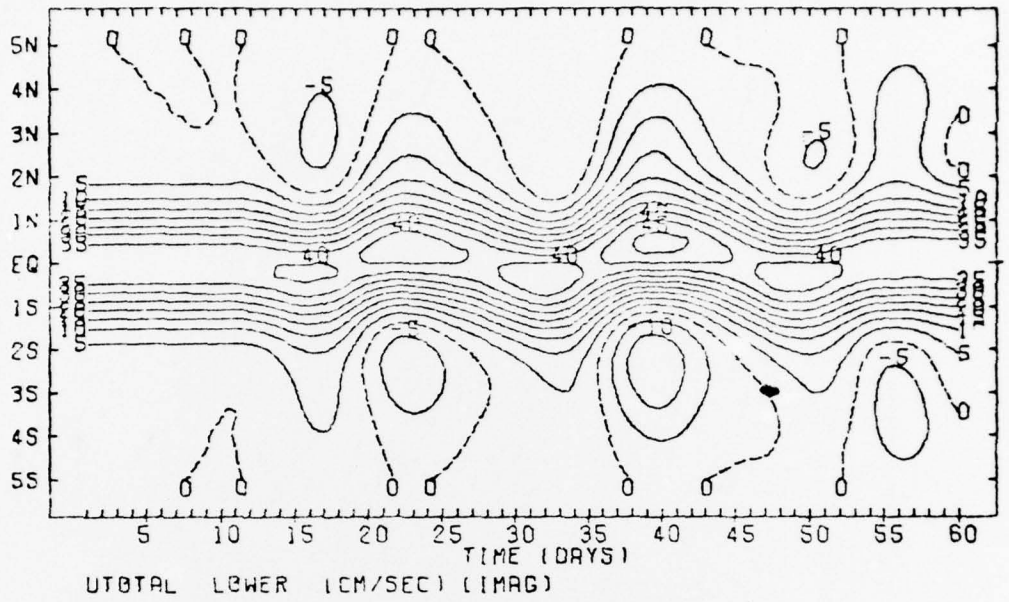
Figure 60

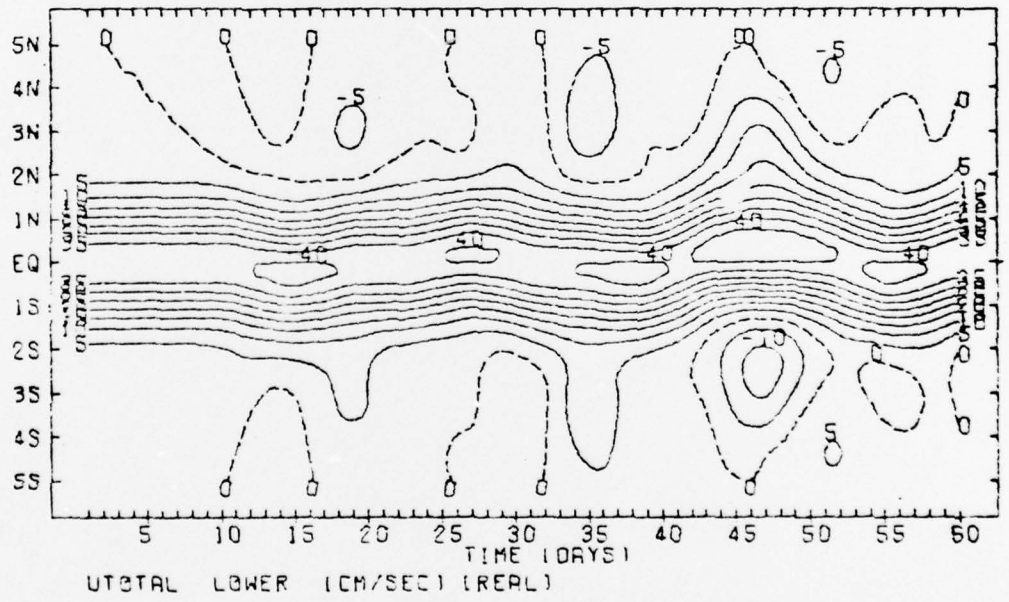




CASE 6: FORCING = PULSE. MEAN FLOW PRESENT

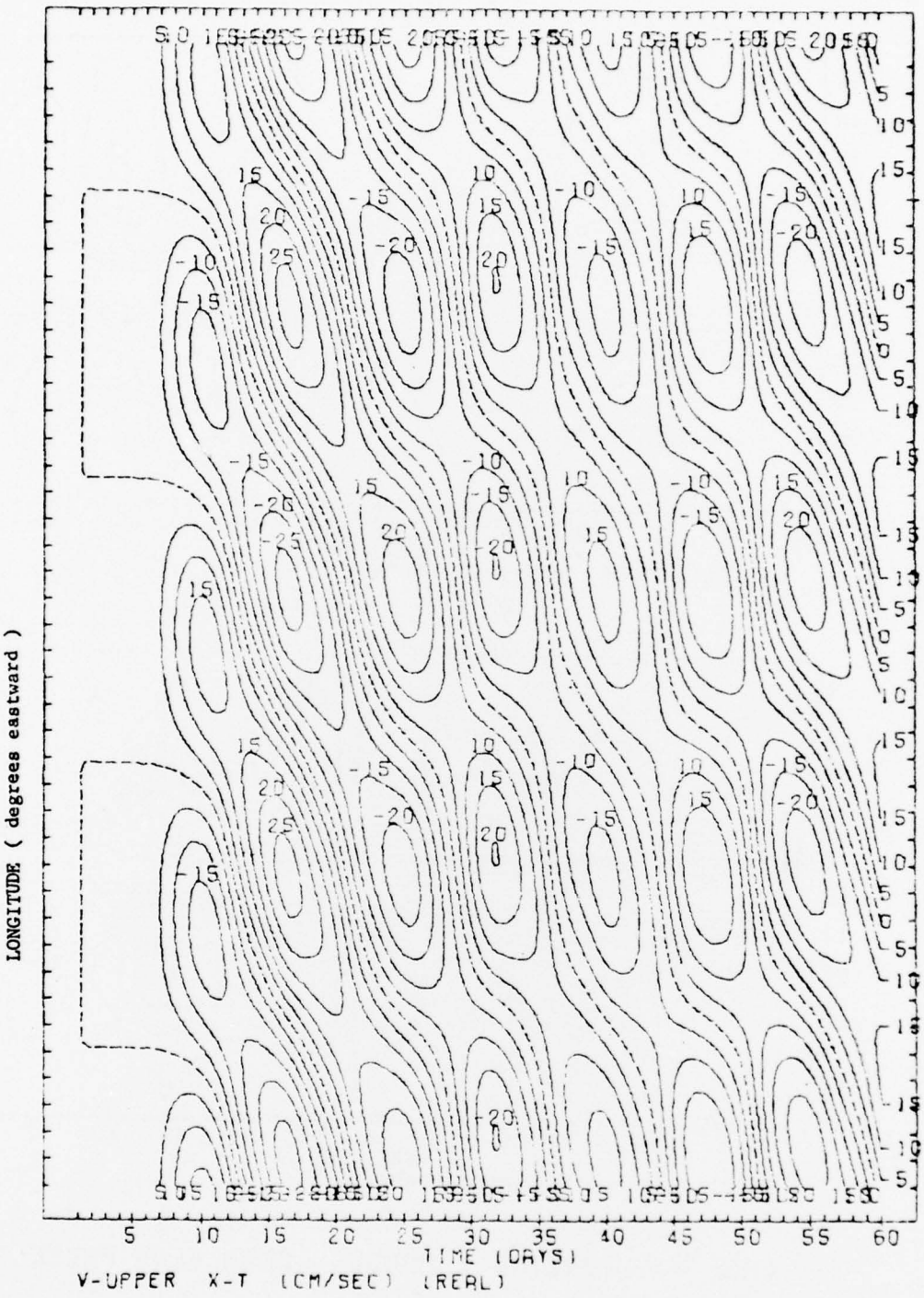
Figure 61





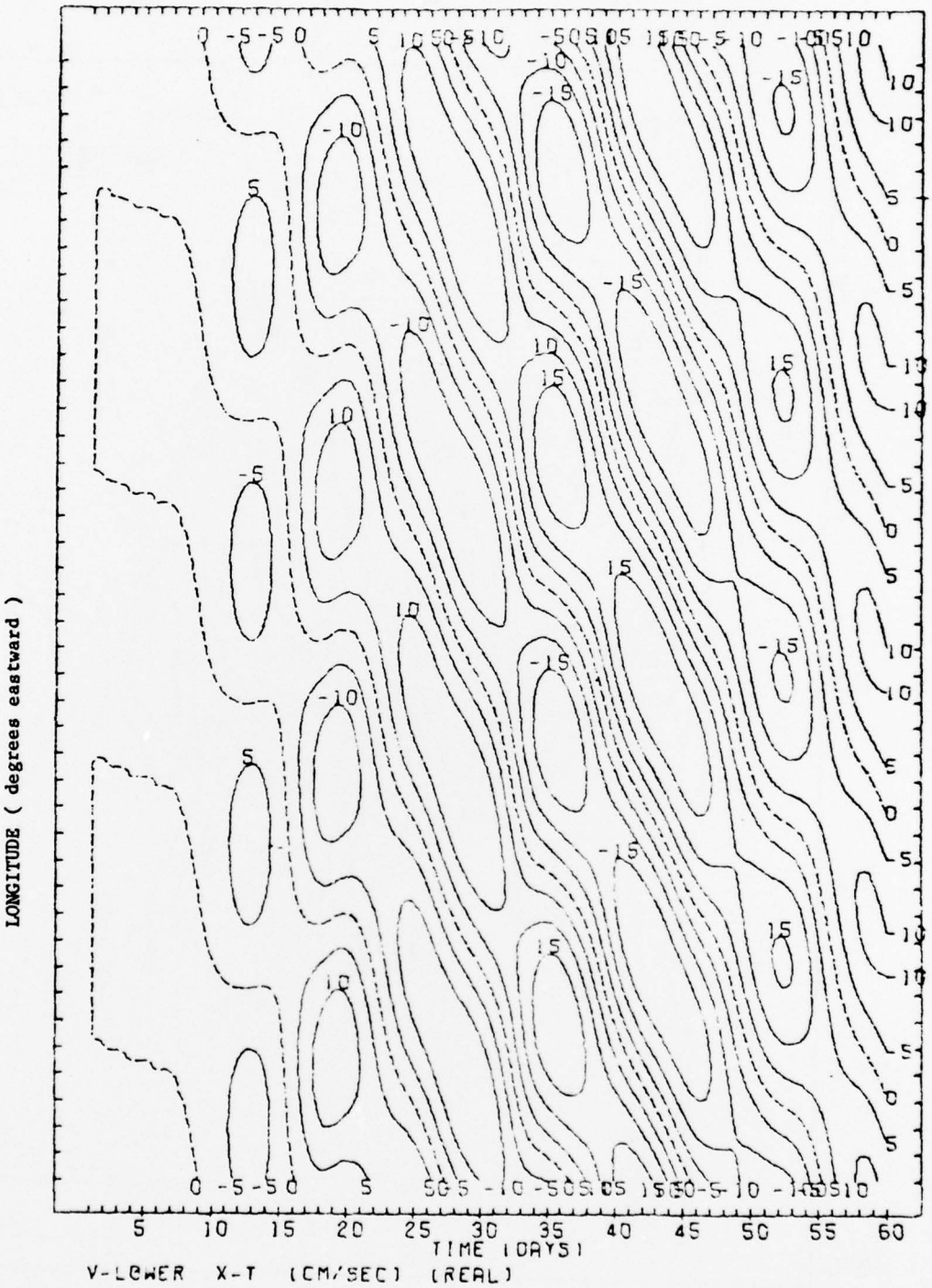
CASE 6: FORCING = PULSE, MEAN FLOW PRESENT

Figure 62



CASE 6: FORCING = PULSE. MEAN FLOW PRESENT

Figure 63



CASE 6: FORCING = PULSE. MEAN FLOW PRESENT

Figure 64

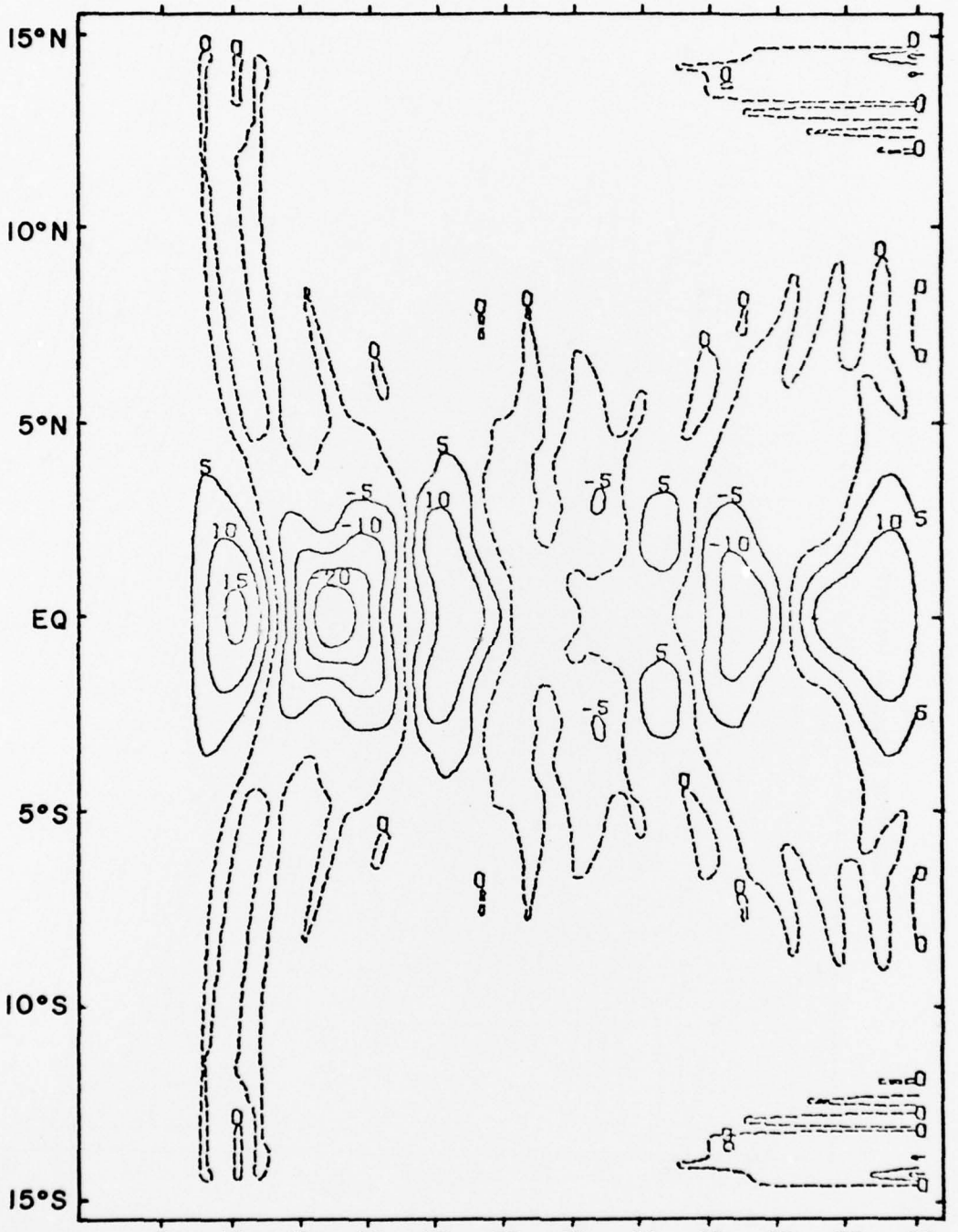

15°N
10°N
5°N
EQ
5°S
10°S
15°S
5
10
15
20
25
30
35
40
45
50
55
60
TIME (days)
V-UPPER (cm/sec) (real) CASE 4: PULSED WIND, NO MEAN FLOW

Figure 65

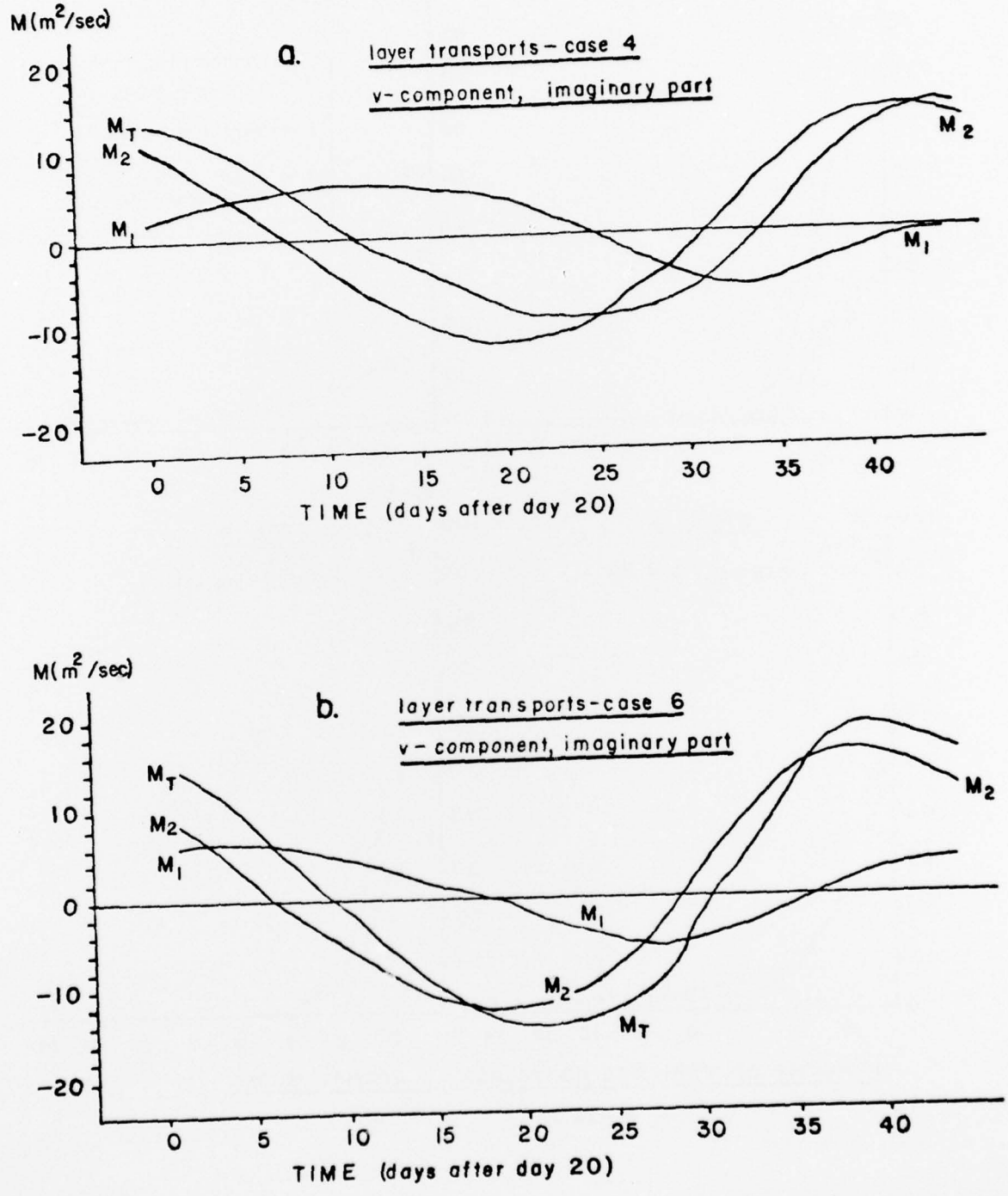

M(m²/sec)
a.
layer transports – case 4
v-component, imaginary part
M_T
M_2
M_1
20
10
0
-10
-20
0
5
10
15
20
25
30
35
40
TIME (days after day 20)
M(m²/sec)
b.
layer transports-case 6
v-component, imaginary part
M_T
M_2
M_1
20
10
0
-10
-20
0
5
10
15
20
25
30
35
40
TIME (days after day 20)

Figure 66

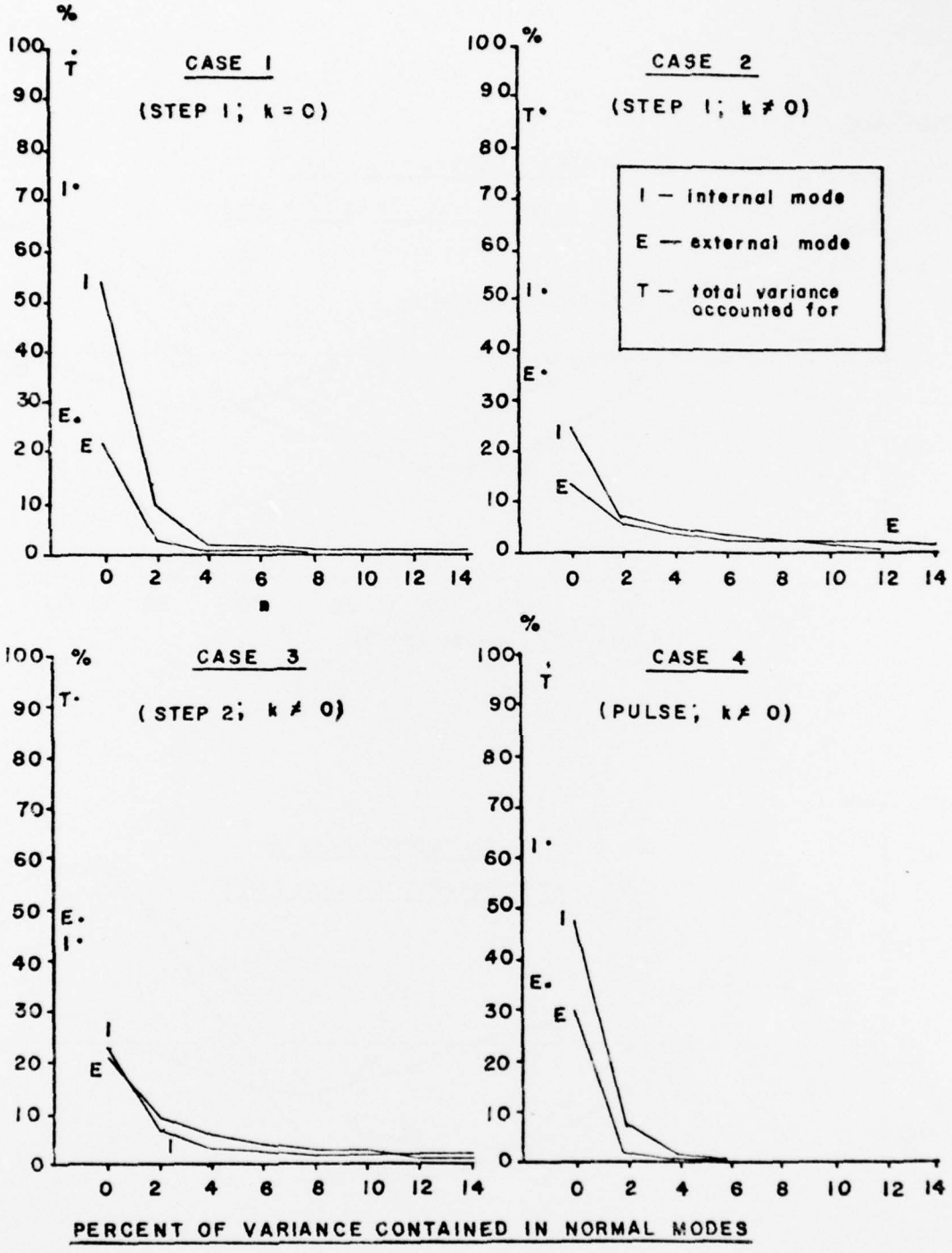

%
CASE 1
(STEP 1; k = 0)
CASE 2
(STEP 1; k ≠ 0)
I — internal mode
E — external mode
T — total variance accounted for
CASE 3
(STEP 2; k ≠ 0)
CASE 4
(PULSE; k ≠ 0)
n
PERCENT OF VARIANCE CONTAINED IN NORMAL MODES

Figure 67